Investigation and analysis of the electro-hydrodynamic (EHD) effects
in asymmetric air gaps

The wire - cylinder case

Konstantinos N. Kiousis BEng, MSc [Hons], MEdu

Submitted for the degree of Doctor of Philosophy

Heriot-Watt University

School of Engineering and Physical Sciences

Institute of Mechanical Process and Energy Engineering

December, 2014

ABSTRACT

In this work, the electro-hydrodynamic (EHD) mechanism, in the case of a thin wire parallel to a conducting cylinder of significantly larger diameter, has been studied. The wire-cylinder geometry may be used in a wide range of applications as a corona discharge generating pair, due to its simple structure and the highly inhomogeneous electric field that can be generated under high voltage DC application, which, in turn, is capable of producing significant EHD flow in air. The physical phenomenon of the EHD effect has been studied through simulations, experiments and comparisons. The operational parameters, such as the electric field and potential distribution, in variously dimensioned electrode arrangements have been investigated, while their dependence on geometrical characteristics of the electrodes, such as the electrode length, the electrode gap and the emitter and collector electrode radii, has been examined. On this purpose, both computer modelling and experimental studies have been conducted.

The electric field and potential distribution has been studied by implementing Finite Element Analysis (FEA). The simulation results have shown that the maximum electric field intensity (E_{max}) was mainly associated with the wire-cylinder radii ratio, while the distance between the electrodes strongly affected the distribution along the axis of the gap. Further analysis of the results has shown that E_{max} may be estimated by an empirical formula which was found to be satisfactory in all cases. An approximate technique for the determination of the unipolar saturation current limit, based on the analysis of the electric field lines has been proposed and the model has been verified through experiments, which have shown that the wire-cylinder unipolar corona discharge current is closely related to the specified theoretical limits.

The experimental study of the EHD flow has shown that the corona discharge current is related to the applied voltage through a quadratic relationship following the well-known Townsend's general model. The ionic wind velocity found to be an approximately linear function of the applied voltage and proportional to the square root of the discharge current, while on the other hand, a linear relationship between the generated thrust and the corona discharge current has been determined. In all cases, the electromechanical efficiency and the thrust efficiency, which is frequently used as an overall performance evaluation factor, have been derived.

DEDICATION

To my family...

With love to my wonderful parents and my beloved wife.

ACKNOWLEDGEMENTS

DECLARATION STATEMENT

(Research Thesis Submission Form should be placed here)

TABLE OF CONTENTS

LIST OF TABLES

LIST OF FIGURES

Figure 4-10 E_{min} variation with the d/R ratio. Wire radius r at 25μm, 250μm and 500μm and potential difference at 1kV in all cases.

Figure 4-11 Representation of the relative error between simulated data and the empirical formula results for E_{max} according to equation (4.1).

Figure 4-12 Field utilization factor f_{wc} with R/r ratio for electrode gap d=3cm.

Figure 4-13 Typical distribution of the electric field lines. FEA results for r =50μm, d=3cm and R=15mm.

Figure 4-14 Schematic representation of the field line parameters for FEA simulations.

Figure 4-15 Electric field line length L_{fl} φ with angle of incidence φ (FEA simulations) for (a) variable electrode gap (d=1-5cm, r=50μm and R=15mm), (b) variable wire radius (r=50-250μm, d=3 cm, and R=15mm) and (c) variable cylinder radius (R=5-15mm, r=50μm and d=3cm). In (b) the fitted curves for different a values coincide.

Figure 4-16 Normalized current density $j_s(\varphi)/j_{s0}$ with the angle of incidence φ for varying electrode gap d, wire radius r and cylinder radius R.

Figure 4-17 Contribution of the saturation current density $j_s(\varphi)$ to the saturation current di_s along a $Rd\varphi$ wide thin strip on the cylinder's surface, per unit length of the electrodes.

Figure 4-18 Normalized distribution of the saturation current $i_s(\varphi)/I_s$ to the angular displacement φ over the cylinder's surface, per unit electrode length.

Figure 5-1. Experimental results of the corona current as a function of the applied voltage for L=300cm, d=3cm, r=50μm and R=15mm. The corona inception threshold (CIV) is also shown at 6.65kV.

Figure 5-21 Electromechanical efficiency with the wind velocity for various wire-cylinder configurations. (a) d_1=2cm, d_2=3cm, d_3=4cm with constant r=50μm and R =15mm, (b) r_1=50μm, r_2=100μm, r_3=250μm with constant d=3cm and R =15mm and (c) R_1 =5mm, R_2 =10mm, R_3 =15mm with constant d=3cm and r=50μm).

Figure 5-22 Representation of the field lines, which define the boundaries of the 'active' flow volume V_{wc} (grey part).

Figure 5-23 Generated thrust per unit length (*N/m*) with (a) applied voltage and (b) discharge current (*A/m*) (d_1=20mm, d_2=30mm and d_3=40mm, r=50μm and R=15mm).

Figure 5-24 Generated thrust per unit length (*N/m*) with (a) applied voltage and (b) discharge current (*A/m*) (r_1=50μm, r_2=100μm and r_3=250μm, d=30mm and R=15mm).

Figure 5-25 Generated thrust per unit length (*N/m*) with (a) applied voltage and (b) discharge current (*A/m*) (R_1=5mm, R_2=10mm and R_3=15mm, d=30mm and r=50μm).

Figure 5-26 Generated thrust (N/m) with power (W/m) for various geometrical characteristics (a) variable electrode gap d, (b) variable emitter radius r and (c) variable collector radius R.

Figure 5-27 Thrust efficiency n_F (N/kW) with generated thrust (N/m) for various geometrical characteristics(a) variable electrode gap d, (b) variable emitter radius r and (c) variable collector radius R.

Figure 5-28 Thrust efficiency n_F (N/kW) with applied voltage (kV) for various geometrical characteristics (a) variable electrode gap d, (b) variable emitter radius r and (c) variable collector radius R.

GLOSSARY

Symbol	Description with Units
r	Emitter (Wire) electrode radius (μm)
d	Electrode separation distance (cm)
R	Collector (Cylinder) electrode radius (mm)
L	Electrode length (mm)
E	Electric Field Intensity (V/m)
V	Applied Voltage (V)
$E_{max\ concyl}$	Maximum Electric Field Intensity in a Concentric Cylinder's Air Gap (V/m)
$E_{max\ consph}$	Maximum Electric Field Intensity in a Concentric Sphere's Air Gap (V/m)
$E_{max\ wire-wire}$	Maximum Electric Field Intensity in a Wire-Wire Air Gap (V/m)
$E_{max\ wire-plane}$	Maximum Electric Field Intensity in a Wire-Plane Air Gap (V/m)
E_{av}	Mean Electric Field Intensity (V/m)
E_{max}	Maximum Electric Field Intensity (V/m)
E_{min}	Minimum Electric Field Intensity (V/m)
f	Field Utilization Factor (E_{max}/E_{av})
a	Ionization Region (μm)
m_u	Wire Roughness factor (m_u=1 for smooth polished wires)
g_0	Air's Dielectric Strength ($\sim 3 \cdot 10^6$ V/m)
δ	Air Density factor (for STP conditions, δ=1)
P	Pressure (cm of mercury)
T	Temperature (°C)
I	Positive Corona Discharge Current (A)
I_L	Positive Corona Discharge Current per unit electrode length (A/m)

V_0	Experimental Measured Corona Inception Voltage (kV)
A	Corona Discharge Current Coefficient (A/V^2)
k	Corona Discharge Current Coefficient (A/V^2)
π	Pi (3.14)
μ	Ion Mobility (in air 1.8 - 2.2·10^{-4} m^2/V·s)
ε_o	Dielectric Permittivity of free space (in air ~8.85·10^{-12} F/m)
ρ	Space Charge Density (C/m^3)
ρ_0	Charge Density at the Ionization Zone (C/m^3)
$\rho(t)$	Space Charge Density versus Time (C/m^3)
t	Drift Time (sec)
t_0	Drift Start Time (sec)
u_D	Ion Drift Velocity (m/s)
Lfl	Field Line Trajectory Length (m)
j_s	Saturation Limit (A/m^2)
ρ_{Lfl}	Saturation Unipolar Ion Density at the Field Line's end (A/m^2)
$j(\theta)$	Saturated Current Density over the Cylindrical Electrode (A/m^2)
j_{s0}	Maximum Current Density (A/m^2)
k_G	Ionic Wind Geometrical Factor (m$^{-1/2}$)
A_{cs}	Discharge Cross Section (m^2)
ρ_{gas}	Gas Density (kg/m^3)
u_{Dmax}	Upper Limit for the Ionic Wind Velocity (m/s)
F	Generated Thrust due to the EHD Effect (N)
n_i	Ion Density
e	Unit charge (the charge of an electron ~1.602·10^{-19} C)
Q	Total Charge (C)
F_{wc}	Generated Thrust in the case of Wire-Cylinder Air Gap (N)

$A_{cs}(d)$	Discharge Cross Section as function of the Distance between the Wire and the Cylinder (m^2)
f_c	Field Coefficient for the Wire-Cylinder Air Gap
V_{wc}	Equivalent Ionic Flow Volume in the Wire-Cylinder Air Gap (cm^3)
V_{hom}	Ionic Flow Volume in a Homogeneous Electric Field (cm^3)
E_{hom}	Mean Field Strength at homogeneous Electric Field (equal to V/d)
E_a	Electric Field Strength at akV (equals a times the strength at 1kV)
A_{BOX}	Fixed distance for the Bounding Box size
D_{BOX}	Total Length of the Electrodes Assembly (air gap included)
k_{BOX}	Scaling Constant
$E(x)/E_{max}$	Normalized Electric Field
$E_{max\,wc}$	Maximum Electric Field Intensity in a Wire-Cylinder Air Gap (V/m)
γ_1	d/r (dimensionless factor)
γ_2	d/R (dimensionless factor)
γ'	$d/2r$ (dimensionless factor)
γ	($\gamma 1=\gamma 2=\gamma$) for $r=R$
f_{wc}	Field Utilization Factor (E_{max}/E_{av}) in a Wire-Cylinder Air Gap
φ	Angle of Incidence on the Cylinder's surface
$\Delta L_{fl\,\varphi,i}$	The Elementary Displacement between Successive Points
L_φ	Total Trajectory Length (the sum of all $\Delta L_{\varphi,i}$ displacements)
$L_{fl\,\varphi}$	Trajectory Length of Field Line with Angle of Incidence φ
a	Dimensionless Parameter coming from $L_{fl\,\varphi}$ data fitting
$i_s(\varphi)$	Saturation Unipolar Current per unit length (A/m)
I_s	Total Unipolar Saturation Current limit (A/m)
k_s	$k_s = 3a = f(r/d, R/d)$ Dimensionless Parameter
j	Current Density (A/m^2)

σ	Conductivity of the Medium ($3\text{-}8 \cdot 10^{-15}$ S/m for air at 20 ˚C)
k_{WC}	Corona Discharge Current Coefficient in the case of Wire-Cylinder Air Gap (A/V^2)
CIV_{SIM}	Air's Dielectric Strength ($\sim 3 \cdot 10^6$ V/m) divided by E_a
E_a	Electric Field Intensity at the vicinity of the Ionization Region a
E_{CIV}	Maximum Electric Field Intensity at the conductor's surface the exact moment when the Corona Discharges Initiate
n	Electromechanical Efficiency (%)
P_{mech}	Mechanical Power (W)
P_{el}	Electrical Power (W)
n_F	Thrust Efficiency (*N/kW*)

ABBREVATIONS

DC	Direct Current
HV	High Voltage
EHD	Electro-hydrodynamic
CIV	Corona Inception Voltage (kV)
BDV	Breakdown Voltage (kV)
FEA	Finite Element Analysis
FDM	Finite Different Method
FEM	Finite Element Method

LIST OF PUBLICATIONS

Chapter in a Book

K.N. Kiousis, A.X. Moronis, W.G. Fruh, *Analysis of the Electric Field Distribution in a Wire-Cylinder Electrode Configuration*, Computational Problems in Engineering, Lecture Notes in Electrical Engineering, Springer: 307, pp. 1-18, 2014.

Publications in Scientific Journals

K.N. Kiousis, A.X. Moronis & W.G. Fruh, *Electro-Hydrodynamic (EHD) Thrust Analysis in Wire-Cylinder Electrode Arrangement*, IOP International Journal of Plasma Science and Technology, 16, 4, pp. 363-369, 2014.

K.N. Kiousis, A.X. Moronis, W.G. Fruh, *Positive Corona Discharge Current in a Thin Wire-Cylinder Electrode Configuration*, ACTA International Journal of Power and Energy Systems, 34, 2, pp. 1-8, 2014.

A.X. Moronis, **K.N. Kiousis**, E.D. Fylladitakis, N. Simou, *A model for determining the unipolar ionic saturation current in parallel wire-cylinder electrodes during corona discharge*, IEEE Transactions on Dielectrics and Electrical Insulation, 21, 3, pp. 1035-1043, 2014.

K.N. Kiousis, A.X. Moronis, E.D. Fylladitakis, *Ionic wind generation during positive corona discharge in a wire-cylinder air gap*, International Journal of Engineering Science and Innovative Technology, 4, 1, pp. 229-239, 2015.

E.D. Fylladitakis, A.X. Moronis, **K.N. Kiousis**, *Experimental evaluation of a needle-to-grid EHD pump prototype for semiconductor cooling applications*, International Journal of Circuits systems and Signal Processing, 8, pp. 337-342, 2014.

E.D. Fylladitakis , A.X. Moronis, **K.N. Kiousis**, *Design of a prototype EHD air pump for electronic chip cooling applications*, IOP International Journal of Plasma Science and Technology, 16,5, pp. 491-501, 2014.

International Conference Proceedings

K.N. Kiousis, A.X. Moronis, W.G. Fruh, *Analysis of the Electric Field Distribution in a Wire-Cylinder Electrode Configuration*, Proceedings of the 1st Europment International Conference on Applied Mathematics and Computational Methods in Engineering, Rhodes, Greece, pp. 164-170, July 17-19, 2013.

K.N. Kiousis, A.X. Moronis, E.D. Fylladitakis, *Finite Element Analysis Method for Detection of the Corona Discharge Inception Voltage in a Wire-Cylinder Arrangement*, Proceedings of the 6th WSEAS International Conference on Recent Advances in Finite Differences and Applied & Computational Mathematics, Vouliagmeni, Greece, pp. 188-193, May 14-16, 2013.

K.N. Kiousis, A.X. Moronis, *Modeling and Analysis of the Electric Field and Potential Distribution in a Wire-Cylinder Air Gap*, Proceedings of the 7th WSEAS International Conference on Recent Researches in Information Science and Applications, Milan, Italy, pp. 35-40, January 9-11, 2013.

K.N. Kiousis, A.X. Moronis, *Experimental Investigation of EHD Flow in Wire to Cylinder Electrode Configuration*, Proceedings of the 10th IASTED European Conference on Power and Energy Systems, Crete, Greece, pp. 21-26, June 22-24, 2011.

E.D. Fylladitakis, A.X. Moronis, **K.N. Kiousis**, *Evaluation of a Single Needle to Grid EHD Pump Prototype for Forced Convection Cooling Applications*, Proceedings of the 1st Europment International Conference on Applied Mathematics and Computational Methods in Engineering, Rhodes, Greece, pp. 282-287, July 17-19, 2013.

K. Kantouna, G.P. Fotis, **K.N. Kiousis**, L. Ekonomou, G. Chatzarakis, *Finite Element Method Analysis of the Electric Field in Cylinder-Wire-Cylinder Electrode Configuration during Corona Discharge*, Proceedings of the 1st International Conference on Circuits, Systems, Communications, Computers and Applications, Iasi, Romania, pp. 204-208, June 13-15, 2012.

CHAPTER 1 - INTRODUCTION

According to literature, it is widely accepted that an electro-hydrodynamic (EHD) effect results when high voltage is applied across a pair of electrodes having substantially different radii of curvature e.g. a sharply pointed electrode and a larger radius electrode [1]. The EHD phenomenon with corona-generated charged particles has been known for a long time [2-4], but only in the modern era considered for practical engineering applications [5, 6]. The first quantitative analysis was made in 1899, where Chattock came to a verifiable relationship through experiments between pressure and current, for a system of plane parallel electrodes [7]. However, the first printed books about the dielectric phenomena and electricity in gases were published a little later and they were the result of extensive work and research. Townsend [8] and Peek [9] provided knowledge for the properties of gaseous, liquid and solid insulations and methods of utilizing these properties to the best advantage in the problems of high voltage engineering. Subsequently, the mechanism of corona wind formation and critical parameters such as corona inception voltage (CIV) and breakdown voltage (BDV) of the air gap were treated extensively.

1.1 THE EHD EFFECT AND ITS APPLICATIONS

The high intensity of the electric field in the vicinity of a high voltage electrode with substantially small radius causes gaseous ionization in the surrounding air. The initiation of corona discharge above a specific threshold voltage (*corona inception voltage*), results in space charge accumulation which, in turn, produces current flow (*corona discharge current*) as the molecules of ionized air drift towards the collector. As shown in figure 1-1, during their motion, charged ions collide with neutral air molecules and atoms which lie along their path, thus transferring their momentum and generating a flow towards the collector, known as "ionic" or "electric" wind [10].

The net result of the EHD effect is the production of flow without any moving parts, characterized by low power consumption, not only in air, but also in other dielectric fluids [11, 12]. At the same time a unidirectional thrust appears in the direction towards the emitter, regardless of the electrode polarity and seems to be proportional to the amount of energy stored in the electric field in the area between the two electrodes [13].
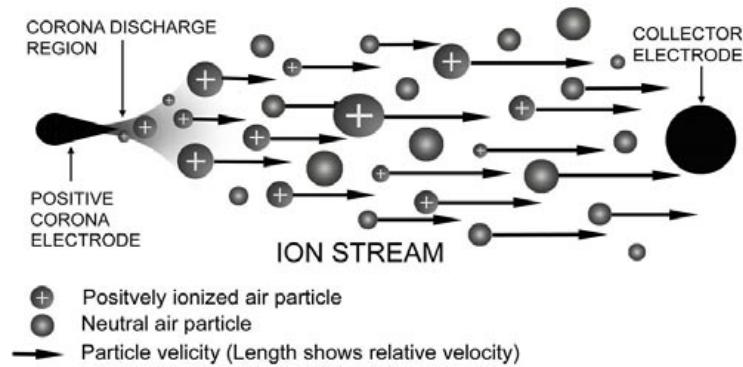
Figure 1-1 Gas molecules surrounding the HV electrode are ionized by the high electric field intensity at the tip, forming an ion stream between the emitter and collector electrodes, thus creating an EHD flow.

Generally, corona discharge is characterized by two regions; a small region very close to the surface of the emitter electrode, the so-called ionization region, and the drift region where the ionized gas molecules are forced towards the collector electrode [14]. The corona mechanism can be simply described as a self-maintained electrical gaseous discharge. The discharge system (see figures 1-2 and 1-3) consists of a high voltage electrode (*emitter*) surrounded by an ionization region where free charge carriers are produced, a low-field drift region where charged particles drift and react (*corona gap*) and a grounded electrode (*collector*), with significantly larger radius compared to the emitter, where charged particles reach and get neutralized. The polarity of the corona is positive or negative depending on the polarity of the voltage applied to the discharge electrode.

The general equation for the charge density and the discharge current is a nonlinear differential equation, which cannot be solved analytically except for certain highly symmetric electrode arrangements [12, 15]. On the other hand, several empirical formulae have been proposed describing the current-voltage characteristics of corona discharges in various electrode configurations e.g. coaxial cylinders, point-ring, rod-plane, point-pot, point-plane and wire-plane arrangements [16-23]. These corona gaps are commonly studied and serve well as benchmarks for corona discharge formulae (see figure 1-4). Positive coronas have been proved to be more stable and more efficient than negative ones, within the narrow range between the corona inception voltage and the breakdown voltage of the gap between the electrodes [24-27].
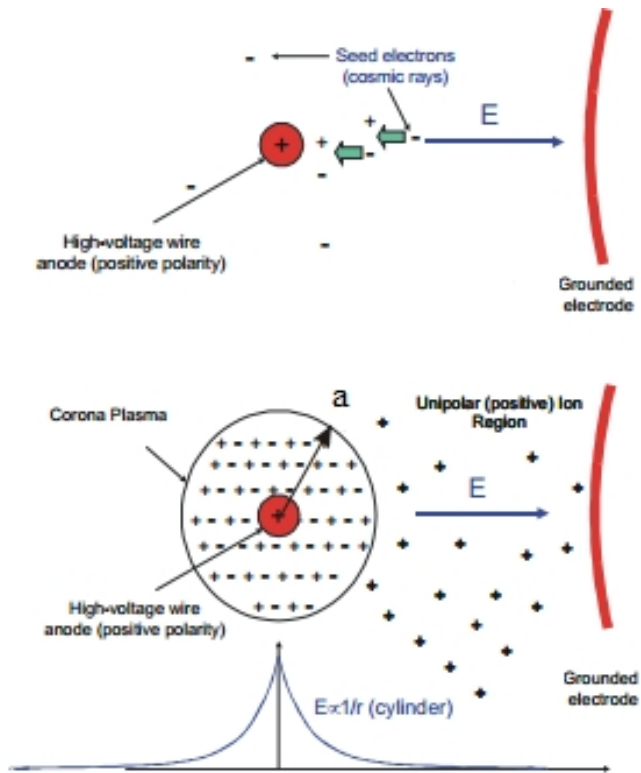
Figure 1-2 Positive DC Corona Discharge in coaxial wire-cylinder electrode geometry (the radius a, indicates the outer boundary of the ionization region).
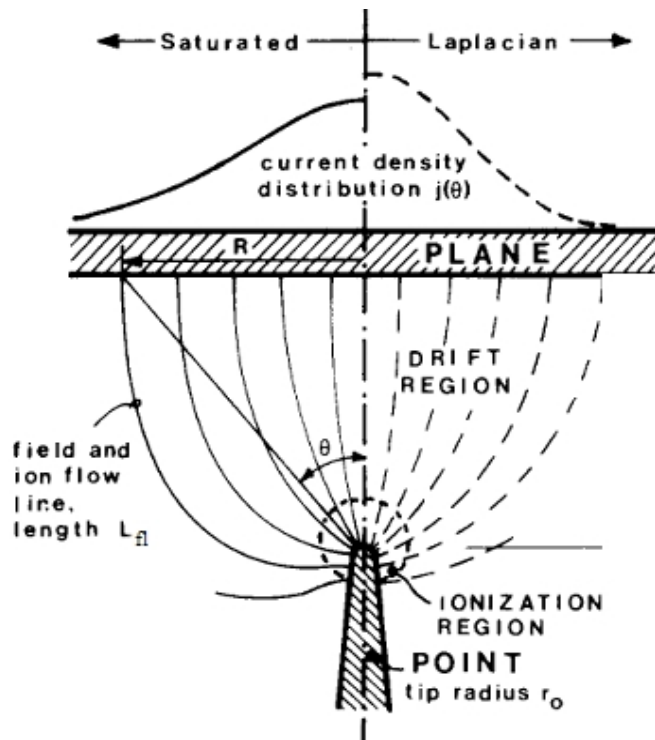
Figure 1-3 Point-to-plane corona gap. Space-charge-saturated field line (left half) and Laplacian (right half) systems sketched in [14].

(a)   (b)
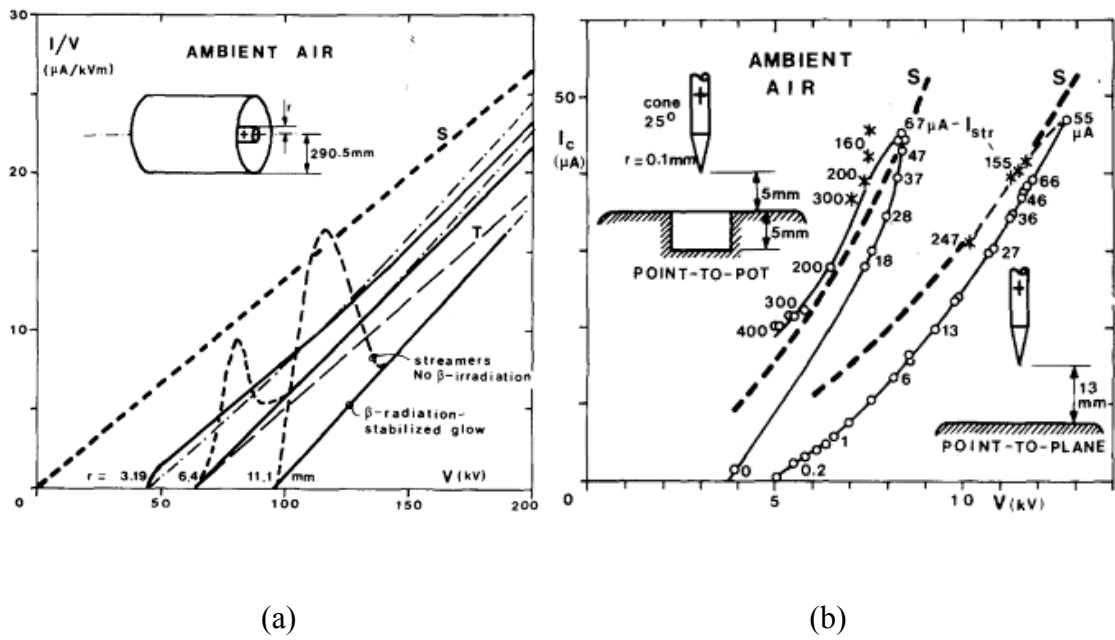
Figure 1-4 (a) Positive corona in ambient air between coaxial cylinders (b) Corona current vs corona voltage, for a point-to-plane and a point-to-pot gap in ambient air, compared with the unipolar saturation current curves.

The EHD phenomenon has not yet been investigated in different configurations and therefore its full potential for practical applications remains undetermined. However, in the 21st century there has been a growing interest over researching the EHD effects for various engineering applications. Nowadays, the EHD effect is widely used in a number of commercial, industrial and research applications such as electrostatic precipitation (see figure 1-5), painting, spraying and coating [28-31] and generally applications where small particle or droplet motion control is needed [32-34]. Unipolar coronas contain ions of one sign only and that is the main reason for their extended use in electrostatic apparatuses.
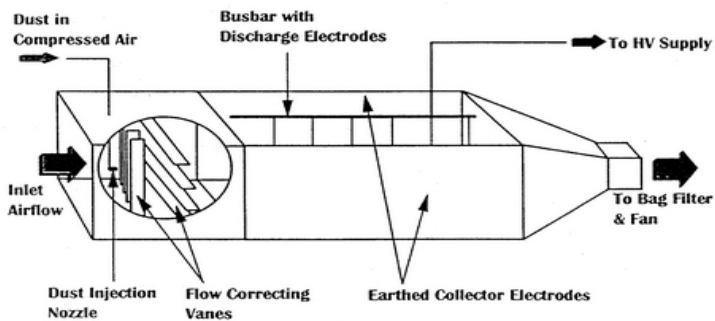
Figure 1-5 Sketch of a laboratory electrostatic precipitator.

Significant research efforts have been made in order to improve the understanding of the impact of corona discharges on air flows [25, 26, 35-40]. Other potential applications, such as dielectric pumping [41-43], enhancement of heat transfer in cooling [44, 45] as well as propulsion applications [46-53] and micro-scale mechanisms [54-56], appeared only recently, driven by increased ecological awareness and market needs (see figures 1-6 and 1-7).
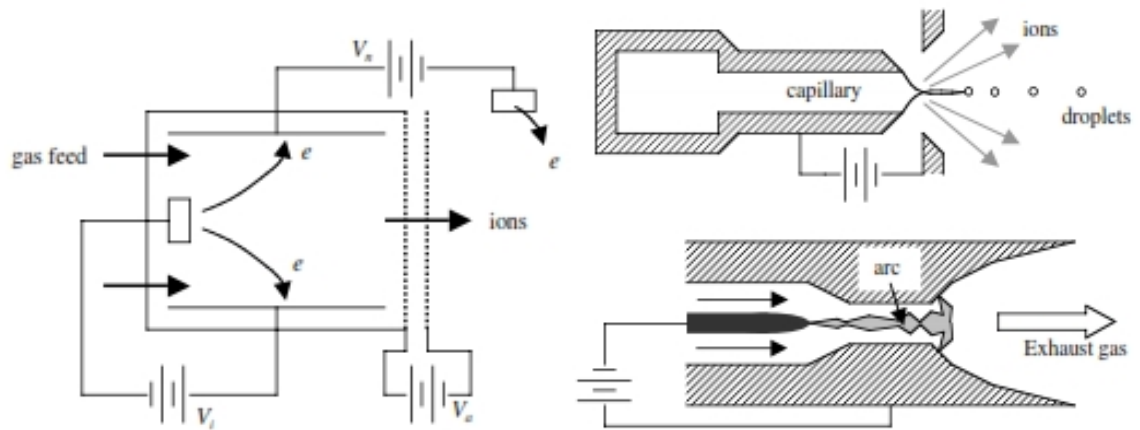
Figure 1-6 Different types of Ion thrusters.
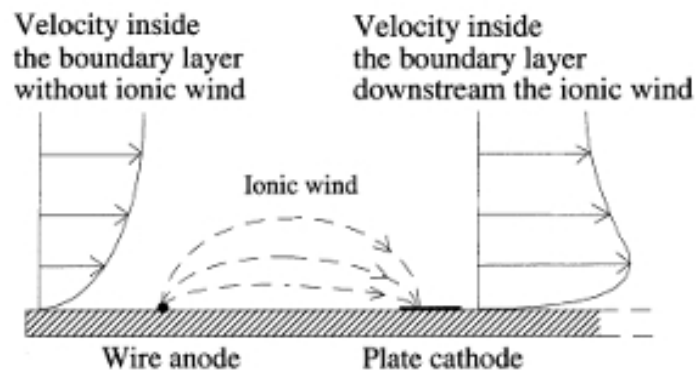
Figure 1-7 Schematic representation of the flow control electro-hydrodynamic actuator.

Velkoff pioneered the EHD cooling, by examining enhanced natural convection using an ionic wind generated by a wire-plate arrangement [57-59], but similar arrangements have been studied also by others [60-62]. The use of a corona discharge as a blower for duct flow between two parallel plates has also been suggested [63, 64].

As displayed in figures 1-8 and 1-9, EHD devices reduced to micro scale dimensions have been proposed for on-chip thermal management of electronic devices [65-72]. Such devices may appear very simple to design and are able to operate silently even for the most difficult geometrical configurations [73-78].

(a)   (b)
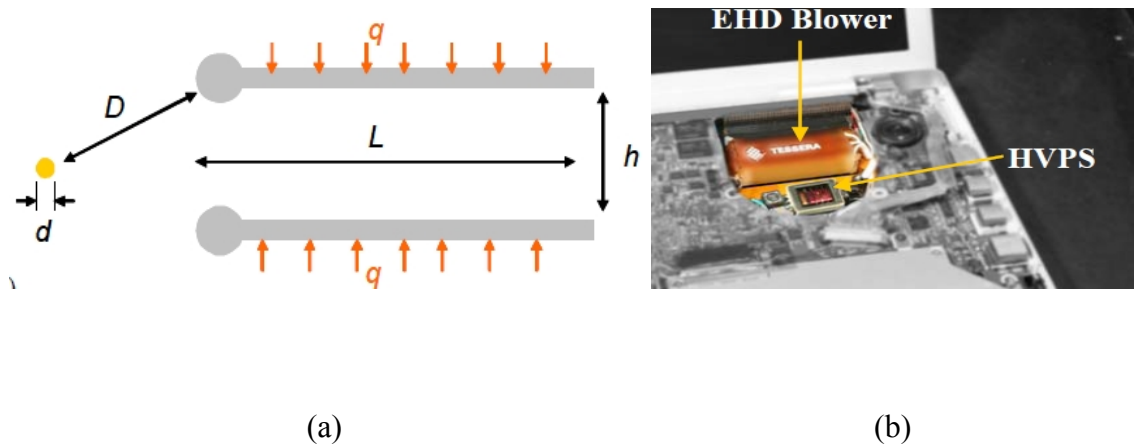
Figure 1-8 EHD cooling device (a) Schematic of the device, with the emitter electrode at the far left and the collectors are two parallel plates (b) prototype with EHD blower and miniature high voltage power supply (HVPS) [65].

(a)   (b)
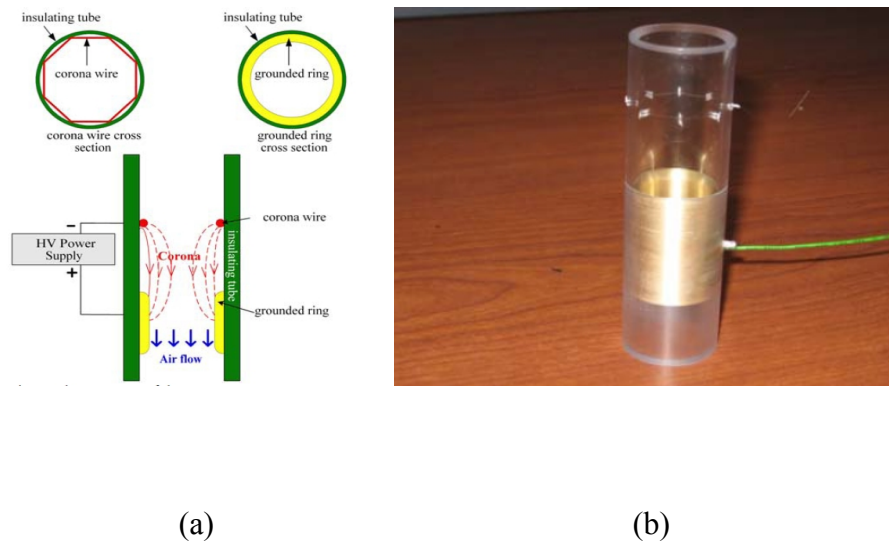
Figure 1-9 Structure of an EHD pump (a) schematic (b) prototype [73].

The EHD effect may also be used in applications such surface treatment [79], pollution control [80], cooling augmentation [81], ozone generation [82] and even agricultural applications [83]. However, all these applications require maximizing the EHD flow velocity [84-87].

On the other hand, certain drawbacks should be pointed out, such as the sensitivity of EHD flow to environmental conditions like humidity, pressure, and temperature, which also affect the breakdown voltage of the dielectric medium [1, 8, 9]. Another drawback is that the EHD flow can be generated in a limited range of the applied high voltage, between the corona inception voltage and the breakdown voltage of the electrode gap [24].

1.2 RESEARCH OBJECTIVES

The aim of this research is to demonstrate and validate the physical aspects of the EHD mechanism through simulations, experiments and comparisons in the case of a wire-cylinder electrode configuration under HV DC application. The operational parameters of the EHD effect, such as the electric field and potential distribution, in variously dimensioned electrode arrangements will be investigated, while their dependence on geometrical characteristics of the electrodes, such as the electrode length, the electrode gap and the emitter and collector radii, will be examined. In addition, the critical physical parameters of the EHD effect will be determined. On this purpose, both computer modelling and experimental studies will be conducted.

There are several applications in which wire-cylinder configurations are being used as EHD flow generation mechanisms [88-91], while they also might find future use in other applications, where other electrode arrangements are being used [25, 39-41]. Due to the simple structure and the highly non-uniform electric field that is produced under high voltage application, the wire-cylinder configuration could be an electrode pair for many other possible applications as well; however, the wire-cylinder air gaps have not been thoroughly investigated. In addition, a large number of computational studies in such non-uniform electric fields may be found in literature [11, 12, 28, 36, 48, 49, 68-71, 80, 89]. However, there is no study available for the wire-cylinder electrode pair.

The parallel wire-cylinder geometry may be used in a wide range of applications as a corona discharge generation pair, due to the highly inhomogeneous electric field that can be produced under HV DC application, which, in turn, is capable of generating significant EHD flow.

The study of the EHD effect and its extensions is still far from mature, and offers many opportunities for both, incremental and possibly even revolutionary developments, in order to study potential applications and derive benefits.

1.3 METHODOLOGY

The electric field and potential distribution in typical wire-cylinder electrode arrangements, under HV DC application, will be studied by implementing the *Finite Element Analysis* (FEA). For this purpose, open source FEA modelling software F.E.M.M. (Finite Element Method Magnetics) ver. 4.2 and dedicated Multiphysics software COMSOL ver. 4.3a will be used. The applied mesh parameters will be optimized in terms of accuracy and processing power in both cases. For accuracy verification purposes, simulation results will be compared with reference results coming from well-known geometries where analytical formulas can be found in bibliography and resemble the wire-cylinder electrode arrangement. Numerical analysis will be carried out on the field intensity along the gap axis, considering different geometrical characteristics of the electrodes, which play the most important role in the spatial distribution of the electric field. A formula for the maximum electric field intensity approximation will be proposed based on a detailed analysis of all simulation results.

The distribution of the electric field lines connecting the wire-cylinder electrodes will also be determined by FEA, in terms of each line's shaping and total length. In fact, these lines could be specified as imaginary particle trajectories. The calculation of each field line length will be performed by tracing the trajectories of particles from the surface of the emitter electrode to the surface of the collector electrode. The acquired data will be treated theoretically in order to calculate the saturation current density as well as the total saturation unipolar corona current limit.

Experiments will be conducted so as to determine the relationship between the electric corona discharge current and the applied high voltage, as well as the current's dependence on geometrical characteristics of the electrodes such as the electrode length, the electrode gap and the emitter and collector radii. Due to the fact that the corona discharge is a rather complex phenomenon, some expressions which have been proposed for the current-voltage characteristics in well-known geometries and serve

well as benchmarks for corona discharge formulae, will be examined. The experimental outcomes will be used in order to define which formula best fits the wire-cylinder arrangement. Further analysis of the results will lead to an expression for the corona current coefficient as a function of the wire-cylinder distance and the wire and cylinder radii. In addition, the Corona Inception Voltage (CIV) in each case will be experimentally determined and the results will be verified with simulation results, as well as with empirical values.

Based on simulation and experimental results, a model will be proposed for the determination of the ionic unipolar corona saturation current in parallel wire-cylinder electrodes in the air, based on the geometrical characteristics of the electric field lines distributing in the space surrounding the electrodes, under HV DC application.

The maximum values of ionic wind velocity will be measured with a hot-wire anemometer in order to determine the relationship between the electric corona discharge current, the ionic wind velocity and the applied high voltage, as well as their dependence on geometrical parameters of the wire-cylinder electrodes. Parametric analysis will be carried out in order to define the dependence of the wind velocity, the function of geometry and the discharge cross section, on geometrical characteristics of the electrodes. In all cases, an upper limit for the wind velocity will be defined assuming single carrier conduction. Based on the experimental findings, an expression for the discharge cross section will be derived for the case of a wire-cylinder electrode configuration. The electromechanical efficiency of the wire-cylinder electrode setup will be determined and will be compared with other results found in bibliography for different electrode geometries.

Measurements of the generated thrust due to the EHD effect will be made with a precision balance in order to determine the relationship between the generated thrust and the corona discharge current. A 'field coefficient' will be introduced as a measure of the electric field inhomogeneity. In this case also, the maximum electromechanical efficiency and the thrust efficiency, which is frequently used as an overall performance evaluation factor, will be evaluated and discussed accordingly.

1.4 OUTLINE OF THE THESIS

The thesis is composed of an Introduction, four Chapters, Conclusions and a list of References. It consists of 142 pages, 17 tables and 73 figures, while the list of references includes 136 entities.

In Chapter 2, the theoretical aspects of the EHD effect have been presented. The EHD flow parameters such as the electric field, the positive corona discharge current, the corresponding ionic wind and the generated thrust due to the reaction force have been presented.

In Chapter 3, the experiment is introduced. The electrode geometry, the FEA model along with the governing equations, the modelling parameters and the verification of the mesh formation are presented. Moreover the experimental setup is described analytically.

Chapter 4 includes the FEA simulation results and discussion, as well as the proposed formula for E_{max} in the case of wire-cylinder arrangement. In addition, the FEA field line lengths, the saturation current density limit and the unipolar saturation current limit have been derived.

In Chapter 5, the experimental results are presented and discussed based on the EHD flow parameters such as the corona discharge current, the ionic wind velocity and the generated thrust and their dependence on geometrical parameters of the wire-cylinder electrodes.

In Chapter 6, the conclusions of the study are presented and discussed.

The main results of the thesis have been published in form of papers in scientific journals, international conference proceedings and in one chapter of a book. Six (6) papers have been published in journals such as the IOP Journal of Plasma Science and Technology, the IEEE Transactions on Dielectrics and Electrical Insulation, the ACTA International Journal of Power and Energy Systems and the International Journal of

Circuits Systems and Signal Processing. Six (6) papers have been presented in International Conferences such as the 1st Europment International Conference on Applied Mathematics and Computational Methods in Engineering in Rhodes, Greece, the 6th WSEAS International Conference on Recent Advances in Finite Differences and Applied & Computational Mathematics in Vouliagmeni, Greece, the 7th WSEAS International Conference on Recent Researches in Information Science and Applications in Milan, Italy, the 10th IASTED European Conference on Power and Energy Systems in Crete, Greece and the 1st International Conference on Circuits, Systems, Communications, Computers and Applications in Iasi, Romania. One (1) paper has been published as a chapter in the Springer volume Computational Problems in Engineering, Lecture Notes in Electrical Engineering. Finally, a publication offer for the thesis in the form of a book came from LAP (Lambert Academic Publishing) International Publishing House, which showed interest after examining several published papers.

CHAPTER 2 - THEORETICAL ASPECTS

2.1 ELECTRIC FIELD

In response to an increasing demand for electrical energy, operating transmission level voltages have increased considerably over the last decades. Designers are therefore forced to reduce the size and weight of electrical equipment in order to remain competitive. This, in turn, is possible only through a thorough understanding of the properties of insulating materials and knowledge of electric fields and methods of controlling the electric stress [92].

The electric field describes the electric force experienced by a motionless positively charged particle at any point in space relative to the source of the field. The concept of an electric field was introduced by Faraday [3].

The electric field strength is the key parameter that defines the behaviour of insulating materials under high electric field stress. The electric stress to which an insulating structure is subjected is numerically equal to the negative voltage gradient:

$$E = -\nabla V \tag{2.1}$$

where E is the electric field intensity (V/m) and V (V) is the applied voltage. The negative sign arises as positive charges repel, so a positive charge will experience a force away from the positively charged conductor, in the opposite direction to that in which the voltage increases.

On the other hand, the electric strength of an insulating material can be defined as the maximum dielectric stress which the material can withstand. The electric breakdown strength of insulating materials depends on a variety of parameters e.g. pressure, temperature, humidity, electrode material and geometry, as well as surface impurities and imperfections (see figure 2-1).

(a)   (b)
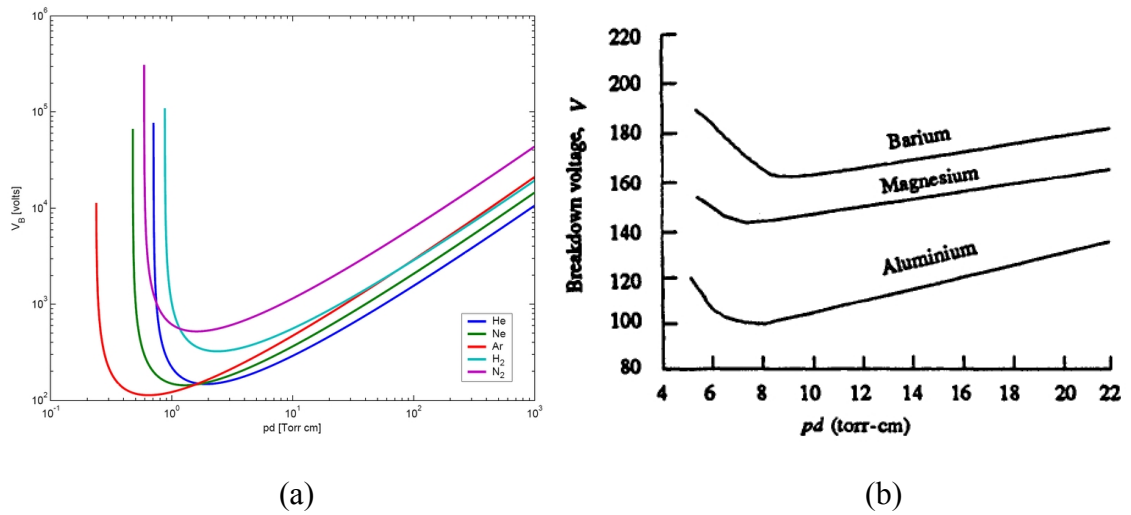
Figure 2-1 (a) Paschen's breakdown voltage-*pd* (*p* is the pressure and *d* is the electrode gap) characteristics [93] and (b) dependence of the breakdown voltage on the cathode materials.

Electric field distribution

The study of the electric field distribution is of great importance for the design and dimensioning of high voltage equipment [94-97]. In a uniform field, as shown in figure 2-2, the electric field is constant at every point and can be approximated by placing two conducting plates parallel to each other and maintaining the potential difference between them.
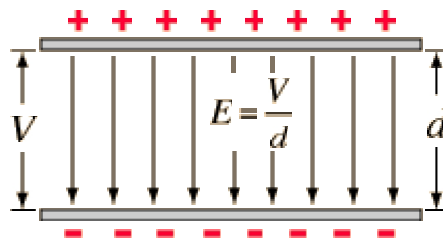
Figure 2-2 A uniform electric field between charged parallel plate conductors.

Non uniform electric fields (see figure 2-3) stress the insulants unevenly; hence the electric strength is reduced. A non-uniform field configuration may apply excessive stress at certain locations (e.g. at the conductor's surface).
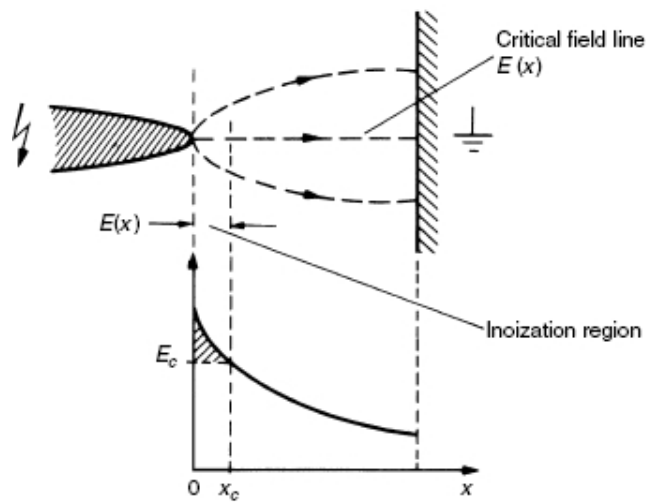
Figure 2-3 Electric field distribution in a non-uniform field gap [92].

There are many methods for determining the potential distribution in order to define the stress and strength of insulating materials [95]. Field sketching (as shown in figure 2-4) is a valuable, rather outdated and emphasized on FEA methods technique for estimating the electric field distribution in one plane of an electrode assembly. In many practical cases it is possible by using some simple rules to plot the field lines and the equipotentials. The resistive film and conducting paper technique, as well as the electrolytic tank method, rely on the fact that the conduction of the current between conductors in liquids can be used as an analogue in the electric field distribution in HV dielectrics.
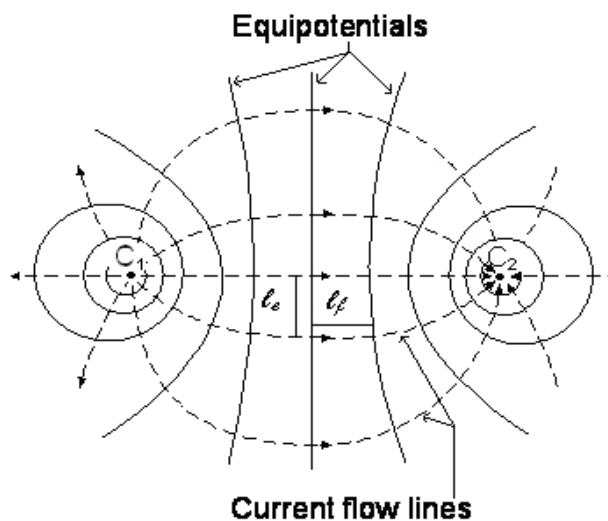
Figure 2-4 Field sketching technique [92].

Approximations from known geometries, is a method using practical electrode configurations from geometries for which analytical solutions exist (e.g. concentric cylinders and spheres, parallel wires and wire-plane air gaps) [97].

The maximum field intensity, in the case of concentric cylinders and spheres may be given as [92]:

$$E_{max\,concyl} = \frac{V}{r_1 \cdot \ln\left(\frac{r_1}{r_2}\right)}$$

(2.2)

$$E_{max\,consph} = \frac{V}{R_1\left(1 - \frac{R_1}{R_2}\right)}$$

(2.3)

where r_1, r_2 are the inner and outer cylinder radii and R_1, R_2 the inner and outer sphere radii respectively.

The analytical formula for the maximum field intensity, in the case of identical parallel wires arrangement is [92]:

$$E_{max\,ww} = \frac{V}{d} \cdot \frac{\sqrt{\left(\frac{d}{2r}\right)^2 + \left(\frac{d}{r}\right)}}{\ln\left(1 + \left(\frac{d}{2r}\right) + \sqrt{\left(\frac{d}{2r}\right)^2 + \left(\frac{d}{r}\right)}\right)}$$

(2.4)

On the other hand, the maximum field intensity, in the case of wire-plane geometry, is [92]:

$$E_{max\,wp} = \frac{V}{r \cdot (d-r)} \cdot \frac{\sqrt{d^2 + r^2}}{\ln\left(\frac{d + \sqrt{d^2 + r^2}}{r}\right)}$$

(2.5)

where r is the wire radius and d the electrode gap.

In most practical cases, two field quantities may be defined. These are the maximum field strength E_{max} and the mean value of the field strength E_{av}. With these two quantities a 'field efficiency factor' (*field utilization factor*) *f* can be derived. In this way it is possible to estimate the breakdown voltage of a wide variety of electrode and insulation system geometries by using known breakdown data (see figure 2-5) [92].

$$E_{av} = \frac{V}{d} \tag{2.6}$$

$$f = \frac{E_{max}}{E_{av}} = \frac{d \cdot E_{max}}{V} \tag{2.7}$$
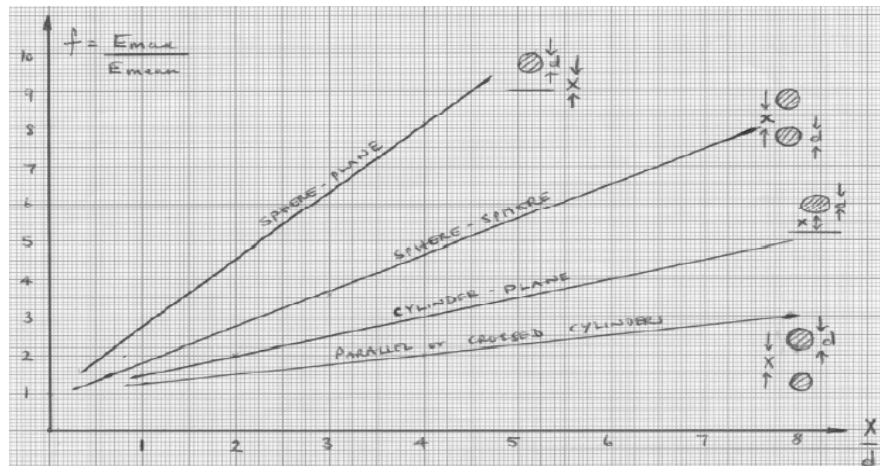
Figure 2-5 Field utilization factor for various air gaps.

The experimental measurement of the field strength in air gaps is in fact difficult and not quite accurate, due to the presence of sensing elements which may affect the distribution of the electric field. On the other hand, computer methods can provide instant and accurate results and are capable of solving problems in more complex conditions. Some of the most commonly used software applications implement the Finite Difference Method (FDM) and the Finite Element Method (FEM) as shown in figure 2-6 [97, 98].
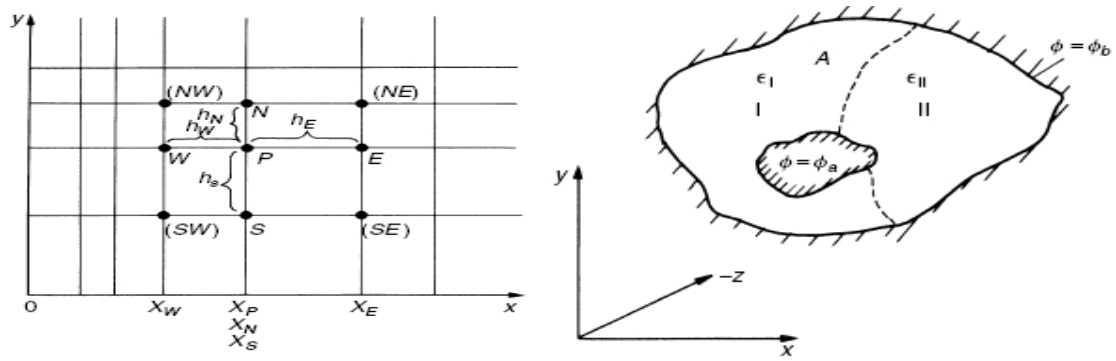
Figure 2-6 Finite Difference Method (FDM) and Finite Element Method (FEM).

Despite the large number of computational studies of the electric field distribution in uniform and non-uniform electric fields at different electrode configurations found in literature [11, 12, 28, 36, 48, 49, 68-71, 80, 89, 97-105], there is no study available for the wire-cylinder electrode arrangement.

2.2 CORONA DISCHARGE

At normal temperature and pressure, gases are excellent insulators. The insulating character of air for example is taken for granted in HV applications [92]. In the absence of electric field, the rate of electron and positive ion generation in an ordinary gas is counterbalanced by decay processes and a state of equilibrium exists. This state of equilibrium will be upset upon the application of a sufficiently high electric field.

In a uniform electric field, a gradual increase in voltage across a gap produces a breakdown of the gap in the form of a spark without any preliminary discharges. On the other hand, if the field is non-uniform, an increase in voltage will first cause a localised discharge in the gas to appear at points with the highest electric field intensity, namely at sharp points or where the electrodes are curved on transmission line conductors. The variation of the current measurements between two parallel plate electrodes was first studied as a function of the applied voltage by Townsend [8]. Townsend found that the current at first increased proportionally with the applied voltage and then remained nearly constant at a value which corresponded to the saturation current. Further increase of the applied voltage led to an exponential increase of current. The general pattern of the current-voltage relationship is shown in figure 2-7.
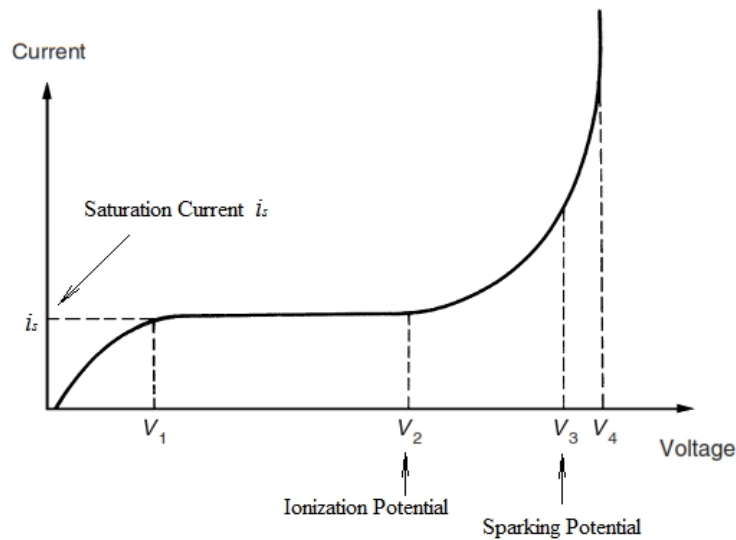
Figure 2-7 Current-voltage characteristic in pre-spark region.

The breakdown corresponds to the establishment of a conductive channel between the electrodes. At low pressures, breakdown occurs with a silent spark. At high pressures, the spark is bright and noisy. The type of discharge that follows spark breakdown depends on the gas pressure, the gap length and geometrical form of the electrodes, the nature of the applied voltage and the constants of the external circuit. The Townsend sparking criterion defines the onset of a process when each primary electron produces one secondary electron which can carry the process. The production of electrons becomes independent and there is self-sustained discharge that is termed corona. This form of discharge can be observed as a bluish luminance, it is always accompanied by a hissing noise, and the air surrounding the corona region is converted to ozone [8, 9].

Corona discharges result in considerable power losses from HV transmission lines, radio interferences and corrosion of adjacent solid insulating materials, long before complete breakdown occurs. These discharges often lead to deterioration or complete breakdown of the insulation [1]. On the other hand the sustainable corona discharge process is widely used as the source of unipolar ions in a number of laboratory and industrial applications as mentioned in Chapter 1-1.

In order for corona discharges to initiate, the surrounding air near sharp high voltage electrodes needs to be ionized. In this way an 'ionization region' is defined and

extends from the outer surface of the high voltage electrode up to a short distance a, depending on its radius of curvature. The ionization region for two identical parallel cylindrical conductors can be calculated as:

$$a = 0.301 \cdot \sqrt{r} \tag{2.8}$$

where r (cm) is the radius of the conductors [9].

Once the field intensity (*potential gradient*) around the emitting electrode is high enough and free electrons are massively produced in the overstressed 'ionization region', which becomes in fact fully conductive, then corona discharges initiate. The threshold voltage for the corona discharges (*Corona Inception Voltage*) between two parallel conductors has been investigated by Peek who thereby developed some well-known empirical formulae [9]:

$$CIV = m_u \cdot g_0 \cdot \left(1 + \frac{0.301}{\sqrt{\delta \cdot r}}\right) \cdot r \cdot \ln\left(\frac{d}{r}\right) \tag{2.9}$$

where m_u represents the wire roughness factor (m_u=1 for smooth polished wires), g_0 is the air's dielectric strength ($\sim 3 \cdot 10^6$ V/m), d (m) is the electrode gap and δ is the air density factor:

$$\delta = 3.92 \cdot \frac{P}{273 + T} \tag{2.10}$$

where P and T are the pressure in cm of mercury and temperature in °C respectively.

Successful attempts have been made since then, to relate the inception of the corona discharges with geometry and environmental parameters [107-110], but the parallel wire-cylinder arrangement has not been studied.

After the corona initiation, space charge accumulates in the vicinity of the high voltage electrode, which in turn produces current flow (*corona discharge current*) as ionized air molecules drift towards the collector (*grounded electrode*) due to the forces

of the electric field. The drift region across the gap may be regarded as a passive resistance in series with the ionization region which has very low resistance. This is the main reason for the exceptional stability of positive coronas [14]. Unipolar coronas contain ions of one sign only, which is the main reason for their extended use in electrostatic apparatus (precipitators, separators etc.). Although the corona discharge is a rather complex phenomenon, various formulas for the corona current intensity I have been proposed in bibliography [1, 8, 9, 15-21, 32-34, 111-115]. The most known expressions are given below:

$$I = A \cdot V \cdot (V - V_0) \tag{2.11}$$

$$I = k \cdot (V - V_0)^2 \tag{2.12}$$

where I (A) is the corona discharge current, V (V) is the applied voltage, V_0 (V) is the corona inception voltage (*CIV*) in each case and k, A (A/V^2) are coefficients related to ion mobility, dielectric permittivity and geometrical characteristics of the electrodes. Equations (2.11) and (2.12) are also known as Townsend's formulae [8].

A short discussion on coefficients A and k follows:

Coefficient A

For coaxial cylindrical geometry, coefficient A was approximated by Cooperman [111]:

$$A = \frac{8 \cdot \pi \cdot \mu \cdot \varepsilon_0}{R^2 \cdot \ln\left(\frac{R}{r}\right)} \tag{2.13}$$

where μ is the ion mobility (1.8 - 2.2·10^{-4} m^2/V·s in air) [112, 113], ε_0 is the dielectric permittivity of the medium (8.85·10^{-12} F/m for air) and r, R (m) are the radii of the inner and outer cylinder, respectively.

Cooperman also derived an expression for coefficient A in the case of a wire placed halfway between two parallel plates:

$$A = \frac{4 \cdot \pi \cdot \mu \cdot \varepsilon_0}{d^2 \cdot \ln\left(\frac{4 \cdot d}{\pi \cdot r}\right)} \tag{2.14}$$

where d (m) is the distance from the wire to the plate and r (m) is the wire radius.

Coefficient k

As far as coefficient k is concerned, some approximations introduce an expression for a rod-plane geometry [114]:

$$k = \frac{\mu \cdot \varepsilon_0 \cdot \ln\left(\frac{R}{r}\right)}{R^2 \cdot 8 \cdot \pi} \tag{2.15}$$

as well as a formula in the case of coaxial cylinders arrangement [115]:

$$k = \frac{2 \cdot \mu}{R^2 \cdot \ln\left(\frac{R}{r}\right)} \tag{2.16}$$

2.3 UNIPOLAR SATURATION CURRENT

The unipolar saturation current is of great importance, whereas exceeding this limit results in bipolar conduction phenomena like streamers, which may lead to undesirable instabilities or even breakdown and are considered the worst EMI (Electromagnetic Interference) offender [14]. The determination of the ionic unipolar saturation current can be made by estimating the contribution of all electric field lines emerging from the emitting electrode and reaching the collector. The main complication in these cases is the treatment of the generated space charges which affect the electric field distribution. On the other hand, all different charged species which affect the total space charge distribution should be considered. Subsequently, the general equations for the space charge density and the electric discharge current are in fact nonlinear integro-differential expressions, which are very difficult to be solved even for relatively simple geometries [91].

According to Sigmond [14, 116], an approximation can be made to simplify this complex problem; unipolar ions drifting without diffusion with constant mobility can be considered. This is realistic in the case of electrical coronas where ionization is only confined in a small volume around the emitting electrode where the electric field is high, while, on the other hand, ions move towards the collecting electrode crossing the drift region, where the electric field is comparatively low [116]. In fact ions coming from the ionization region are "injected" into the drift region which is characterized by Ohmic behaviour, regarding the current flow. Therefore, assuming unipolar ions of positive polarity (*positive coronas*) with constant mobility μ, drifting with space charge density $\rho(t)$ versus time, we can get to the unipolar charge drift formula which is valid along any field line connecting the electrodes [14]:

$$\frac{1}{\rho(t)} - \frac{1}{\rho_0} = \frac{\mu}{\varepsilon_0}(t - t_0) \qquad\qquad (2.17)$$

where $\rho_0 = \rho(t_0)$ is the charge density at the ionization zone.

Considering a single ion flow tube (see figure 2-8) corresponding to such a line of length L_{fl}, the saturation unipolar ion density $\rho_{Lfl} = \rho(t_0 + t)$ is obtained at the line's end, at its point of incidence on the collector's surface after the drift time t required for the ions to cross the gap between the electrodes.
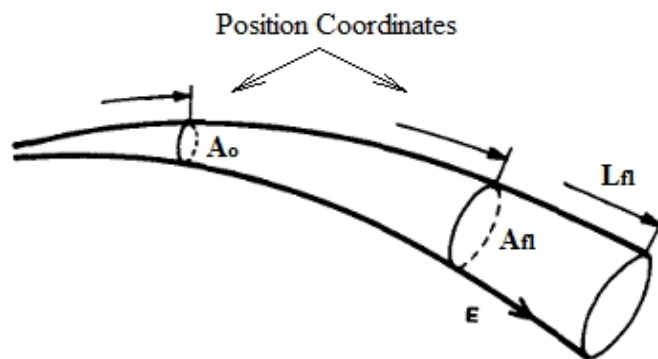
Figure 2-8 An ion flow tube, with area A_0 to A_{fl} at a position coordinate [14].

For a given voltage drop V along the line, these ions travel along it, moving under the field force, with average velocity [32, 33]:

$$u_D = \mu \cdot E_{av} = \mu \cdot \frac{V}{L_{fl}} \tag{2.18}$$

Since ρ_0 at the ionization region is in all cases much greater than ρ we have $\rho_0 - \rho \approx \rho_0$, so substituting in equation (2.17):

$$\frac{1}{\rho_{L_{fl}}} - \frac{1}{\rho_0} = \frac{\mu}{\varepsilon_0} t \qquad \therefore \qquad \rho_{L_{fl}} = \frac{\varepsilon_0}{\mu \cdot t} \tag{2.19}$$

There is a saturation limit j_s to the unipolar drift current density along any field line of length L_{fl}, crossing a gap of voltage V [14]. As:

$$j_s = \rho_{L_{fl}} \cdot u_D \tag{2.20}$$

substituting from (2.20) we finally get:

$$j_s = \mu \cdot \varepsilon_0 \cdot \frac{V^2}{L_{fl}{}^3} \tag{2.21}$$

In fact, equation (2.21) represents the contribution of every single field line to the total corona drift current between the electrodes and can be used as a simplified approximation for the estimation of the current density distribution over the collecting electrode. The total corona drift current can then easily be estimated by integrating the current density over the whole surface of this electrode.

2.4 CURRENT DENSITY DISTRIBUTION

The first experimental indication of the peculiarities of unipolar space-charge-saturated ion drift was obtained by Warburg in 1899 [117, 118]. The current density distribution $j(\theta)$ over the plane in stationary point-plane discharges (see figure 2.9) was reported that followed the following formula closely:

$$j(\theta) = j_{s0} \cdot \cos^m \theta, \qquad \begin{cases} m = 4.82 \ \textit{Positive coronas} \\ m = 4.65 \ \textit{Negative coronas} \\ \theta < 60° \end{cases} \qquad (2.22)$$

where θ, is the emerging angle and j_{s0} is the maximum current density at θ=0..

This so-called Warburg distribution has since been amply confirmed and stands over a large range of corona currents and point-to-plane distances, although minor irregularities may occur near the axis [33]. The value of m is usually set equal to 5. For θ angles greater than 60° the current density usually falls rather abruptly to zero, indicating that field lines so far from the axis do not connect with the ionization region.
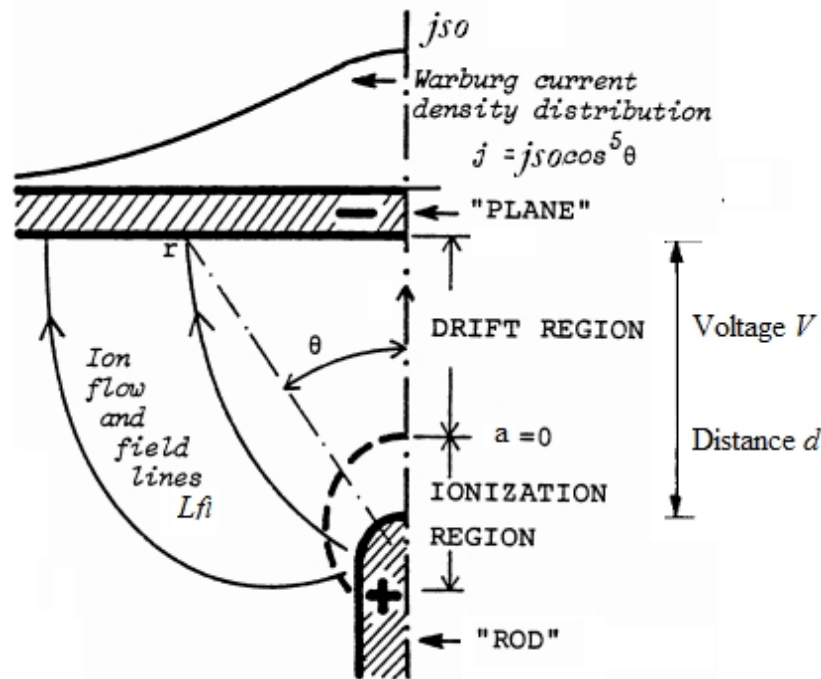
Figure 2-9 A typical point-plane corona geometry, with positive point. The surface a = 0 marks the outer limit of the ionization region [33].

2.5 IONIC WIND

The current that arises in the vicinity of the anode during the discharge, injects unipolar charges which drift towards the cathode with a speed u_D (m/s) proportional to the mean electric field as shown in equation (2.18).

During their drift along the electric field lines, charged ions collide with neutral air molecules and atoms, thus transferring their momentum and causing the ionic wind effect. The resulting wind is a combination of charged ions that drift towards the collector and neutral particles that gained momentum by collisions. The positively charged atoms and molecules have their charge neutralized when they reach the cathode and stop there, but the neutral particles, which acquired kinetic energy during the collisions, continue their travel even further.

The first expression of the ionic wind velocity has been derived by Robinson [6]:

$$u_D = k_G \cdot \sqrt{\frac{I}{\rho_{gas} \cdot \mu}} \tag{2.23}$$

where k_G (m$^{-1/2}$) is a geometrical factor, ρ_{gas} (kg/m^3) is the gas density and I (A) is the positive corona discharge current.

Sigmond and Lagstadt [119] introduced the function of the electrode gap d (m) and the discharge cross section A_{cs} (m^2) and fulfilled an expression for the ionic wind velocity:

$$u_D = \sqrt{\frac{I \cdot d}{\rho_{gas} \cdot \mu \cdot A_{cs}}} \tag{2.24}$$

In the case of the wire-cylinder arrangement, where the electric field is not uniform along the axis of the gap, the discharge cross section is a function of the distance between the wire and the cylinder. Thus, an expression for the discharge cross section A_{cs} may be derived from (2.23) and (2.24), by means of the electrode gap d and the geometrical factor k_G and can be used in the case of a wire-cylinder electrode configuration:

$$A_{cs} = \frac{d}{k_G{}^2} \tag{2.25}$$

Flow Limitation

Since drifting ions transfer their momentum to neutral air molecules by collisions taking place along their drift path [120] one could expect that the ion drift velocity is directly proportional to the air velocity generated by the moving neutral molecules downward the collector (see equation 2.18). In this way, an upper limit for the wind velocity may be defined, assuming single carrier conduction [121]:

$$u_{Dmax} = \sqrt{\frac{d \cdot j_{sat}}{\rho_{gas} \cdot \mu}} \tag{2.26}$$

where u_{Dmax} (m/s) is the maximum ionic wind velocity and j_{sat} (A/m^2) is the saturation current density over the cylindrical electrode.

2.6 GENERATED THRUST

As mentioned above, the corona current, flowing from the emitter towards the collector generates an air flow (*ion wind*) in the same direction, as moving positive ions collide with neutral air molecules, exchanging their momentum and, finally, accelerating them. The generated thrust is in fact a reaction force against the field force, so it can be approximated by the sum of all electric field forces acting on moving ions as follows [122]:

$$F = n_i \cdot A_{cs} \cdot d \cdot e \cdot E_{av} \tag{2.27}$$

where F (N) is the generated thrust due to the EHD effect, n_i is the ion density, A_{cs} (m^2) is the discharge cross section, d is the gap length (m), e is the unit charge (*charge of an electron*) and E (V/m) is the mean electric field.

The total charge Q can then be expressed as:

$$Q = N \cdot e \tag{2.28}$$

and the discharge current as :

$$I = \frac{dQ}{dt} = \frac{d}{dt}(n_i \cdot A_{cs} \cdot d \cdot e) = \frac{d}{dt}(n_i \cdot A_{cs} \cdot u_D \cdot dt \cdot e) = \tag{2.29}$$

$$= n_i \cdot A_{cs} \cdot u_D \cdot e = n_i \cdot A_{cs} \cdot \mu \cdot E_{av} \cdot e$$

From equations (2.27), (2.29) we finally get the following expression [122]:

$$F = \frac{d}{\mu} \cdot I \tag{2.30}$$

Equation (2.30) represents the relationship between the generated thrust and the corona discharge current in a uniform electric field with a constant discharge cross section A_{cs}. In the case of a wire-cylinder arrangement, the electric field is not uniform along the axis of the gap, so the discharge cross section is a function of the distance d between the wire and the cylinder. Thus, the thrust could be expressed as:

$$F_{wc} = n_i \cdot A_{cs}(d) \cdot d \cdot e \cdot E_{av} = n_i \cdot V_{wc} \cdot e \cdot E_{av} \tag{2.31}$$

where V_{wc} (m^3) represents an 'equivalent' ionic flow volume in the case of wire-cylinder arrangement (see figure 2-10) and E_{av} (V/m) is the average electric field intensity within this volume.

By combining equations (2.30) and (2.31), we have:

$$F_{wc} = f_c \cdot \frac{d}{\mu} \cdot I \tag{2.32}$$

In the above equation f_c is introduced as a 'field coefficient' for the wire-cylinder arrangement, defined as:

$$f_c = \frac{V_{wc}}{V_{hom}} \cdot \frac{E_{av}}{E_{hom}}$$

<div align="right">(2.33)</div>

where V_{hom} (m^3) is the ionic flow volume that should be considered for a homogeneous electric field (e.g. between parallel plates) across the same gap d and voltage V, where the mean field strength E_{hom} would be equal to the ratio V/d. It should be noted that f_c may be considered as a measure of the electric field inhomogeneity and equals 1 for a totally homogeneous electric field.
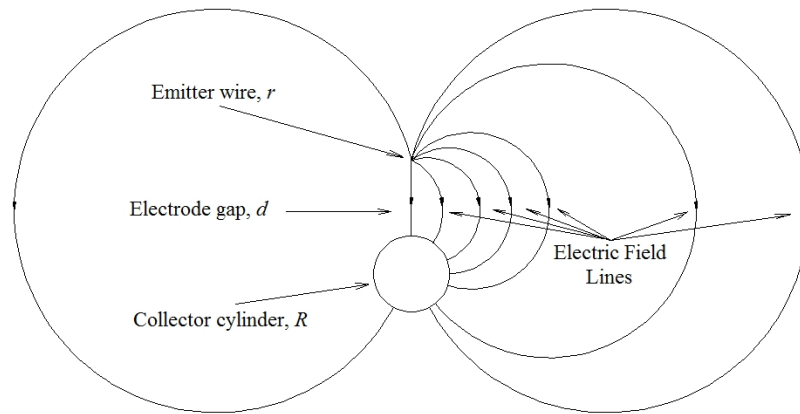
Figure 2-10 Graphical representation (on plane) of the moving ions trajectories along the field lines, which define the boundaries of the ionic flow volume.

CHAPTER 3 - EXPERIMENT AND SIMULATIONS

The electric field and potential distribution in typical wire-cylinder electrode arrangements, under HV DC application, will be studied by implementing the Finite Element Analysis (FEA). On this purpose, open source FEA modelling software F.E.M.M. (Finite Element Method Magnetics) ver. 4.2 and dedicated Multiphysics software COMSOL ver. 4.3a will be used.

On the other hand, experiments will be conducted so as to determine the relationship between the electric corona discharge current, the corresponding ionic wind velocity, the generated thrust due to the EHD effect and the applied high voltage, as well as their dependence on geometrical characteristics of the electrodes such as the electrode length, the electrode gap and the emitter and collector radii. In addition, the CIV in each case will be experimentally determined and the results will be verified with simulation results, as well as with empirical values.

3.1 ELECTRODE GEOMETRY

In order to study the EHD phenomenon in a wire-cylinder electrode arrangement, a set of experimental assemblies were carefully prepared. The physical model of the electrode configuration under examination is being displayed in figure 3-1.

The influence of the electrode material (e.g. copper, aluminum, steel, and zinc), has no effect on the nature of the EHD effect [11], hence copper and aluminium have been used for the wire-cylinder electrode fabrication. Each module consisted of a thin polished copper wire with radius *r* (*emitter*) and an aluminum cylinder (*collector*) with radius *R*, while the electrode length was *L*. Both electrodes were fixed on a polyethylene frame parallel to each other, at distance *d*.

Since the corona discharge is strongly dependent on the electric field inhomogeneity, which, in turn, controls the space charge generation by air ionization at the inter-electrode space, different *R/r* and *d/r* ratios have been used, as shown in table 3-1.
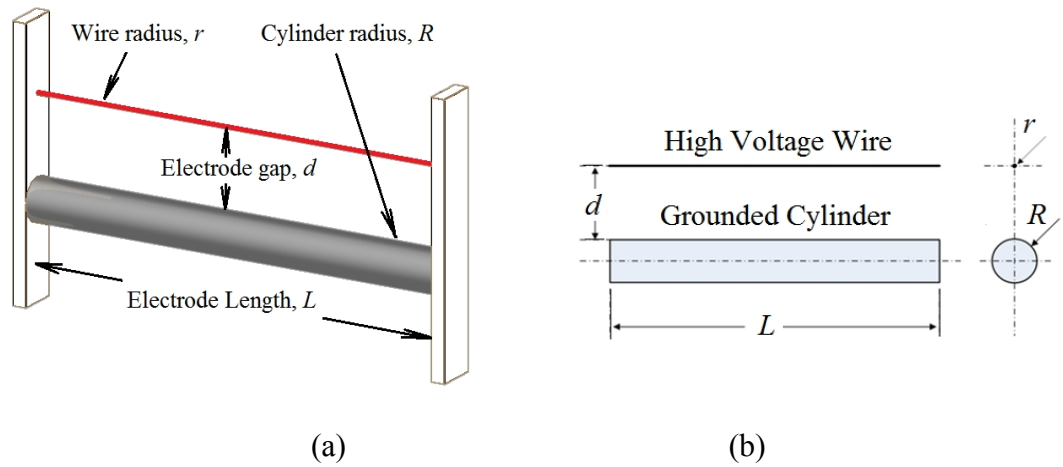
Figure 3-1 (a) The structure of the experimental module and (b) detailed diagram of the module where the wire (emitter) and cylinder (collector) are shown.

Table 3-1 Geometrical characteristics of the wire-cylinder electrode pair - Dimensions.

Gap distance d (cm)	1, 2, 3, 4, 5
Wire radius r (μm)	30, 50, 100, 250, 400
Cylinder radius R (mm)	5, 10, 15, 20
Electrode length L (mm)	100, 200, 300, 400, 500
R/r ratio	12.5 - 667
d/r ratio	75 - 1667

The wire-cylinder electrode pair under consideration for the FEA modelling is shown in figure 3-2. A thin wire of radius r is placed parallel to a cylinder with significantly larger radius R, at distance d. The wire radius r, the cylinder radius R and the air gap d between the electrodes are critical parameters which define the geometry and, in this way, determine the electric field strength. In this study, r ranged between 1 and 500μm, R between 1 and 20mm, while the gap d between the electrodes ranged between 1 and 10cm. In fact, the FEA model of the wire-cylinder electrodes shown in figure 3-2 is an accurate representation of the manufactured real experimental modules shown in figure 3-1, which have been used during laboratory tests under HV application.

(a)   (b)
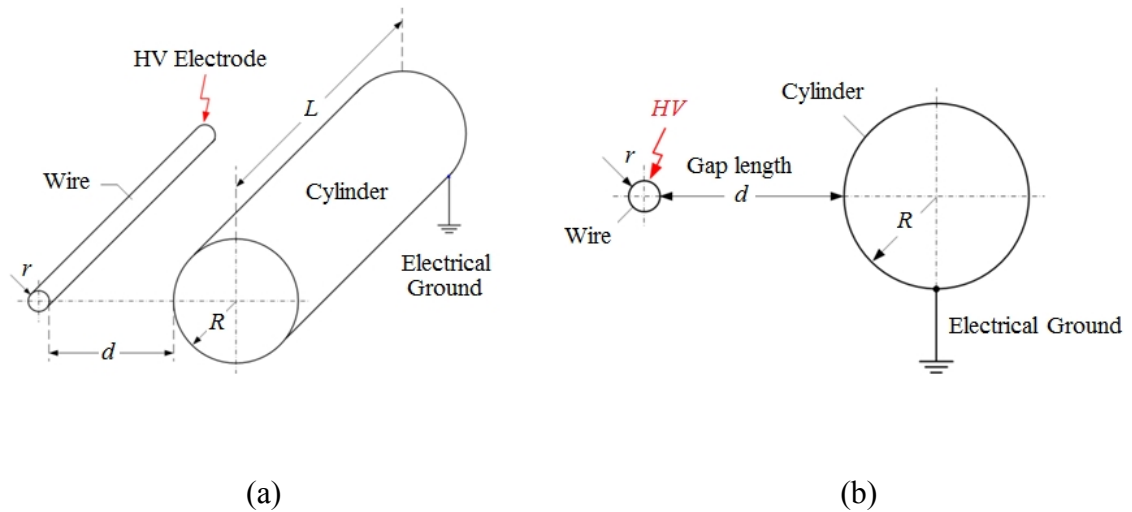
Figure 3-2 (a) Perspective plan of the electrodes arrangement in space and (b) simplified planar model, due to longitudinal axis symmetry.

Theoretically, the electrodes of figure 3-2 may have infinite length, but due to the longitudinal axis symmetry, the electric field or potential distribution may only change in the radial direction, perpendicular to the wire or the cylinder surface, along the gap. Therefore, this three-dimensional problem may be minimized into a two-dimensional problem that requires a much smaller number of nodes and less computing power.

3.2 FEA MODEL

FEA modelling in electrostatics is based on the application of a set of differential equations that describe the problem, considering certain boundary conditions, in order to come to a unique solution. FEA modelling breaks the problem down into a large number of regions, each with a simple geometry (e.g. triangles), defined by a mesh with a very large number of nodes. Then the problem is transformed from a small but difficult to solve problem into a big but relatively easy to solve, involving a very large number of unknown quantities.

In our case, fine modelling and analysis of the electric field strength in a wire-cylinder electrode arrangement in atmospheric air, at normal conditions has been carried out based on FEA techniques, considering the geometrical characteristics of the electrodes.

The mesh parameters of F.E.M.M. ver. 4.2 have been thoroughly investigated in order to optimize the applied mesh around the specific areas of interest, thus ensuring the accuracy of the results. These areas may be the conductor's surfaces, as well as the inter-electrode region and especially the points along the line defining the shortest distance d between the electrodes. On the other hand, the element size parameters of COMSOL ver. 4.3a have been optimized for the resolution of correct generation of field lines since the mesh formation may affect the field line distribution and lead to inaccuracies.

In addition, the determination of the bounding box size is generally critical, since a small box may affect the electric field distribution and lead to errors, or, on the other hand, a large box may unnecessarily lead to a very large number of nodes, demanding more processing power.

Governing Equations

In our case a typical electrostatics problem has been defined, which is governed by the well-known Gauss's and Poisson's equations, assuming homogenous field and steady state conditions [94-96]:

$$E = -\nabla V \tag{3.1}$$

$$\nabla^2 V = -\frac{\rho}{\varepsilon_0} \tag{3.2}$$

where E is the electric field intensity, V is the applied voltage, ρ is the space charge density and ε_0 is the dielectric permittivity of air. The electric field should satisfy the charge conservation law:

$$\nabla \cdot j = 0 \tag{3.3}$$

where j is the current density. The latter is defined as:

$$j = \rho \cdot u = \rho \cdot \mu \cdot E \qquad\qquad (3.4)$$

where u is the ion drift velocity and μ is the ion mobility. (3.1), (3.2), (3.3) and (3.4) can be combined to obtain:

$$\nabla\{(\nabla^2 V)(\nabla V)\} = 0 \qquad\qquad (3.5)$$

In theory, the physical problem is reduced to the mathematical problem of solving equation (3.5) with the appropriate boundary conditions. This complex equation has been solved analytically only for simple geometries where the voltage can be expressed as a function of a single coordinate (e.g. concentric wire-cylinder setup [8]). In other cases where two or more coordinates are required the problem becomes very hard to treat symbolically; however numerical solutions can easily be found by FEA [123, 124].

The FEA method provides numerical results for the voltage distribution at each node of the applied mesh. The electric field strength may then be easily determined by (3.1) around the user-defined domain, where the mesh is constructed. In such a computational analysis, the solver precision, the boundary conditions, the bounding box size defining the domain and the mesh distribution are of great importance for the accuracy of the results [125-128].

FEA Modelling Parameters

The FEA analysis is based on the solution of equation (3.5) for the potential V, over the user defined domain with the user defined sources and boundary conditions. It discretizes the problem domain using triangular elements, which form a mesh consisting of a large number of nodes. The solution over each element is approximated by a linear interpolation of the values of potential at the three vertices of the triangle [129]. In our case, a two-dimensional planar electrostatic problem was defined with a solver precision equal to 10^{-8}.

Dirichlet conditions were explicitly defined on the problem's boundaries [130]. The wire and cylinder outer surfaces were considered to be equipotentials with fixed

voltages 1kV and 0V, respectively. Subsequently, all electric field strength results were defined per kV of the applied voltage. Since the applied voltage may vary in practice, valid results may be easily obtained in any case, by just multiplying the electric field strength at 1kV, by the number of applied kilovolts. This can be easily explained by equation (3.1). For example, considering any fixed pair of wire-cylinder electrodes with 1kV voltage difference, then, if $V_1(x, y)$ is the potential and $E_1(x, y)$ is the corresponding electric field strength at any point *(x, y)*, then, at *akV*, the potential would be $V_a(x, y) = aV_1(x, y)$ and the corresponding electric field strength $E_a(x, y)$ could be determined by equation (3.1) as follows:

$$E_a(x,y) = -\nabla V_a(x,y) = -\nabla\big(a \cdot V_1(x,y)\big) = a \cdot \big(-\nabla V_1(x,y)\big) = a \cdot E_1(x,y) \quad (3.6)$$

It becomes clear from the proportionality of equation 3.6, that the electric field strength at *akV* equals *a* times the electric field at 1kV.

Due to the symmetry of the electrode geometry along the gap axis, half-plane modelling has been applied. The problem's domain was defined by the bounding box shown in figure 3-3. This box sets the limits of the surrounding dielectric medium, which in our case was atmospheric air. The bounding box size was defined by the fixed distances $A_{BOX} = k_{BOX} \cdot D_{BOX}$ between its sides and the wire-cylinder electrodes, where $D_{BOX} = 2r + d + 2R$ was the total length of the electrodes assembly (air gap included) and k_{BOX} was a scaling constant.
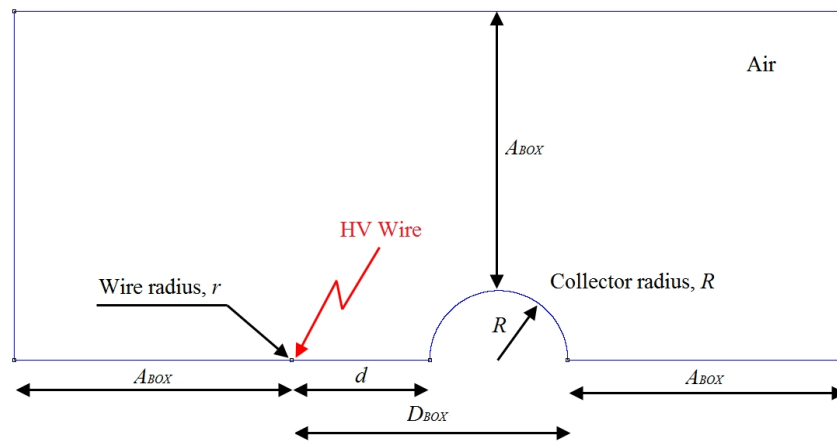
Figure 3-3 The model of the two electrodes and the bounding box of the surrounding air, where the mesh is applied.

Numerical analysis has been carried out on the electric field intensity for different k_{BOX} values in order to determine the ideal bounding box size which is critical, since the electric field distribution may be affected by small boxes. The geometrical dimensions of the electrodes were r=25μm, R=15mm and d=3cm, while the mesh formation parameters were set on the program default values, as shown in table 3-2.

Table 3-2 F.E.M.M. ver. 4.2 default values for the mesh parameters.

Minimum angle (Degrees)	Maximum arc segment (Degrees)	Local element size (μm)	Mesh size (μm)
30	5	Auto	Auto

The simulation results showed that the maximum electric field intensity E_{max} values converge with the box size. Similar results have been obtained for other geometrical characteristics of the electrodes as well. Therefore, a suitable choice for the bounding box size, taking into account the number of nodes as well (see figure 3-4), would be for $k_{BOX} = 3$, ($A_{BOX} = 3D_{BOX}$) and can be considered as adequate for further analysis. This value had been kept constant throughout all simulations.
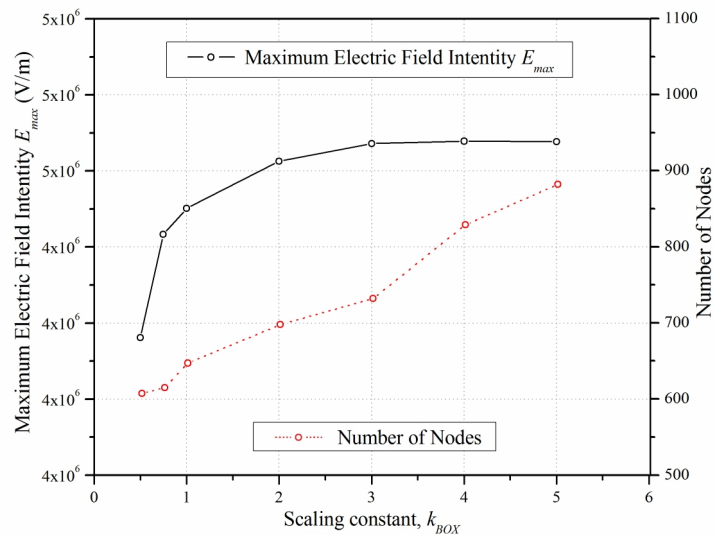
Figure 3-4 Maximum field intensity and applied mesh nodes with k_{BOX} (multiplier of distance D_{BOX}, $A_{BOX} = k_{BOX} \cdot D_{BOX}$).

There is a set of key parameters to the F.E.M.M. model so as to ensure proper mesh formation. The mesh discretization at distances very close to the electrode surfaces depends mainly on two parameters, *the maximum arc segment degrees* and the *minimum angle*. These determine the size of the triangular elements near the outer surface of the electrodes, where the electric field and voltage gradients get their maximum values, thus demanding very fine analysis by a dense mesh. On the other hand, the mesh distribution along the gap is a function of the *local element size along line* parameter. The density of the mesh elements in other areas such as the inter-electrode space away from the electrode surfaces are functions of another key parameter, the *mesh size*.

The mesh generation, using the default F.E.M.M. ver. 4.2 values for the mesh key parameters, is presented in figure 3-5. The wire-cylinder electrode pair in this case also had dimensions r=25μm, R=15mm, d=3cm and the bounding box size had a fixed distance $A_{BOX} = 3D_{BOX}$ away from the electrodes.
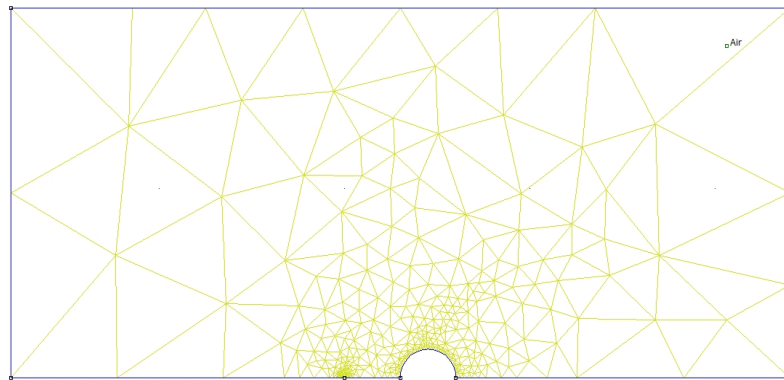
Figure 3-5 Generated mesh for the default values of the mesh formation parameters (r=25μm, R=15mm, d=3cm and $A_{BOX} = 3D_{BOX}$).

It can be seen that the mesh is not quite dense in the areas of interest and the results may lack of accuracy. The default mesh generation consists of 732 nodes and 1303 elements. Mesh optimization is needed in this case by adjusting the mesh formation parameters. Analytical study of the influence of each one of the mesh parameters has been carried out, by running a large number of simulations, using different *maximum arc segment angles*, *minimum angles of the triangular mesh*, *local elements size along line* and *mesh sizes*, in order to accomplish convergence of the

results. In this way an optimal mesh has been configured, in terms of accuracy and processing power consumption, with the key parameter values given in table 3-3.

Table 3-3 Comparison between the F.E.M.M. ver. 4.2 default values of the mesh key parameters and the optimized values.

FEMM key parameter	Default values	Selected values (*optimized*)
Minimum Angle (degrees)	*30*	*31*
Maximum Arc Segment (degrees)	*5*	*0.5*
Local Element Size Along Line (μm)	*auto*	*10*
Mesh Size (μm)	*auto*	*auto*
Nodes	*732*	*25858*
Elements	*1303*	*47870*

An example of the optimized mesh formation is shown below, in figure 3-6. The higher mesh density in the areas of interest can be easily seen (i.e. near the high voltage and the grounded electrode, as well as along the wire-cylinder gap axis).

DETAILED AREA OF INTEREST
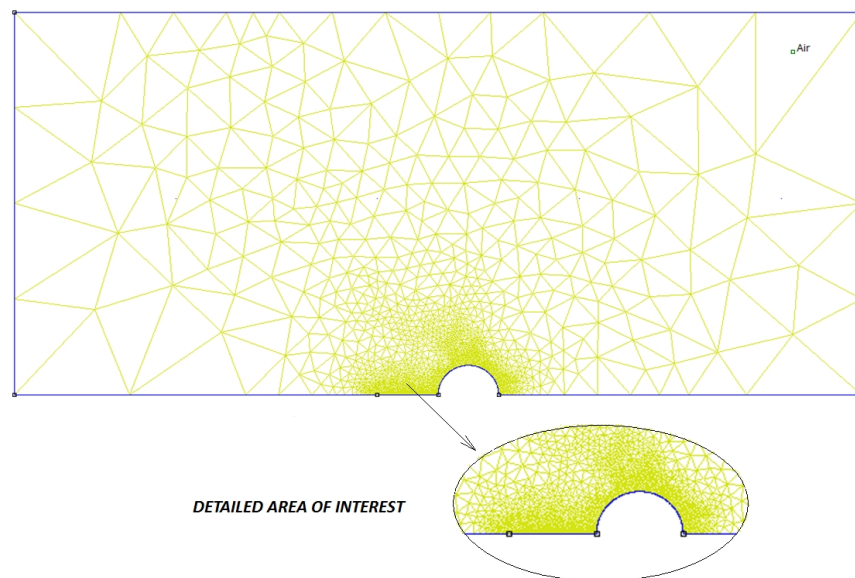
Figure 3-6 Optimized mesh formation and detail of the area of interest where the fine mesh generation is shown.

As far as the COMSOL ver. 4.3a modelling parameters are concerned, the maximum and minimum element size limits had been set at 700μm and 1μm, respectively. According to previous studies [131], the minimum element size needs to be at least 25% of the smallest simulated geometrical dimension of the electrodes so that accurate results can be retrieved.

The smallest dimension for COMSOL ver. 4.3a FEA analysis was the 50μm radius of the wire; therefore, the minimum element size was only a 2% fraction of the smallest simulated geometrical dimension. Triangular elements have been used for the required mesh construction throughout the FEA simulations as well.

Verification of the mesh formation

For verification purposes, the optimized mesh has been used in order to estimate the maximum field intensity E_{max}, at well-known geometries, similar to the wire-cylinder electrode pair, such as two identical wire conductors in parallel (where R/r=1), for which analytical formulas can be found in bibliography [92]. In this way, the accuracy of the optimized mesh could be easily tested. In the case of two identical wires of radius r, fixed parallel to each other at distance d, the maximum electric field intensity is given by equation (2.4).

F.E.M.M. ver. 4.2 simulations that have been conducted with the optimized applied mesh, for geometrical characteristics of the electrodes within the limits of our study, have provided results which are in good agreement with theoretical expectations in all cases. Such results are given in table 3-4, where both theoretical and simulation values for E_{max} are shown, along with the corresponding relative error.

Table 3-4 Comparison between the E_{max} (theoretical and F.E.M.M. ver. 4.2 simulation results) for two identical wire conductors in parallel, at 1kV potential difference.

r (μm)	d (cm)	Theoretical E_{max} (V/m)	Optimized Mesh results E_{max} (V/m)	Relative error (%)
1	1	$54.296 \cdot 10^6$	$54.183 \cdot 10^6$	0.21
25	3	$2.825 \cdot 10^6$	$2.803 \cdot 10^6$	0.78
100	5	807250	799771	0.93
250	7	357014	353483	0.99
500	10	190261	187465	1.47

3.3 EXPERIMENTAL SETUP

Laboratory measurements have been carried out in order to specify the total corona discharge current flowing between the wire and cylinder electrodes, at different voltage levels. In addition, the corresponding ionic wind velocity and the generated thrust due to the EHD effect have been recorded. On that purpose, thin copper wires and aluminum cylinders of appropriate diameter were used as emitter and collector electrodes respectively and experimental setups have been created in order to carry the investigations.

A schematic of the experimental setup is given in figure 3-7. The high voltage was supplied to the emitter by an adjustable high voltage power source (*Matsusada Precision W Series*) while the collector was electrically grounded. A voltmeter combined with a *Coline HV40B 40 kV* (1000:1) high voltage probe has been used for measuring the DC high voltage applied to the emitter electrode, with an accuracy of 1%. Positive corona discharge current readings have been acquired by a high precision ammeter (*Metra Hit 28s*) with 1nA sensitivity, connected in series between the collector and the electrical ground.
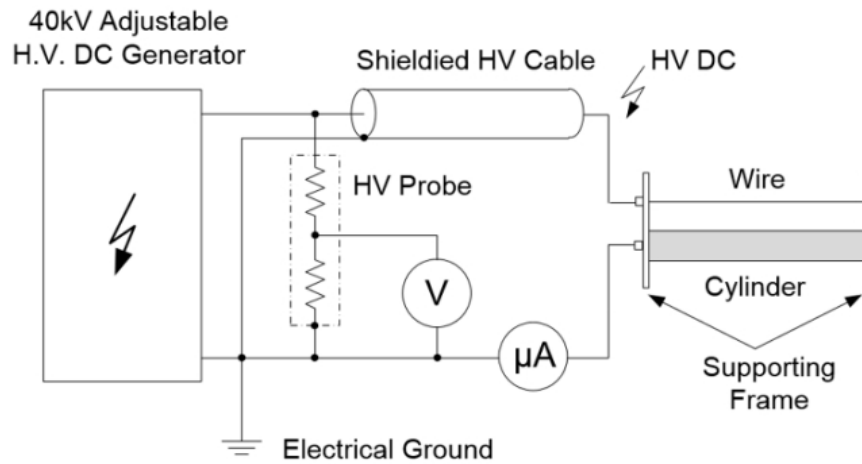
Figure 3-7 Experimental setup for corona current readings.

The velocity of air flow, which was generated due to the gas discharge, has been recorded on a *Testo 425* thermal anemometer. The permanently attached telescopic handle of the anemometer could be extended up to 820mm, while the probe head had a diameter of 7.5mm. The accuracy of the instrument was ±0.03m/s within the operational range of the device (0-60°C), while the sampling rate was 2bit/s. For the ionic wind measurements, the hot-wire flow probe has been placed close to the lower surface of the cylindrical electrode, where the maximum values of ionic wind velocity were detected. In order to determine where the maximum values of the wind velocity were produced; measurements have been made in altered placements of the flow probe in the vertical and the horizontal axis of the experimental setup.

The generated thrust, due to the EHD effect, has been detected and measured as a reduction in weight of the electrode system with a *Kern 572-32* precision electronic balance with 1mg resolution. A schematic of the experimental setup is shown in figure 3-8. As shown in figure 3-8, the electrode setup hung freely, by a thin cotton thread, which was available at the bottom of the precision balance. The overall weight of the wire-cylinder electrode assembly was approximately 400gr. The balance stand, containing the electrodes, was isolated from outside air disturbances by the use of detachable plexiglas covers, forming in this way a closed box. This arrangement ensured undisturbed EHD flow between the electrodes. The box length was 90cm, while the width and the height were 70cm and 100cm respectively.

(a)

(b)
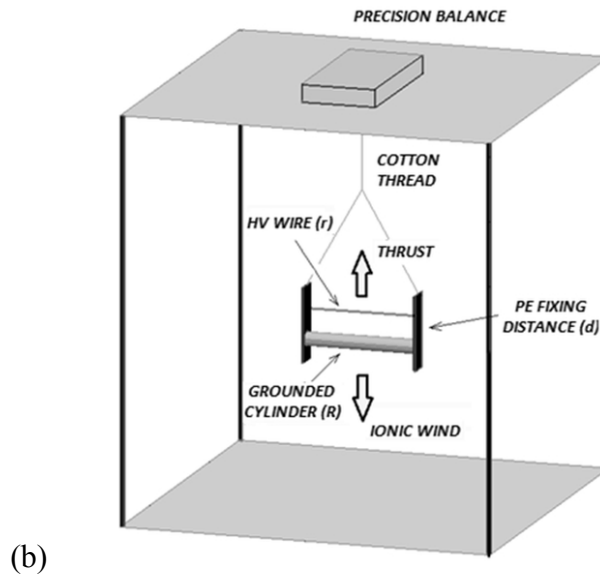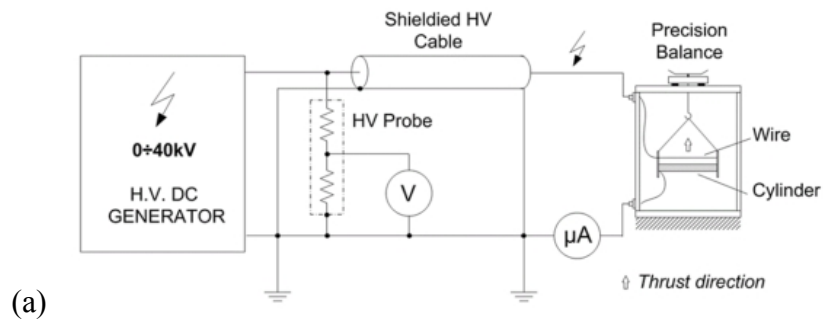
Figure 3-8 (a) Schematic of the experimental setup for generated thrust measurements and (b) perspective view of the electrode setup with the supporting construction.

All the experiments have been performed in atmospheric air, with conditions which were monitored as summarized in table 3-5. All measurements were made by applying high DC voltage to the anode with 1kV increments above the corona inception threshold and relatively close to the breakdown voltage of each gap.

Table 3-5 Experimental Conditions.

Parameter	Method of measurement	Range of variation
Temperature	K-type thermocouple	23.1 - 26.3°C
Pressure	Local weather station	994 - 1012.6mbar
Relative humidity	SC and polymer capacitive sensor	33.2 - 60.8%

CHAPTER 4 - FEA SIMULATION RESULTS AND DISCUSSION

As expected, the simulation results have shown that the maximum electric field strength E_{max} is located at the outer surface of the wire electrode, at the least distant point from the cylinder (see figures 4-1a, 4-2a and 4-4), while the minimum field strength E_{min} has been identified at distance x, depending on the R/r ratio (see figure 4-4).

On the other hand, the potential distribution across the electrode gap d is shown in figures 4-1b and 4-2b, where it becomes clear that equipotentials are in fact cylindrical surfaces with displaced centers along the gap axis.

A detailed plot of the electric field distribution near the high voltage wire electrode where E_{max} is shown, and the surrounding area of the ionization region a (E_a) is displayed in figure 4-3.
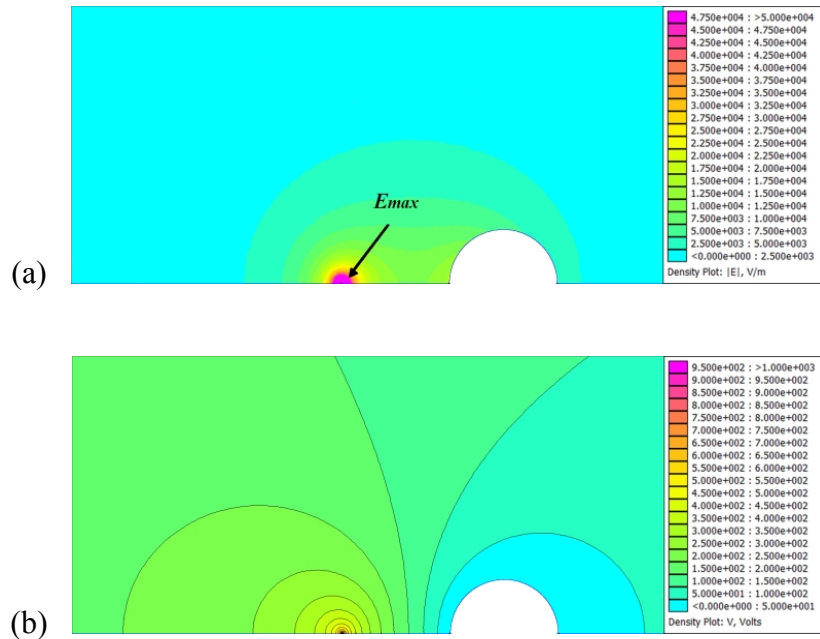
Figure 4-1 (a) Electric field strength and (b) potential distribution. Wire-cylinder electrodes with r=25μm, R=15mm and d=3cm, at 1kV potential difference.

(a)

(b)
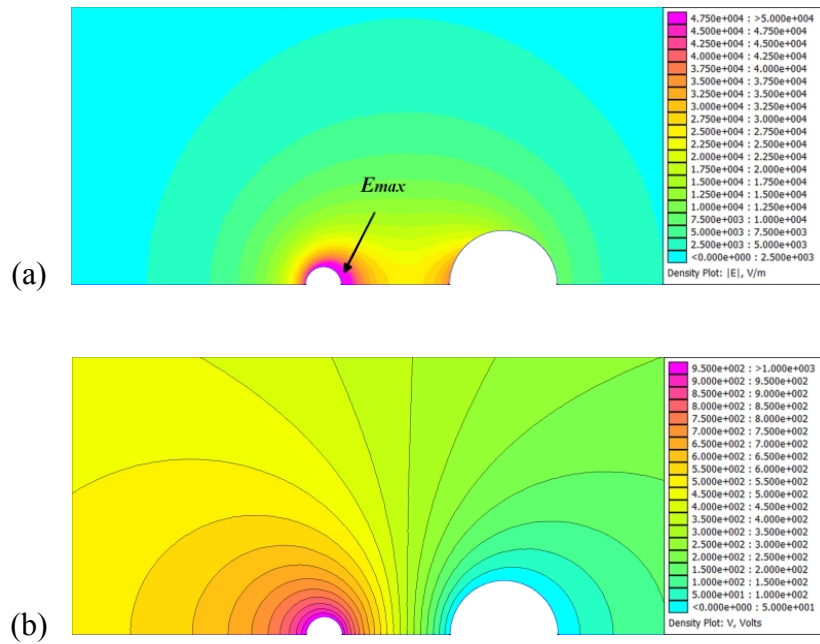
Figure 4-2 (a) Electric field strength and (b) potential distribution. Wire-cylinder electrodes with r=5mm, R=15mm and d=3cm, at 1kV potential difference.
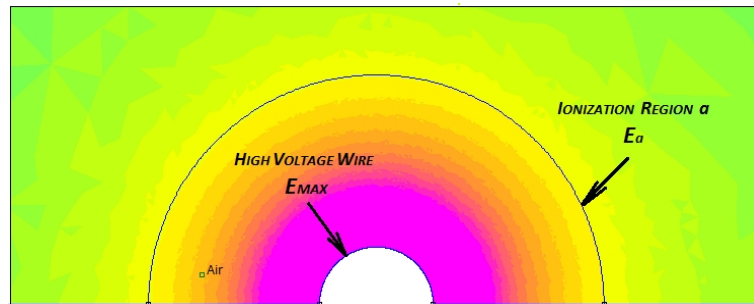
Figure 4-3 Detailed plot of the electric field distribution near the emitter and the ionization region area (the ionization region area was derived according to equation 2.8).

The variation of the electric field intensity across the gap, for different R/r ratios is given in figure 4-4, where the normalized field $E(x)/E_{max}$ is shown, at distance x from the wire's surface, expressed as a percentage of the total electrode gap length d. It can be seen that the field intensity gets its maximum value at the wire's surface (where x=0 or x/d=0%) then diminishes along the gap until its minimum value and, finally, increases at a certain level depending on the R/r ratio, at the cylinder's surface (where x=d or x/d=100%). From another point of view, R/r ratio may be considered as a measure of the electric field inhomogeneity, since larger R/r ratios result in a more inhomogeneous field distribution along the gap (see figure 4-4).
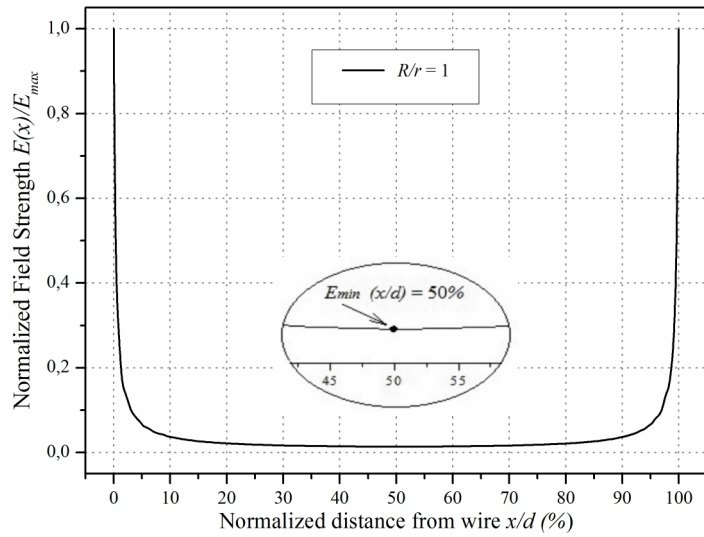
(a)
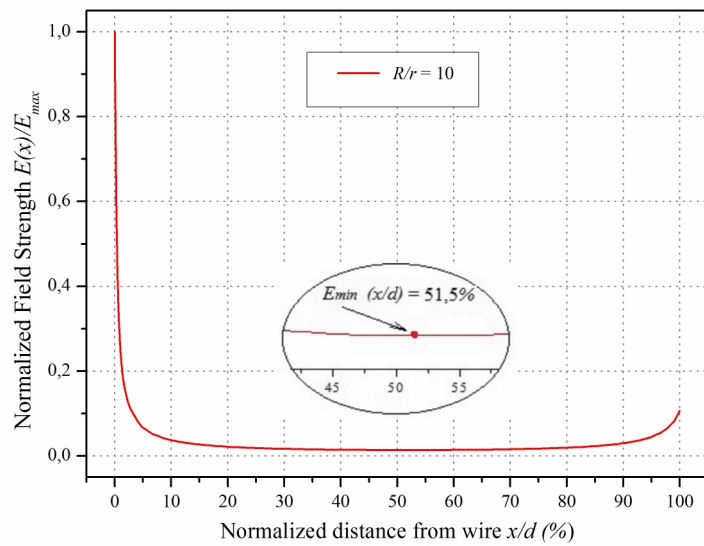
(b)
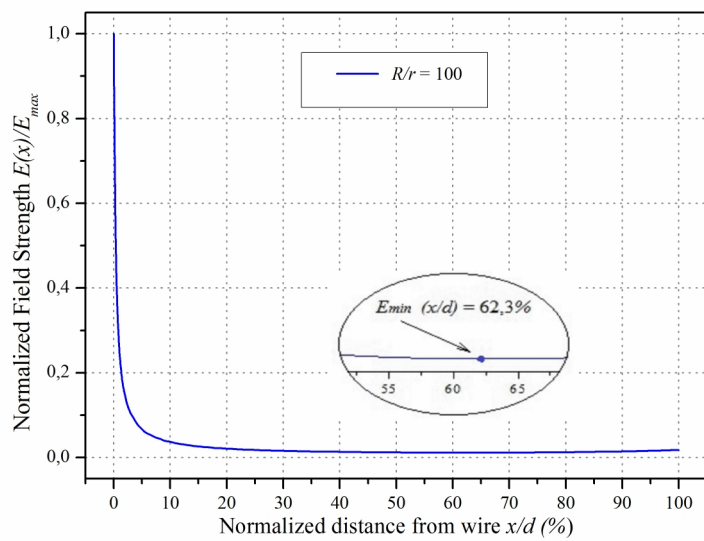
(c)

Figure 4-4 Normalized electric field intensity along the gap axis, and detail where E_{min} is shown. In this case r=100μm, d=3cm and (a) R/r=1, (b) R/r=10 and (c) R/r=100. Similar results can be obtained for different d and r values as well.

The variation of the electric field intensity along the gap axis, for R/r=600 and different gaps, is shown in figure 4-5. The field intensity seems to fall abruptly after 10% of each gap (especially in the case of large gaps) and remains below the mean field intensity in all cases. It becomes clear that large gaps produce more homogeneous fields, thus E_{min} moves closer to the centre of the distance between the electrodes as the gap increases (see figure 4-5). On the other hand, the potential distribution along the axis of the electrode gap changes slightly for different distances d between the wire-cylinder electrodes as shown in figure 4-6. Similar results have been obtained for other R/r ratios and d values, as well.
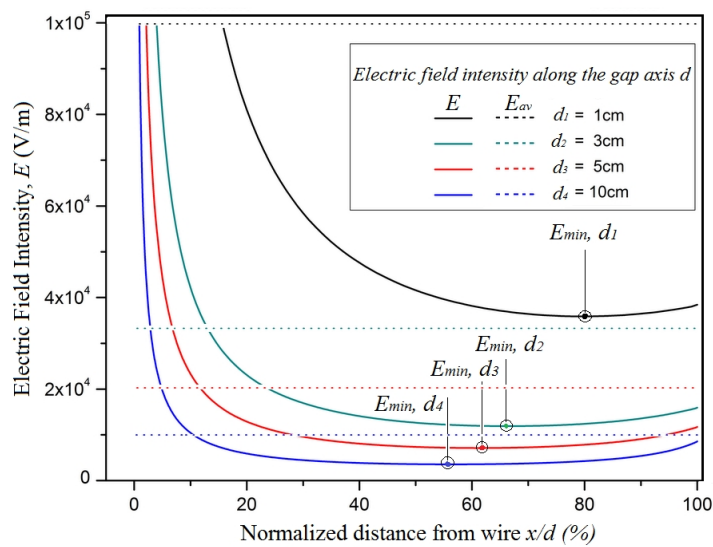
Figure 4-5 Electric field intensity along the gap axis (R/r=600 and d=1-10cm).
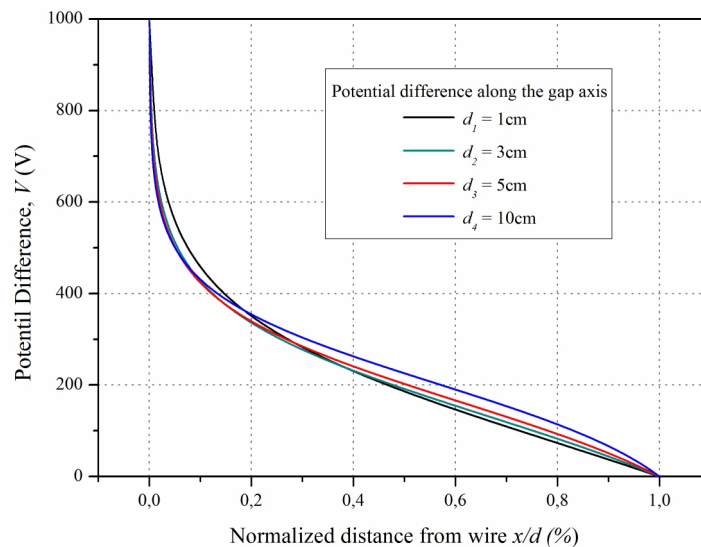
Figure 4-6 Potential distribution along the gap axis (R/r=600 and d=1-10cm).

The dependence of the maximum electric field intensity E_{max} on the wire radius r, the cylinder radius R and the electrode gap d has also been examined. Figure 4-7 shows typical curves of E_{max} versus d/r ratio, for different gaps d and cylinder radii R, while figure 4-8 shows the variation of E_{max} versus d/R ratio for different wire radii r and gaps d. From these results, it becomes clear that E_{max} is strongly affected by the d/r ratio, in a linear way, and secondly, by the d/R ratio.
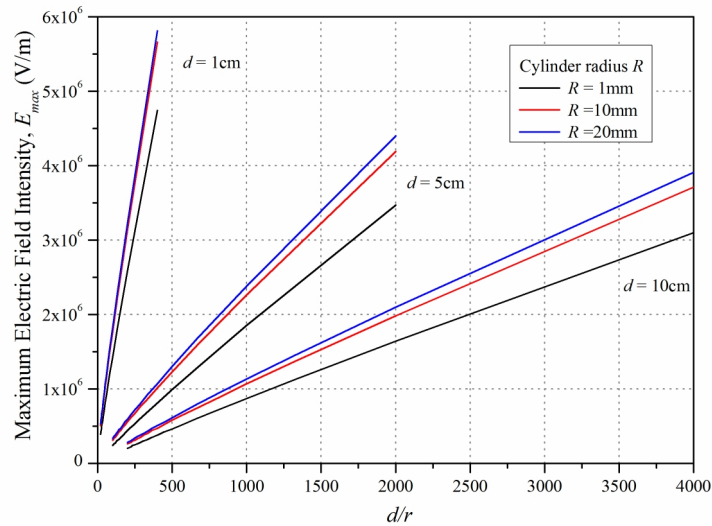
Figure 4-7 Variation of E_{max} with the d/r ratio. Electrode gap d at 1cm, 5cm and 10cm and potential difference 1kV in all cases.
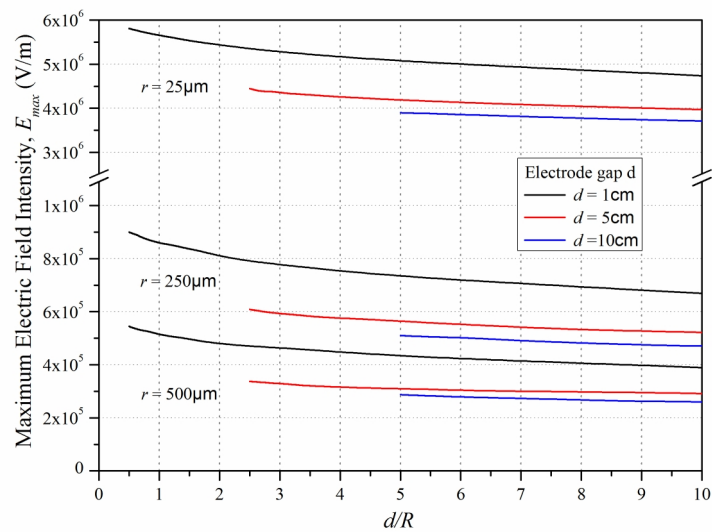
Figure 4-8 E_{max} variation with the d/R ratio. Wire radius r at 25μm, 250μm and 500μm and potential difference at 1kV in all cases.

Gap distance d remains a critical parameter in all cases. Generally, high electric field intensities can be reached by using thin wires, small electrode separation gaps and large cylinder radii, which is a reasonable finding, since the electric field distribution is thus becoming strongly inhomogeneous. On the other hand, figures 4-9 and 4-10 show how the minimum field strength E_{min} along the gap axis is affected by d/r, d/R and the electrode gap d. Here it seems that the gap distance d is the dominant parameter, while the wire radius r comes next.
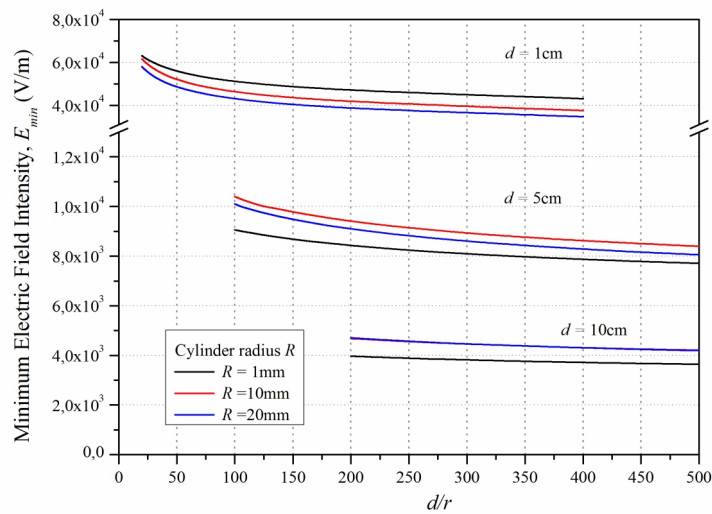
Figure 4-9 Variation of E_{min} with the d/r ratio. Electrode gap d at 1cm, 5cm and 10cm and potential difference at 1kV in all cases.
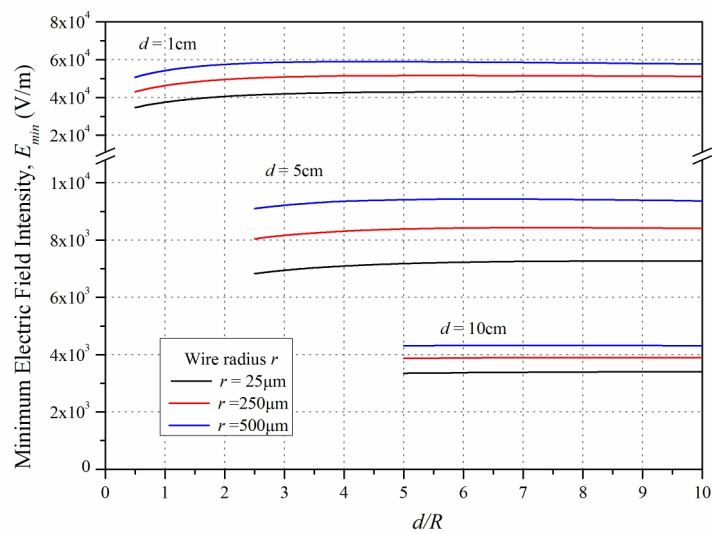
Figure 4-10 E_{min} variation with the d/R ratio. Wire radius r at 25μm, 250μm and 500μm and potential difference at 1kV in all cases.

4.1 PROPOSED FORMULA FOR E_{MAX} IN THE CASE OF WIRE-CYLINDER ELECTRODE ARRANGEMENT

According to simulation results, E_{max} increases linearly with d/r ratio. On the other hand, it is also dependent on the d/R ratio. The gap distance d is found to be critical in determining the electric field in all cases. This comes in agreement with theoretical expectations, since the ratio V/d is frequently used in bibliography as a standard measure of the mean value of the electric field strength in any gap [16-21]. Besides, most of the formulas for E_{max} in well-known geometries are usually expressed as the product of V/d by a geometrical constant, as in equation (2.4) [94-96]. According to the above, an effort has been made to introduce a formula for the maximum electric field strength E_{max} in the wire-cylinder arrangement.

Detailed analysis of all simulation results has shown that the maximum electric field intensity $E_{max\ wc}$ within the limits of this study can be approximated by the following formula:

$$E_{max\ wc} = \frac{V}{d} \cdot \frac{\gamma_1}{ln[\gamma_1 \cdot (\gamma_2 + 2)]} \tag{4.1}$$

where V (V) is the applied voltage, $\gamma_1 = d/r$ and $\gamma_2 = d/R$ (dimensionless factors).

On the other hand, similarly defining $\gamma' = d/2r$ in equation (2.4), we have:

$$E_{max\ ww} = \frac{V}{d} \cdot \frac{\sqrt{\gamma' \cdot (\gamma' + 2)}}{\ln\left[(\gamma' + 1) + \sqrt{\gamma' \cdot (\gamma' + 2)}\right]} \tag{4.2}$$

It should be noted that in the case of two identical cylindrical conductors in parallel $r=R$ ($\gamma_1 = \gamma_2 = \gamma$) and for $d \gg r$ we have $\gamma \gg 1$, $\gamma + 2 \approx \gamma$. Then (4.1) becomes:

$$E_{max\ wc} = \frac{V}{d} \cdot \frac{\gamma}{2 \cdot \ln(\gamma)} \tag{4.3}$$

In fact (4.3) equals (4.2) for $d >> r$, since $\gamma' >> 1$, $\gamma'+1 \approx \gamma'$ and $\gamma'+2 \approx \gamma'$ (also considering that $\gamma' = \gamma/2$).

The results of equation (4.1) for all possible combinations of the critical geometrical parameters r, R and d, within the limits of this study ($r \leq 500\mu m$, $R \geq 1mm$ and $d \geq 1cm$), are in good agreement with the corresponding maximum field intensity E_{max} values estimated by the FEA simulation.

Typical graphs of the change in relative error for E_{max} with the geometrical parameters r, R and d are given in figure 4-11. These graphs show that the error diminishes as d and R increase with respect to the wire radius r.
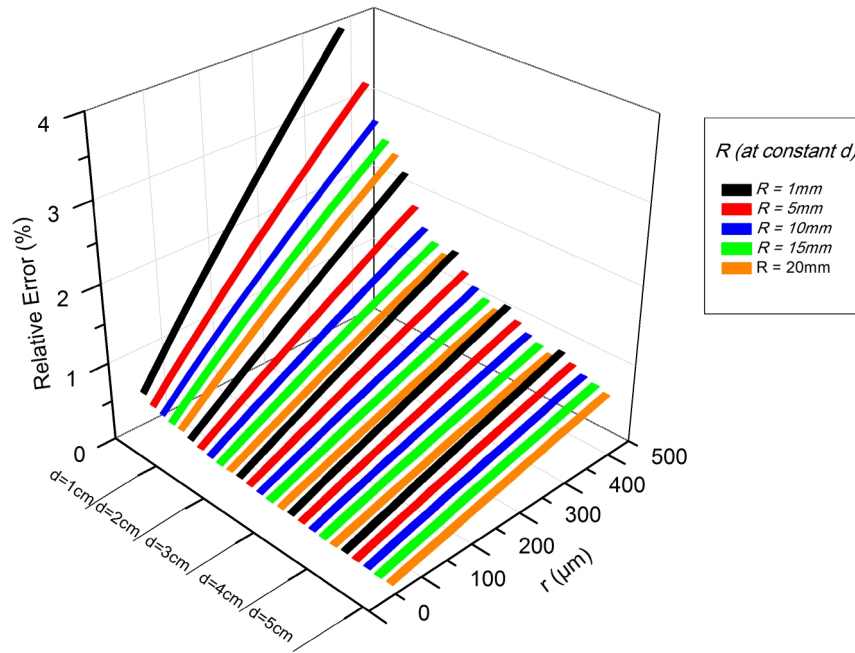
Figure 4-11 Representation of the relative error between simulated data and the empirical formula results for E_{max} according to equation (4.1).

According to figure 4-11, the relative error remains small, below 4 % (worst case) and decreases with increasing gap d and cylinder radius R.

Practically speaking, the proposed formula for E_{max} can be effectively used for electrode pairs constructed by thin wires parallel to cylinders of considerably larger radii at distances of a few centimeters or more. Such electrode arrangements have been

used in previous works [88-91] and are suitable for corona or ionic wind applications, due to the high inhomogeneity of the produced electric field. The determination of the maximum electric field in these cases is always one of the most critical design parameters.

Moreover, the electric field utilization factor (equation 2.7) which is frequently used to indicate the electric field inhomogeneity [132] can be easily defined from equation (4.1) as:

$$f_{wc} = \frac{\gamma_1}{ln[\gamma_1 \cdot (\gamma_2 + 2)]} \tag{4.4}$$

According to simulation results, the variation of the field utilization factor f_{wc} with R/r ratio in a constant electrode gap d is presented in figure 4-12.
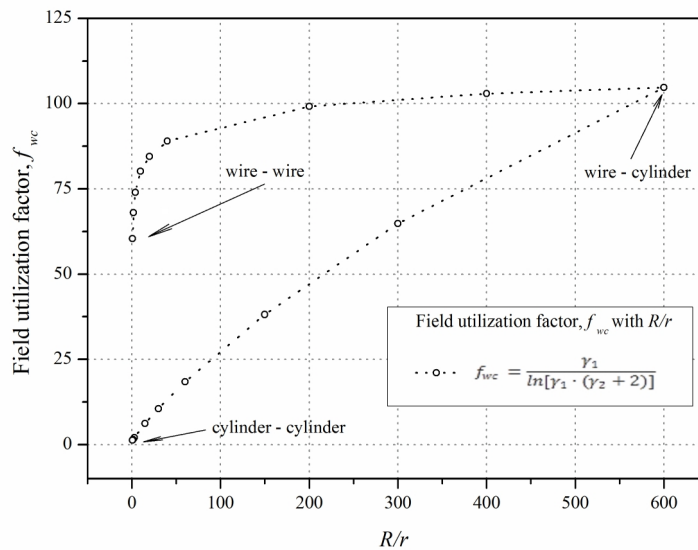
Figure 4-12 Field utilization factor f_{wc} with R/r ratio for electrode gap d=3cm.

The maximum value of f_{wc} has been found in the case of the maximum field inhomogeneity (f_{wc} =104 for R/r=600) and was high enough considering other geometries [92].

4.2 FIELD LINE LENGTHS

A typical FEA image of the field lines in a wire-cylinder setup is shown in figure 4-13, where it becomes clear that the electric field lines are in fact segments of circles with different radii. This has been verified by the extracted particle trajectory data (the coordinates of successive points along each field line) from FEA simulations. It may be noted that the distribution of field lines in the wire-cylinder setup resembles the well-known distribution of field lines in two parallel cylindrical conductors [92].
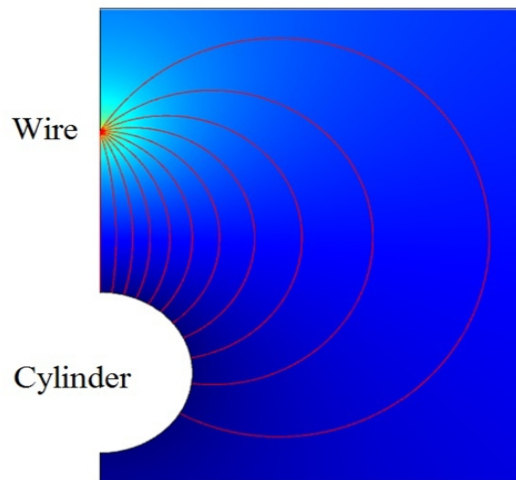
Figure 4-13 Typical distribution of the electric field lines. FEA results for *r* =50μm, *d*=3cm and *R*=15mm.

Figure 4-14 displays a more detailed geometrical model for an electric field line emerging from the wire emitter (point *O*) and ending perpendicularly on the cylinder's surface (point *O´*). As shown in figure 4-14, each field line is characterized by its emerge angle θ or, equivalently, from its incidence angle φ, with reference to the gap axis *Y*. The incident angle has been selected as identification parameter of the field lines.

The total lengths L_{fl} φ of different field lines have been recorded as a function of their angles of incidence φ on the cylinder's surface. A great number of simulations have been made, covering incidence angles between 0 and 180°, in order to cover the right half part of the cylinder's surface. Given the symmetry around the *Y* axis, the other half part on the left side of *Y* axis exhibits identical behavior.
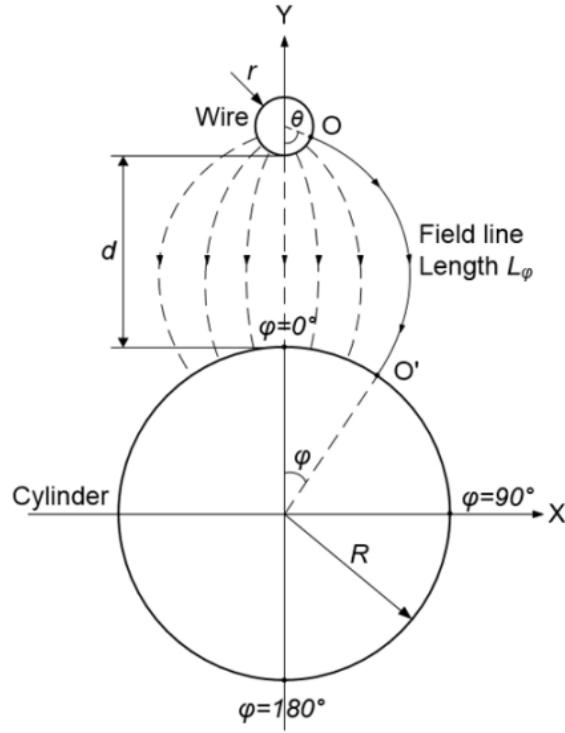
Figure 4-14 Schematic representation of the field line parameters for FEA simulations.

The total length $L_{fl}\,\varphi$ of each field line, for a given incidence angle φ, can be calculated by extracting the corresponding particle trajectory data from the simulation software in the form of a series of pairs of Cartesian coordinates $(x_{\varphi,i},\ y_{\varphi,i})$, each corresponding to a single point on this line. The infinitesimal displacement $\varDelta L_{fl}\,\varphi,i$ between successive points is:

$$\varDelta L_{fl\varphi,i} = \sqrt{\left(x_{\varphi,i} - x_{\varphi,i-1}\right)^{2} + \left(y_{\varphi,i} - y_{\varphi,i-1}\right)^{2}} \tag{4.5}$$

The sum of all $\varDelta L_{fl\,\varphi,i}$ displacements equals the total trajectory length $L_{fl\,\varphi}$:

$$L_{fl\varphi} = \sum_{i} \varDelta L_{fl\varphi,i} \tag{4.6}$$

The numerical results for trajectory lengths $L_{fl}\,\varphi$ have been used in order to determine a symbolic expression for the electric field lines. The following formula provides a very good approximation for the total length of field lines:

$$L_{Fl}(\varphi) = d \cdot cosh^a(\varphi) \tag{4.7}$$

where a is a dimensionless parameter coming from $L_{fl}\,\varphi$ data fitting. The resulting values of a, for the wire-cylinder electrode setup, are given in table 4-1.

Table 4-1 Fitted values of parameter a, according to equation (4.7), from FEA results for the total trajectory lengths $L_{fl}\,\varphi$.

Electrode configurations	Varying geometrical parameter		a
1st set (r = 50µm and R = 15mm)	d (cm)	1	1.96
		2	1.45
		3	1.23
		4	1.06
		5	0.98
2nd set (d = 3 cm and R = 15 mm)	r (µm)	50	1.23
		100	1.24
		250	1.25
3rd set (r = 50 µm and d = 3 cm)	R (mm)	5	0.85
		10	1.05
		15	1.23

Figure 4-15 shows the electric field line lengths for varying electrode gap length d, wire radius r and cylinder radius R respectively, as well as the fitted curves according to equation (4.7) for the parameter a values shown in table 4-1.
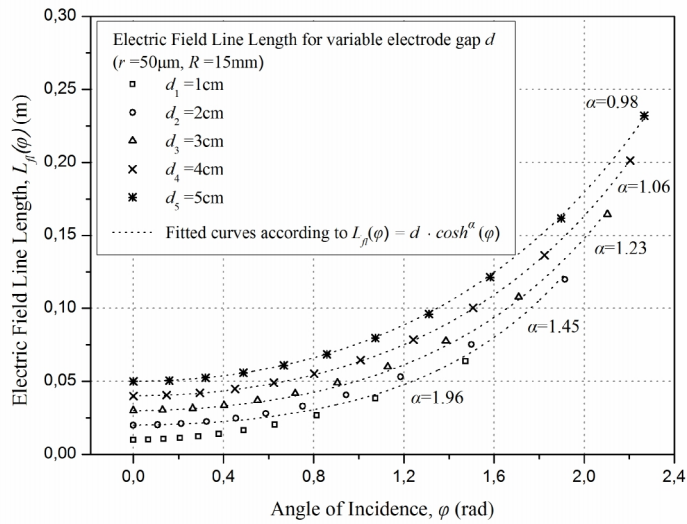
(a)
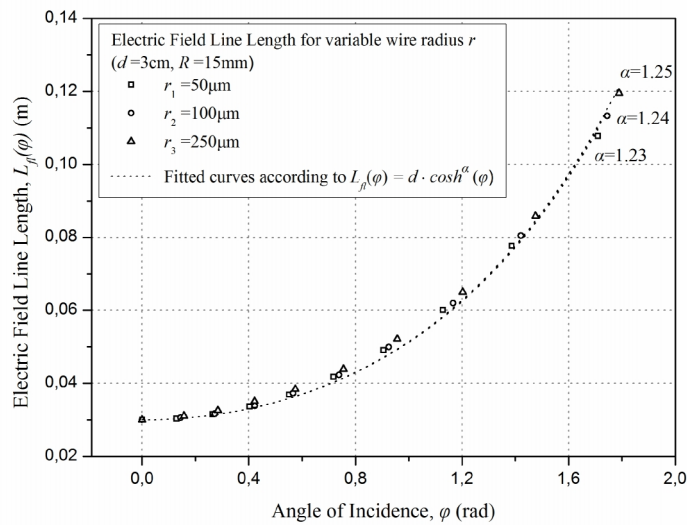
(b)
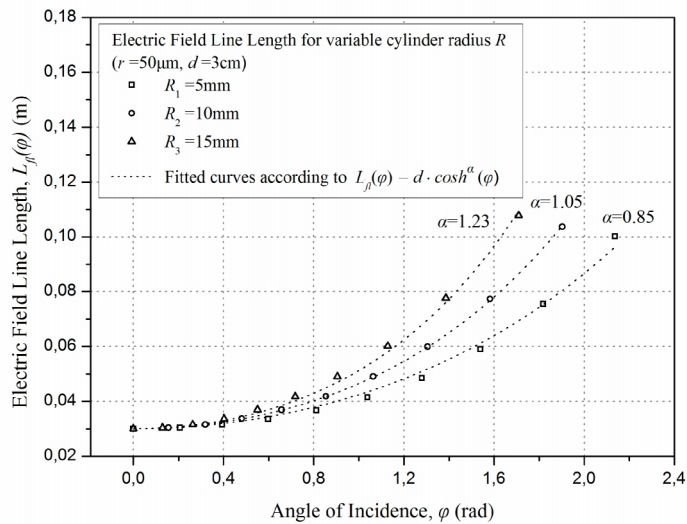
(c)

Figure 4-15 Electric field line length $L_{fl}\,\varphi$ with angle of incidence φ (FEA simulations) for (a) variable electrode gap (d=1-5cm, r=50μm and R=15mm), (b) variable wire radius (r=50-250μm, d=3 cm, and R=15mm) and (c) variable cylinder radius (R=5-15mm, r=50μm and d=3cm). In (b) the fitted curves for different a values coincide.

Further analysis of the data in table 4-1 has shown that the dimensionless parameter α can be expressed as a function of the geometrical characteristics of the electrodes:

$$a = \left(\frac{r}{d}\right)^{0.083} + \left(\frac{R}{d}\right)^{0.7} \tag{4.8}$$

4.3 SATURATION CURRENT DENSITY LIMIT

Regarding the general expression for the saturation current density limit given in equation (2.21) and FEA results for the total length of electric field lines according to equation (4.7), we get that the distribution of the saturation current density limit $j_s(\varphi)$ over the cylinder's surface is not uniform and can be approximated by the formula:

$$j_s(\varphi) = \mu \cdot \varepsilon_o \cdot \frac{V^2}{L_{fl}(\varphi)^3} = \mu \cdot \varepsilon_o \cdot \frac{V^2}{\left(d \cdot cosh^a(\varphi)\right)^3} = \frac{\mu \cdot \varepsilon_o \cdot V^2}{d^3} \cdot cosh^{-3a}(\varphi) \tag{4.9}$$

where $j_s(\varphi)$ is the saturation current density limit (A/m^2) and φ is the incidence angle according to figure 4-14 with $0 \le \varphi \le \pi$ and a is given by equation (4.8).

It becomes clear from equation (4.9) that the maximum current density j_{s0} is obtained at $\varphi=0$, where $L_{fl}(0)=d$:

$$j_{s0} = j_s(0) = \mu \cdot \varepsilon_o \cdot \frac{V^2}{L_{fl}(0)^3} = \frac{\mu \cdot \varepsilon_o \cdot V^2}{d^3} \tag{4.10}$$

Equation (4.9) can then be rewritten as:

$$j_s(\varphi) = j_{s0} \cdot cosh^{-3a}(\varphi) = j_{s0} \cdot cosh^{-k_s}(\varphi) \tag{4.11}$$

where $k_s = 3a = f (r/d, R/d)$ is dimensionless.

The FEA simulation results for the normalized current density $j_s(\varphi)/j_{s0}$ for different d, r and R values is given in figure 4-16.
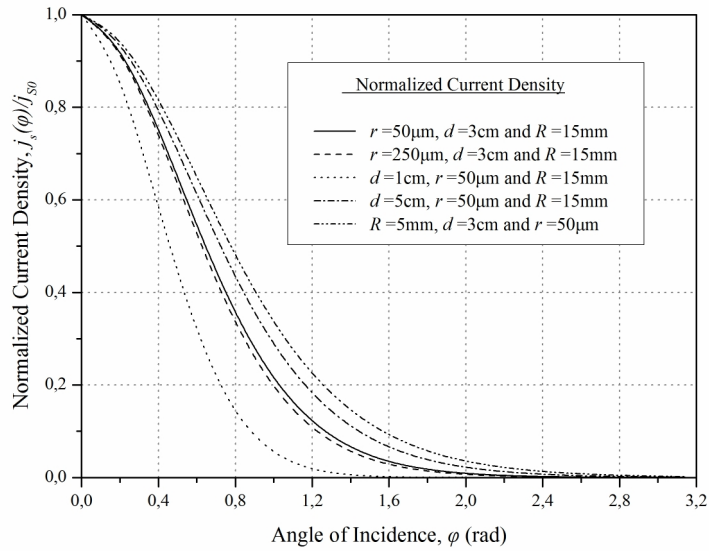
Figure 4-16 Normalized current density $j_s(\varphi)/j_{s0}$ with the angle of incidence φ for varying electrode gap d, wire radius r and cylinder radius R.

It becomes clear that current density $j_s(\varphi)$ is decreasing abruptly at larger φ angles, laterally on the cylinder's surface (see figure 4-14). This happens due to the dependence of $j_s(\varphi)$ on $L_{fl}(\varphi)^{-3}$, in combination with the fact that the length of the field lines $L_{fl}(\varphi)$ is considerably increasing at larger φ angles, according to figure 4-15. The contribution of large incidence angles φ, over 1.6 rads ($\approx$90°), to the current density is generally minimal, due to the 'expansion' of the field lines.

It should be noted that the current density distributions of figure 4-16 resemble the well-known Warburg distribution [117, 118], which has also been observed in other geometries as well [14, 133-135]. For example, in stationery point-to-plane geometry [14] the current density over the plane decreases with $cos^m(\theta)$ for $\theta \leq 60°$, where θ denotes the angle of the field lines emerging from the tip. This kind of dependence, though different from the $cosh^{-ks}(\varphi)$ rule, results in a similar variation.

It also appears that the current density distribution is mainly determined by the gap distance d and, secondly, on the cylinder's radius R. On the other hand, it has almost no dependence on the wire radius r. This is normal, because the variation of the wire radius r within the limits of this study (50 to 250µm) represents only a small fraction of the total length L_{fl} (φ) of the electric field lines in equation (4.9). Therefore, it has a minimal effect on the corresponding current density. For example, the minimum field line length equals the gap distance d and is calculated at incidence angle $\varphi=0$. For $d=3$cm, r represents only a small fraction ranging between 0.16% and 0.83% of the shortest field line.

4.4 UNIPOLAR SATURATION CURRENT LIMIT

Figure 4-17 displays the contribution of the saturation current density $j_s(\varphi)$ to the saturation current di_s along a $Rd\varphi$ wide thin strip on the cylinder's surface, per unit length of the electrodes.
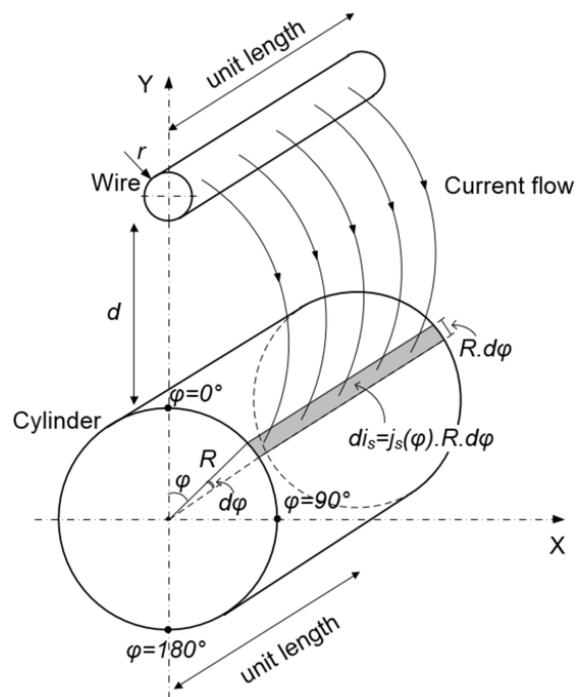
Figure 4-17 Contribution of the saturation current density $j_s(\varphi)$ to the saturation current di_s along a $Rd\varphi$ wide thin strip on the cylinder's surface, per unit length of the electrodes.

According to figure 4-17, the elementary contribution di_s of $j_s(\varphi)$ to the total saturation current limit may be defined considering the elementary area $Rd\varphi$ corresponding to a thin strip of unit length along the cylinder's surface, at angle φ. The saturation unipolar current $i_s(\varphi)$ per unit length of the wire-cylinder electrodes can then be estimated by integrating di_s over the cylinder's surface, from the cylinder's top ($\varphi=0$) up to angle φ. Substituting from equations (4.10) and (4.11) we get:

$$i_s(\varphi) = 2\int_0^\varphi di_s \cdot d\varphi = 2\int_0^\varphi j_s(\varphi) \cdot R \cdot d\varphi = 2\int_0^\varphi j_{so} \cdot \cosh^{-k_s}(\varphi) \cdot R \cdot d\varphi =$$

$$= j_{so} \cdot 2 \cdot R \int_0^\varphi \cosh^{-k_s}(\varphi) \cdot d\varphi$$

(4.12)

where $0 \le \varphi \le \pi$. Multiplication by 2 in equation (4.12) is introduced in order to count for the other half part of the cylinder's surface, on the left side of Y axis.

The total current limit I_s per unit length of the electrodes can be estimated considering the whole surface of the cylinder for $\varphi=\pi$:

$$I_S = j_{so} \cdot 2 \cdot R \int_0^\pi \cosh^{-k_s}(\varphi) \cdot d\varphi \tag{4.13}$$

$$k_s = 3 \cdot a = 3 \cdot \left[\left(\frac{r}{d}\right)^{0.083} + \left(\frac{R}{d}\right)^{0.7}\right] \tag{4.14}$$

The unipolar saturation current limit I_s (A/m) represents the maximum current between the electrodes, assuming unipolar current flow. This model is valid during normal corona flow, at voltage levels below the breakdown voltage of the gap. Table 4-2 summarizes the results for I_s at different k_s values, according to equation (4.13) and table 4-1.

Table 4-2 Unipolar saturation current limit I_s in a wire-cylinder arrangement per unit length of the electrodes, versus maximum current density j_{s0}, for different geometrical characteristics of the electrodes according to equation (4.13).

Experimental set	Varying parameter		$k_s = 3a$ (table 4.1)	k_s according to (4.14)	I_s according to (4.13) (A/m·kV)
1st set r=50μm R=15mm	d (cm)	1	5.88	5.92	$j_{s0} \times 0.0161$
		2	4.35	4.28	$j_{s0} \times 0.0193$
		3	3.69	3.61	$j_{s0} \times 0.0212$
		4	3.18	3.23	$j_{s0} \times 0.0226$
		5	2.94	2.98	$j_{s0} \times 0.0236$
2nd set d=3cm R=15mm	r (μm)	50	3.69	3.61	$j_{s0} \times 0.0212$
		100	3.72	3.72	$j_{s0} \times 0.0208$
		250	3.75	3.86	$j_{s0} \times 0.0204$
3rd set r=50μm d=3cm	R (mm)	5	2.55	2.62	$j_{s0} \times 0.0085$
		10	3.15	3.15	$j_{s0} \times 0.0153$
		15	3.69	3.61	$j_{s0} \times 0.0212$

The normalized distribution of $i_s(\varphi)/I_s$ over the cylinder's surface is given in figure 4-18, for different r, d and R. Generally, it can be observed that the electric field lines that end on the cylinder's surface at incidence angles over 1.6 rads (~90°) have limited effect on the total saturation current ranging from 0% for d=1cm, r=50μm and R=15mm, to 4% for d=3cm, r=50μm and R=5mm. This is due to the current density distribution over the cylinder's surface which falls abruptly for $\varphi \geq 90°$ (see figure 4-16).
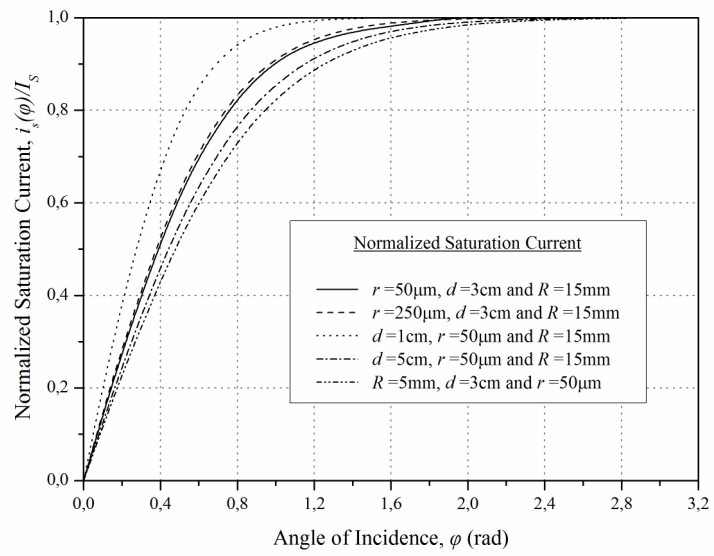
Figure 4-18 Normalized distribution of the saturation current $i_s(\varphi)/I_s$ to the angular displacement φ over the cylinder's surface, per unit electrode length.

CHAPTER 5 - EXPERIMENTAL RESULTS AND DISCUSSION

5.1 CORONA DISCHARGE CURRENT

Experiments have been conducted in order to define which one of Townsend's formulae for the current-voltage characteristic (2.11 or 2.12) best fits the experimental current results for the wire-cylinder arrangement. In order to estimate coefficients A and k, as well as to define the magnitude of dependence on geometrical characteristics of the electrodes, a parametric analysis has been carried out. It should be noted, that all measurements were conducted by increasing the applied voltage just below the breakdown voltage of the gap.

As mentioned in Chapter 3, all measurements of the positive corona discharge current have been taken by applying high dc voltage to the emitter with 1kV increments. On the other hand, the applied voltage increments for the determination of the *Corona Inception Voltage* had been significantly lower (50V), in order to ensure the required sensitivity of the measurement.
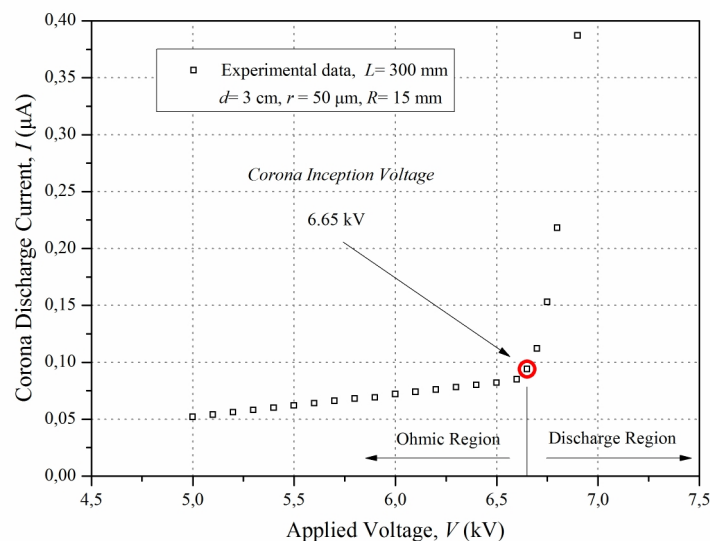
Figure 5-1 Experimental results of the corona current as a function of the applied voltage for *L*=300cm, *d*=3cm, *r*=50μm and *R*=15mm. The corona inception threshold (CIV) is clearly shown at 6.65kV.

Figure 5-1 is an indicative representation of the experimentally detected CIV in the case of a typical wire-cylinder electrode arrangement, where the electrode length was $L=300$mm, the electrode gap was $d=3$cm and the wire and cylinder radii were $r=50\mu$m and $R=15$mm, respectively. According to figure 5-1, the air surrounding the electrodes exhibits an Ohmic behaviour in the voltage region below the CIV of 6.65kV, where the electric field is relatively small. This may be considered as the '*Ohmic Region*' where the current density can be expressed as:

$$j = \sigma \cdot E_{av} \tag{5.1}$$

where σ is the conductivity of the medium ($3\text{-}8\cdot10^{-15}$ S/m for air at 20 ˚C [8]).

When the applied voltage is further increased, above 6.65kV in this case, corona discharges initiate and the *V/I* characteristic deviates significantly from the constant-slope Ohmic linear model, to a quadratic relationship approximated by (2.11) or (2.12) indicating the '*Discharge Region*'.

Influence of the electrode length L on the corona current

Measurements of the positive corona discharge current were made on five modules with electrode length $L_1=100$mm, $L_2=200$mm, $L_3=300$mm, $L_4=400$mm and $L_5=500$mm. The emitter radius r, the collector radius R and the electrode gap d were kept constant at 50μm, 15mm and 3cm respectively. Experimental results of the corona discharge current with applied voltage are presented in figure 5-2.

Coefficients A and k were estimated by a least square fitting method according to (2.11) and (2.12) (see table 5-1), where V_0 was the detected corona inception voltage in each case.
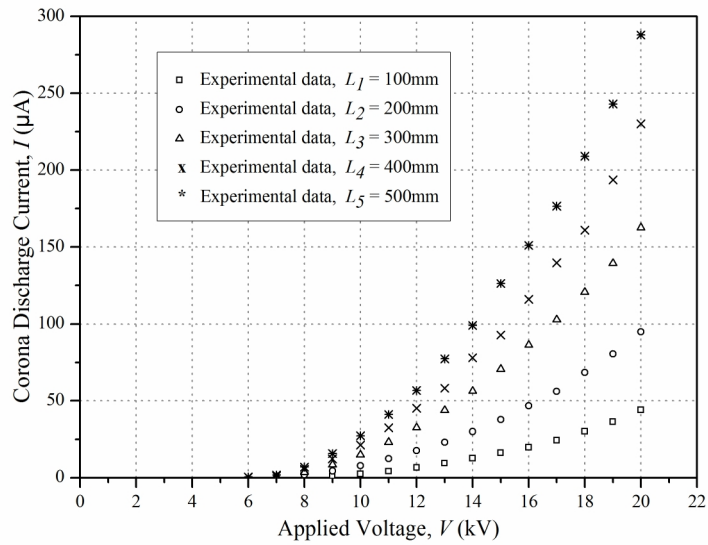
(a)
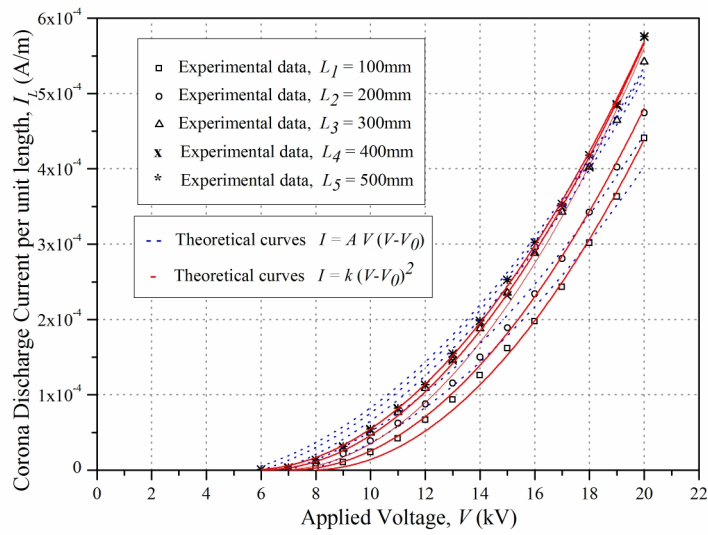
(b)

Figure 5-2 (a) Corona discharge current with the applied voltage and (b) corona current per unit electrode length (A/m) with the applied voltage for different electrode lengths L. Experimental results and fitted curves according to Townsend's formulae for d=3cm, r=50μm and R=15mm.

Table 5-1 Coefficients *A, k* and inception voltage V_0 values, as a function of the electrode length *L*, for *d*=3cm, *r*=50μm and *R*=15mm.

Electrode length *L* (mm)	Inception Voltage V_0 (kV)	Coefficient *A* (A/m·V^2)	Coefficient *k* (A/m·V^2)
L_1 = 100	7.8	$1.65 \cdot 10^{-12}$	$2.84 \cdot 10^{-12}$
L_2 = 200	7.1	$1.71 \cdot 10^{-12}$	$2.95 \cdot 10^{-12}$
L_3 = 300	6.65	$1.95 \cdot 10^{-12}$	$3.14 \cdot 10^{-12}$
L_4 = 400	6	$1.96 \cdot 10^{-12}$	$3.16 \cdot 10^{-12}$
L_5 = 500	5.7	$1.98 \cdot 10^{-12}$	$3.18 \cdot 10^{-12}$

The positive corona discharge current was found to be proportional to the electrode length *L,* as expected, since the generated corona current is controlled by the emitter length. Contrary to the expectation that the current per unit length should stay constant, it seems to be affected by the electrode length, especially for small values of *L*. This may be attributed to the electric field deformation at the wire and cylinder edges, which is becoming less significant as the length increases. This comes also in agreement with the variation of the experimental corona inception voltage results for shorter lengths (see table 5-1). As shown in figure 5-2b, the discharge current per unit electrode length becomes nearly constant above *L*=300mm. Thus, the electrode length of 300mm has been considered adequate for further analysis regarding the investigation of other geometrical parameters (*d, r* and *R*). So, all the wire-cylinder electrode assemblies that have been used in the remaining experiments have constant length *L*=300mm.

Influence of the electrode gap d on the corona current

The relationship between the positive corona discharge current and the electrode gap *d* has also been investigated. Measurements of the discharge current were made on five modules with electrode gaps d_1=1cm, d_2=2cm, d_3=3cm, d_4=4cm and d_5=5cm, while the emitter and the collector radii, were constant at *r*=30μm and *R*=15mm respectively. The electrode length was *L*=300mm in all cases. A comparison, of the discharge current per unit electrode length with respect to the applied voltage for different gaps, is

presented in figure 5-3.

Figure 5-3 Corona discharge current per unit electrode length (A/m) with applied voltage, for different electrode gaps d. Experimental results and fitted curves according to Townsend's formulae for L=300mm, r=30μm and R=15mm.

As shown in figure 5-3, we have fitted our experimental data to the models given by (2.11) and (2.12), using the experimental results for the corona inception voltage V_0. In this way, coefficients A and k have been defined accordingly (see table 5-2).

Table 5-2 Coefficients A, k and inception voltage V_0 values, as a function of the electrode gap d, for L=300mm, r=30μm and R=15mm.

Electrode gap d (cm)	Inception Voltage V_0 (kV)	Coefficient A ($A/m \cdot V^2$)	Coefficient k ($A/m \cdot V^2$)
$d_1 = 1$	4.45	$24.8 \cdot 10^{-12}$	$57.6 \cdot 10^{-12}$
$d_2 = 2$	5.15	$5.25 \cdot 10^{-12}$	$8.67 \cdot 10^{-12}$
$d_3 = 3$	5.7	$1.97 \cdot 10^{-12}$	$2.82 \cdot 10^{-12}$
$d_4 = 4$	6.1	$1.05 \cdot 10^{-12}$	$1.45 \cdot 10^{-12}$
$d_5 = 5$	6.4	$0.66 \cdot 10^{-12}$	$0.88 \cdot 10^{-12}$

Increasing the electrode gap, while keeping the applied voltage constant, resulted in a decreased discharge current. As shown in figure 5-3, the dependence on the gap decreases with larger gaps. Small gaps produce higher electric field gradients at the conductor's surface (see Chapter 4), which in turn, reduces the breakdown voltage of the gap (e.g. for d_1=1cm the breakdown voltage was below 9kV, while for d_5=5cm, the breakdown voltage was above 30kV). The relationship between the electric field intensity and the electrode separation distance d is inversely proportional (equation 2.6), thus larger gaps produce reduced currents with respect to the applied voltage. Coefficients A and k decrease with the gap but, in contrast, the inception voltage increases with the gap, as expected according to equation (2.9).

Influence of the emitter radius r on the corona current

Measurements of the discharge current have been made on five electrode assemblies with r_1=30μm, r_2=50μm, r_3=100μm, r_4=250μm and r_5=400μm. The remaining geometrical parameters where constant at L=300mm, d=3cm and R=20mm respectively. The experimental results of the discharge current per unit electrode length with applied voltage, with varying emitter radius r, are shown in figure 5-4 with the corresponding fitted curves according to equations (2.11) and (2.12).
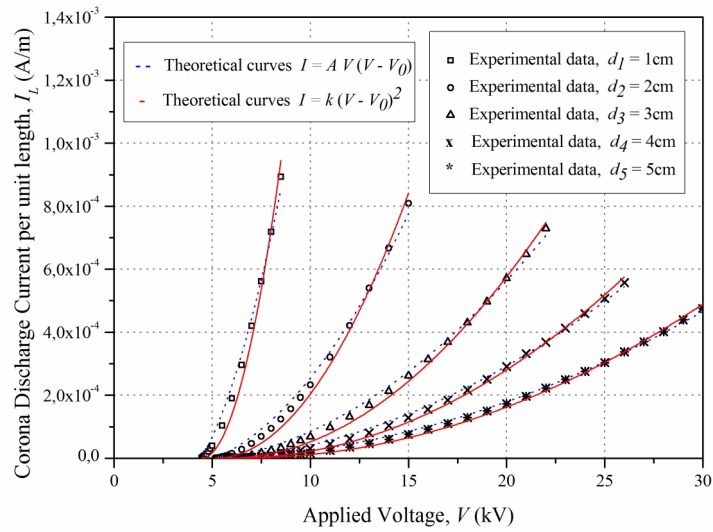

Figure 5-4 Corona discharge current per unit electrode length (A/m) with applied voltage for different wire radii r. Experimental results and fitted curves according to Townsend's formulae for L=300mm, d=3cm and R=20mm.

Coefficients A and k, which are presented in table 5-3, were estimated accordingly considering the experimental results for the corona inception voltage V_0.

Table 5-3 Coefficients A, k and inception voltage V_0 values, as a function of the wire radius r, for L=300mm, d=3cm and R=20mm.

Emitter radius r (μm)	Inception Voltage V_0 (kV)	Coefficient A (A/m·V^2)	Coefficient k (A/m·V^2)
$r_1 = 30$	5.4	$1.87 \cdot 10^{-12}$	$3.06 \cdot 10^{-12}$
$r_2 = 50$	6.55	$2.13 \cdot 10^{-12}$	$3.48 \cdot 10^{-12}$
$r_3 = 100$	8.6	$2.26 \cdot 10^{-12}$	$3.92 \cdot 10^{-12}$
$r_4 = 250$	13.45	$2.32 \cdot 10^{-12}$	$5.87 \cdot 10^{-12}$
$r_5 = 400$	17.7	$2.49 \cdot 10^{-12}$	$8.97 \cdot 10^{-12}$

According to the experimental findings, the corona discharge current is decreasing as the wire radius is getting larger, although the ionization region a, expands according to equation (2.8). A possible explanation may be that the electric field intensity at the conductor's surface decreases as the wire radius is getting larger (see Chapter 4) and the mean field intensity across the gap may decrease as well. Thus, the electric carriers (*positive ions*) that have been produced in the ionization region, drift across the gap with reduced velocity as the electric field forces are getting weaker. The effect of the electric field intensity on the average ion drift velocity across the gap can easily be seen from equation (2.18).

According to the above, increased wire radius results in decreased mean electric field intensity between the electrodes, which in turn results in lower ion drift velocities across the gap. Hence, the positive ions that reach the cathode per unit time reduce, thus declining the total corona discharge current. Coefficients A and k increase proportionally to the wire radius although the discharge current decreases with r. Similarly, the corona inception voltage V_0 increases with the emitter radius r (see table 5), as expected according to equation (2.9).

Influence of the collector radius R on the corona current

In order to define the dependence of the discharge current on the cylinder radius R, measurements of the positive corona discharge current have been carried out on different electrode modules with cylinder radii $R_1=5mm$, $R_2=10mm$, $R_3=15mm$ and $R_4=20mm$. The electrode length was constant at $L=300mm$, while the emitter radius r and the electrode gap d were 100μm and 5cm respectively.

The experimental results of the positive corona discharge current per unit electrode length with the applied voltage, for varying cylinder radius R, are presented in figure 5-5, with the corresponding fitted curves according to Townsend's equations (2.11) and (2.12).
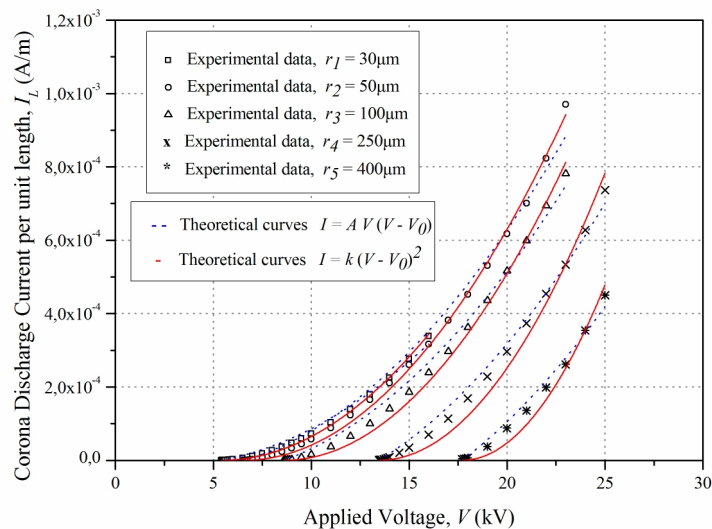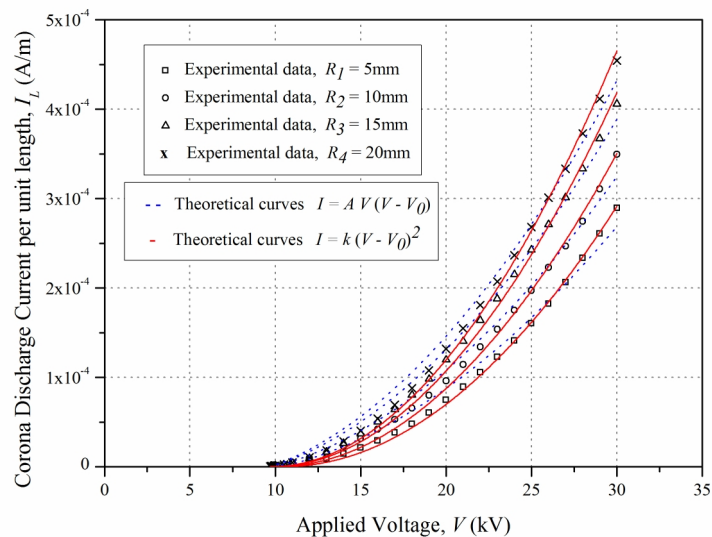

Figure 5-5 Corona discharge current per unit electrode length (A/m) with applied voltage for different cylinder radii R. Experimental data and fitted curves according to Townsend's formulae for $L=300mm$, $d=5cm$ and $r=100μm$.

The estimated values of coefficients A and k as well as the corona inception voltage V_0 values are given in table 5-4.

Table 5-4 Coefficients *A, k* and inception voltage V_0 values, as a function of the cylinder radius *R*, for *L*=300mm, *d*=5cm and *r*=100μm.

Collector radius R (mm)	Inception Voltage Vo (kV)	Coefficient A (A/m·V^2)	Coefficient k (A/m·V^2)
$R_1 = 5$	10.4	$4.57 \cdot 10^{-12}$	$0.76 \cdot 10^{-12}$
$R_2 = 10$	10	$5.41 \cdot 10^{-12}$	$0.88 \cdot 10^{-12}$
$R_3 = 15$	9.75	$6.39 \cdot 10^{-12}$	$1.02 \cdot 10^{-12}$
$R_4 = 20$	9.7	$7.09 \cdot 10^{-12}$	$1.13 \cdot 10^{-12}$

The positive corona discharge current seems to increase with the cylinder radius *R*. This is expected since increased collector (*cylinder*) radius produces higher electric field intensity at the emitter's surface due to the increased field inhomogeneity (see Chapter 4). In this way, the ionized particles start their drift with increased velocity according to equation (2.18). The positive ions arriving at the collector per unit time increase with *R*, thus providing higher discharge currents. Coefficients *A* and *k* also increase with *R*, as shown in table 5-4, while the inception voltage V_0 decreases with the cylinder radius.

Proposed formula for coefficient k

Coefficients *A* and *k* were estimated by a least square fitting method according to Townsend's formulae (2.11) and (2.12) and the fit was satisfactory in all cases. This verifies the assumption that the positive corona discharge current is proportional to the square of the applied voltage, thus showing that the Townsend formulae may also be applied in the case of wire-cylinder electrode geometry.

According to the investigation, equation (2.12) fits better than (2.11) in all cases (R^2~1). Coefficient *k* found to be proportional to the emitter and collector electrode radii (*r* and *R*) and inversely proportional to the electrode gap *d*. Further analysis of the experimental results has shown that coefficient *k* may be approximated according to the following expression:

$$k_{wc} = \frac{\mu \cdot \varepsilon_0}{d^2 \cdot \ln\left(\frac{d^2}{R \cdot r}\right)} \cdot \left[\frac{1395}{\left(\frac{d^2}{R \cdot r}\right)} + 11.18\right] \qquad (5.2)$$

The correlation between experimental data and theoretical curves for the corona discharge current according to equation (2.12), where coefficient k_{wc} has been applied, is shown in figure 5-6. On the other hand, the error between experimental and theoretical data is shown in figure 5-7.
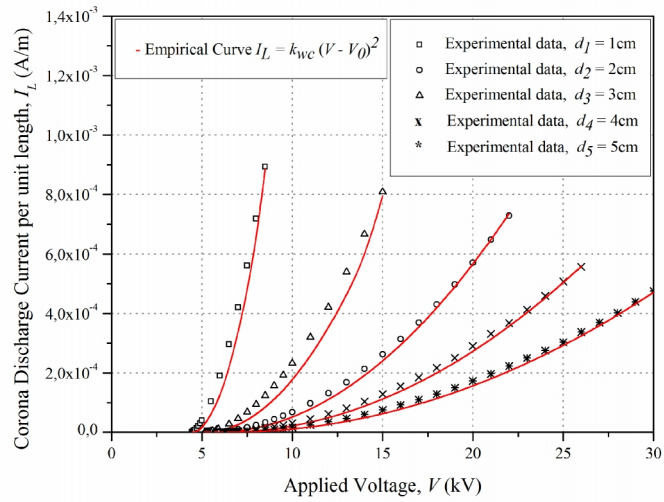
(a)
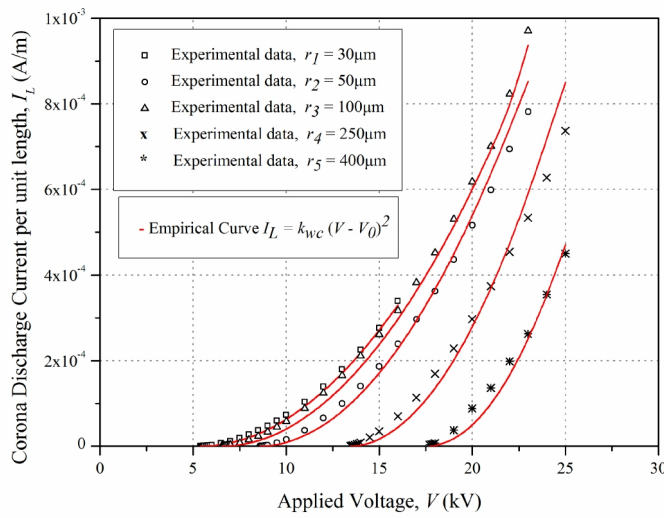
(b)
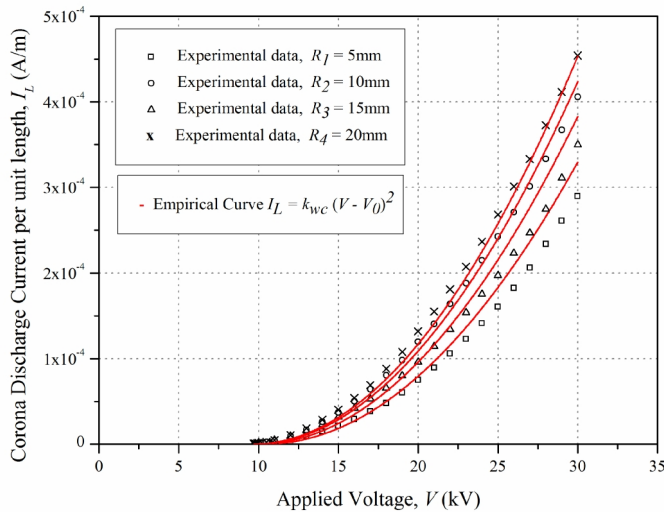
(c)

Figure 5-6 Corona discharge current per unit electrode length (A/m) with applied voltage. Correlation between experimental data and theoretical curves based on (2.12), where the proposed coefficient k_{wc} according to (4.16) has been used. (a) The electrode gap d varies between 1-5cm, (b) the wire radius r varies between 30-400μm and (c) the cylinder radius R varies between 5-20mm.
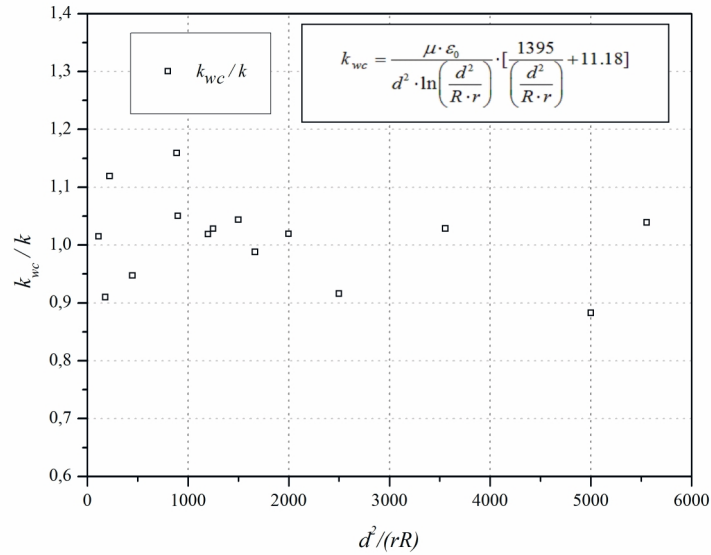
Figure 5-7 Ratio of the proposed k_{wc} corona current coefficient to the experimentally defined coefficient k according to equation (2.12), as a function of the dimensionless quantity (d^2/rR).

Corona Inception Voltage

The experimentally detected corona inception voltage V_0 results have been verified with FEA simulation results, along with the empirical values derived according to Peek's formula (2.9).

As mentioned in Chapter 3.2, FEA Model - *FEMM Modelling Parameters*, the wire and cylinder outer surfaces were considered to be equipotentials with fixed voltages 1kV and 0V, respectively. According to equation (3.6), the electric field strength at akV equals a times the electric field at 1kV. Hence, the CIV may be determined by dividing the air's dielectric strength ($\sim 3 \cdot 10^6$ V/m [9]) with the electric field strength at the vicinity of the ionization region a:

$$CIV_{SIM} = \frac{(Dielectric\ Strength\ of\ the\ medium)}{E_a} \tag{5.3}$$

The detailed plot of the electric field distribution near the HV wire (see figure 4-3) shows the surrounding area of the ionization region a where E_a is pointed out.

Figures 5-8, 5-9 and 5-10, display the correlation between the experimentally detected CIV results, the FEA simulation results according to equation (5.3), along with the empirical values derived according to Peek's formula (2.9). Moreover, the dependence of the CIV on the electrode gap d, the wire radius r and the cylinder radius R is presented.
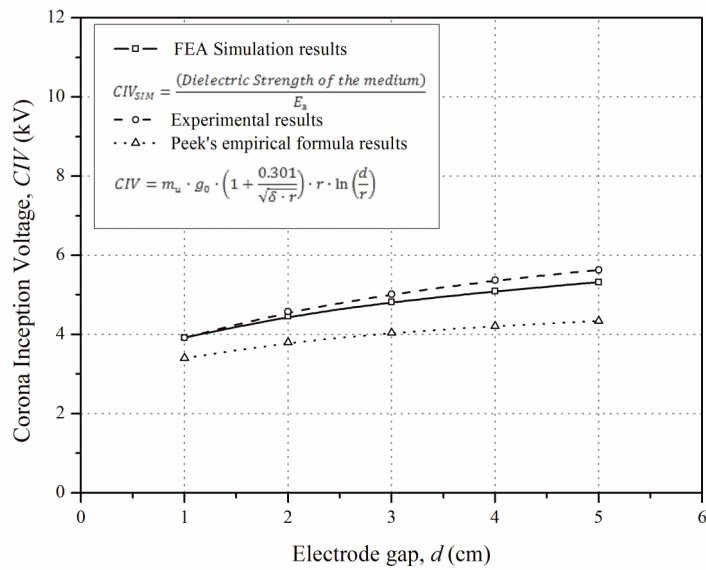
Figure 5-8 Dependence of the *CIV* on the electrode gap d, for r=50μm and R=15mm.
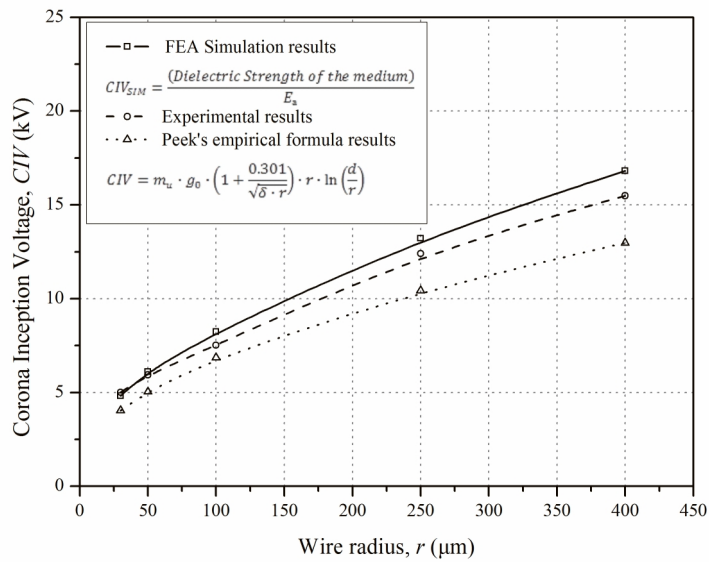
Figure 5-9 Dependence of the CIV on the wire radius *r*, for *d*=3cm and *R*=15mm.
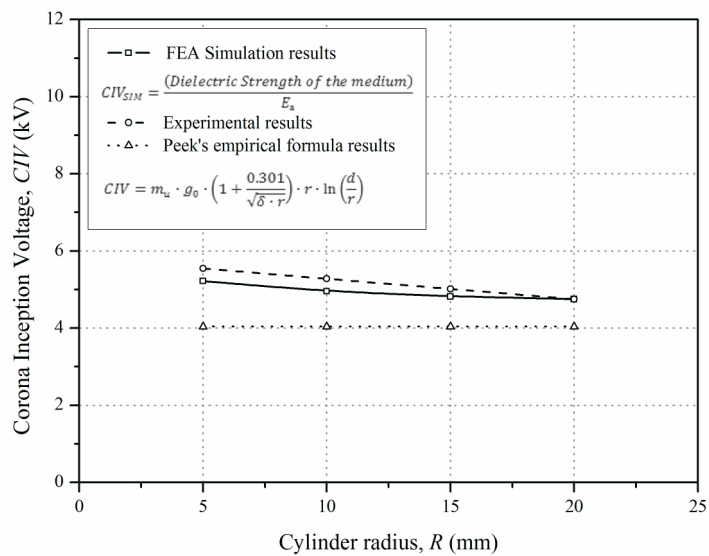
Figure 5-10 Dependence of the *CIV* on the cylinder radius *R*, for *d*=3cm and *r*=50μm.

The experimental results were in a good agreement with simulations data, thus confirming the accuracy of the applied method. On the other hand, Peek's empirical formula results according to equation (2.9) had slight divergence which may be attributed to the electric field which is less homogeneous in the wire-cylinder arrangement, compared to the parallel wire's geometry (see figure 5-11).
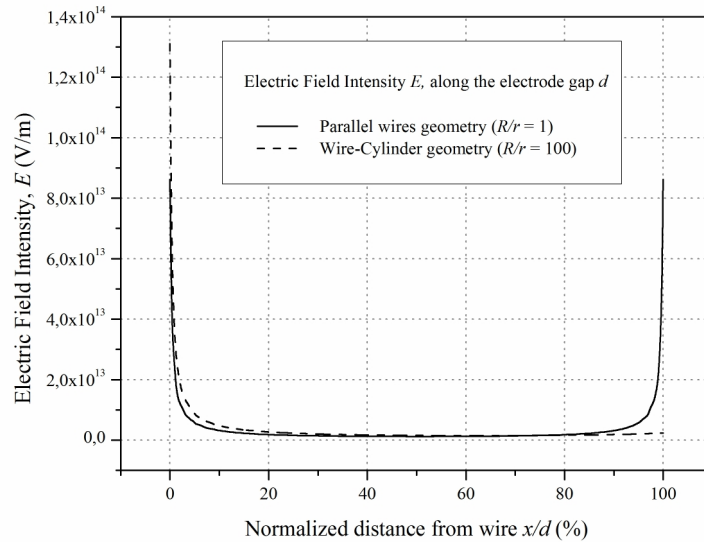
Figure 5-11 Electric field intensity along the electrode gap d for parallel wire geometry ($R/r=1$) and a typical wire-cylinder geometry ($R/r=100$).

The maximum electric field intensity of the air gap (at the conductor's surface) the exact moment when the corona discharges initiate E_{CIV}, has also been derived by Peek [9]:

$$E_{CIV} = m_u \cdot g_0 \cdot \left(1 + \frac{0.301}{\sqrt{\delta \cdot r}}\right) \tag{5.4}$$

In our case, the electric field strength that has been determined at the conductor's surface (at 1kV) multiplied by the CIV, provides the electric field intensity at the exact moment when the corona discharges initiate. A correlation between FEA simulation results for the electric field magnitude at the inception voltage E_{CIV} and Peek's empirical formula values according to equation (5.4) are presented in figures 5-12, 5-13and 5-14.
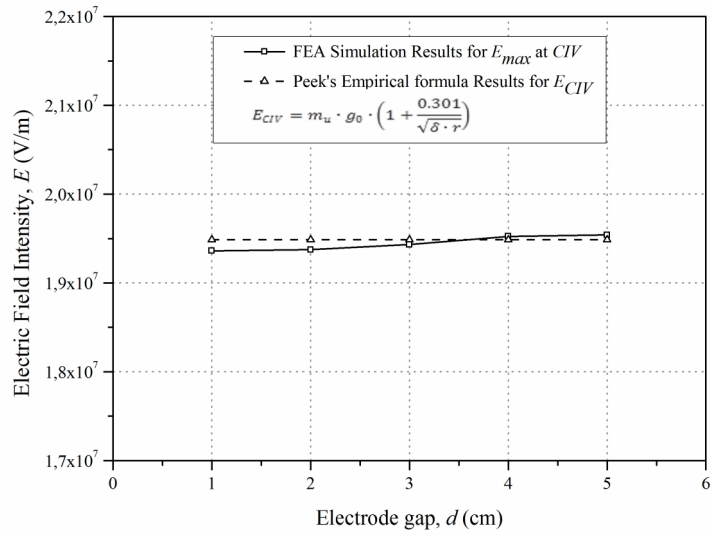
Figure 5-12 E_{CIV} with the electrode gap d, for r=30μm and R=15mm.
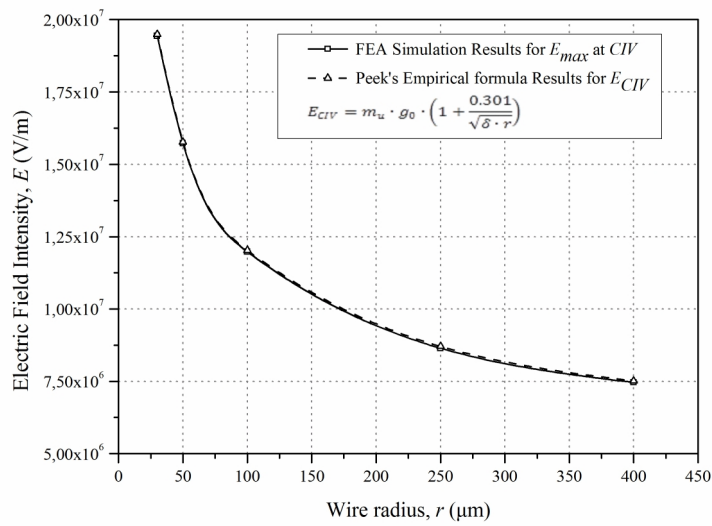
Figure 5-13 E_{CIV} with the wire radius r, for d=3cm and R=15mm.
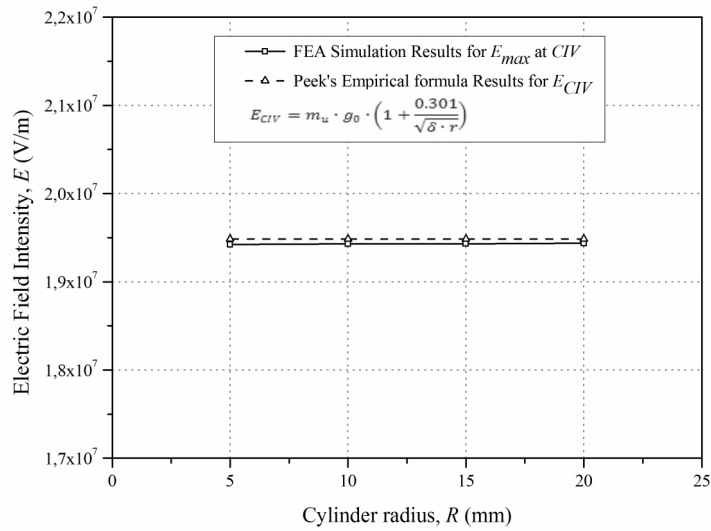
Figure 5-14 E_{CIV} with the cylinder radius R, for d=3cm and r=25μm.

It becomes clear, that the maximum electric field intensity, the exact moment when the corona discharges initiate E_{CIV}, depends only on the wire radius r. This comes also in agreement with Peek's empirical formula values according to equation (5.4), which coincide with the FEA simulation results in all cases.

5.2 SATURATION CURRENT

The experimental results for the corona discharge current from Chapter 5.1 have been used in order to relate the experimental outcomes to theoretical findings for the saturation current limit I_s according to equation (4.13).

Figures 5-15, 5-16 and 5-17, show the relation between the experimental measurements for the corona discharge current and the saturation current limit I_s, according to the proposed equation (4.13), at different voltage levels across the gap, below breakdown. As the exact value of the ion mobility μ in air depends on multiple factors and varies between 1.8 and 2.2 m^2/V·s [112-113], an average value of 2 m^2/V·s has been considered for the saturation current limits.
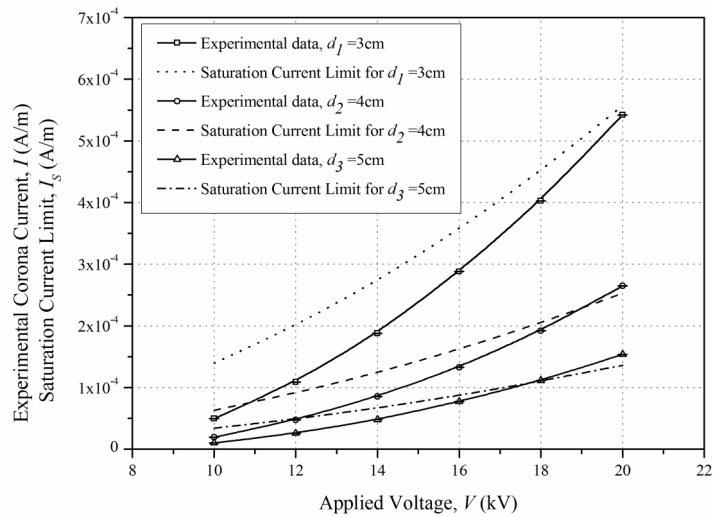
Figure 5-15 Correlation between the experimental data for corona current I and the theoretical saturation current limit I_s per unit length of the electrodes, for constant r=50μm, R=15 mm and electrode gaps d ranging from 3 to 5cm.
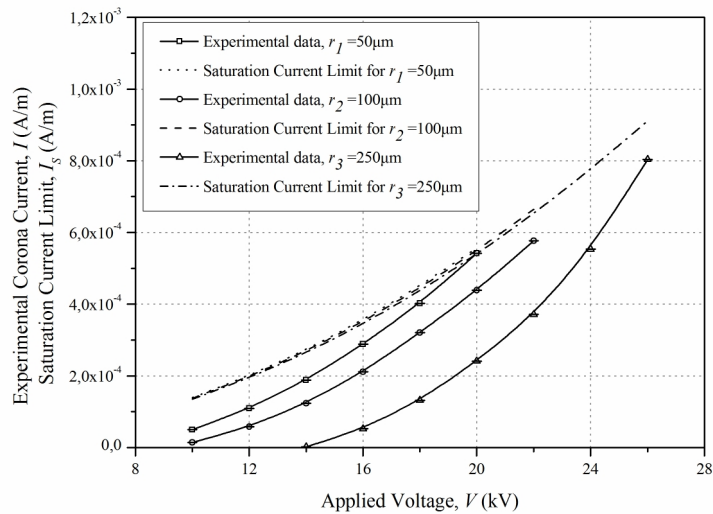
Figure 5-16 Correlation between the experimental data for corona current I and the theoretical saturation current limit I_s per unit length of the electrodes, for constant d=3cm, R=15 mm and wire radii r ranging from 50 to 250μm.
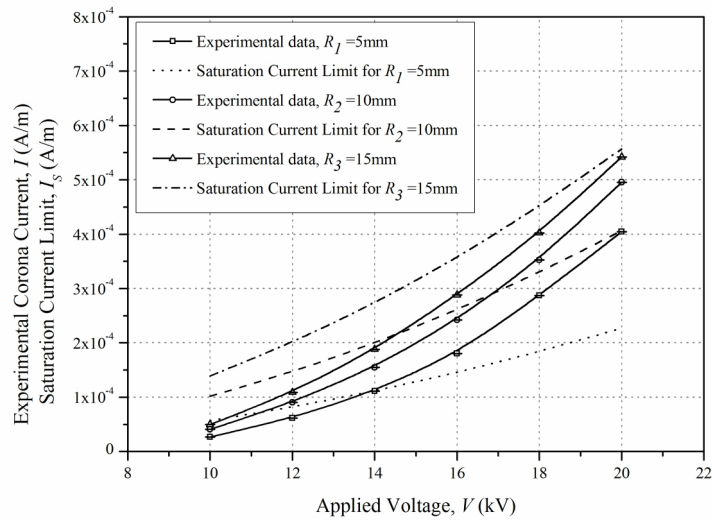
Figure 5-17 Correlation between the experimental data for corona current I and the theoretical saturation current limit I_s per unit length of the electrodes, for constant d=3cm, r=50μm and cylinder radii R ranging from 5 to 15mm.

A close relation between the experimental corona current values and the unipolar saturation current limits derived from equation (4.13) may be seen in figures 5-15, 5-16 and 5-17. Generally, the corona current seems to approach or exceed the saturation current limit at higher currents. These results are in agreement with other results, for different electrode geometries, which can be found in literature [14, 33,116, 136]. For example, in the case of corona between coaxial cylinders of radii r, R (for $r \ll R$), the relationship between the saturation current limit and the continuous corona current has been examined [14] and it has been found that the measured currents approach the saturation current limit at high currents. Similar results have been presented for positive point-to-plane or point-to-point gaps [136]. In these studies the increase of the corona current near or above the saturation limit is attributed to low pressure streamer generation at higher currents.

In fact, the field's gradient at the vicinity of the wire is controlling ionization, which produces the positive ions that contribute to the corona current between the electrodes [136]. On the other hand, the low-field strength outside the ionization area controls the movement of ions in the drift region. The drift region in many ways acts as large impedance in series with the ionization region and gives coronas their characteristic intrinsic stability [33]. In the case of wire-cylinder electrodes, the electric

field depends mainly on the gap d, the wire radius r and the R/r ratio (see Chapter 4). Generally, small gaps, thin wires and large cylinders produce stronger electric fields. Therefore, the increased corona currents with decreasing d of figure 5-15 are normally expected due to the higher electric fields that are generated along the gap at lower d values.

Since corona currents are strongly dependent on the electric field strength [8, 9, 14, 116], higher fields are generally expected to produce increased corona currents for a given geometry and corona polarity. The reduced corona currents, as the wire radius r increases in figure 5-16, may be attributed to the field reduction with thicker wires (see Chapter 4). Obviously, the saturation limits remain almost constant, due to the small dimensions of the wire's radius r in comparison with the gap d. It seems that these limits may be reached at higher voltage, before breakdown of the wire-cylinder gap.

Similarly, the increased corona currents at higher cylinder radii, as shown in figure 5-17, should also be expected due to the higher fields which are generated in the cases of high field inhomogeneity. The saturation limits vary in the same way, since higher cylinder radii have a strong influence on the distribution of the field lines in space. In this case, the experimental results show that the unipolar saturation current limits are more likely to be exceeded at lower voltage levels. According to bibliography, observed currents in excess of the unipolar saturation limits invariably imply either ions (*electrons*) of higher mobility than anticipated, or bipolar conduction phenomena like streamers [14, 33, 116]. It should be noted that bipolar conduction currents and unipolar currents may coexist in the total corona current flowing between the electrodes [14, 33, 116].

5.3 IONIC WIND VELOCITY

As far as the ionic wind velocity is concerned, parametric analysis has been carried out in order to define the dependence of the ionic wind velocity, the function of geometry k_G and the discharge cross section A_{cs} on geometrical characteristics of the electrodes. In all cases, equation (2.26) has been used in order to define the upper limit of the wind velocity, assuming single carrier conduction.

Influence of the electrode gap d on the wind velocity

The ionic wind velocity was plotted against $(I/\rho \cdot \mu)^{1/2}$ (see figure 5-18b) for d_1=2cm, d_2=3cm and d_3=4cm, while the emitter and collector radii were 50μm and 15mm respectively. The function of geometry k_G was derived from the experimental results by applying a least square fit (see figure 5-18b) according to equation (2.23), while the discharge cross section A_{cs} was derived by equation (2.25). All the results are given in table 5-5.
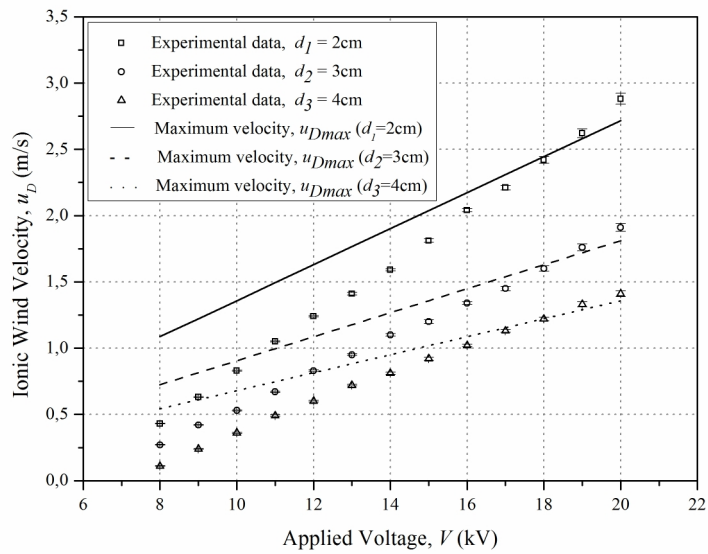
(a)
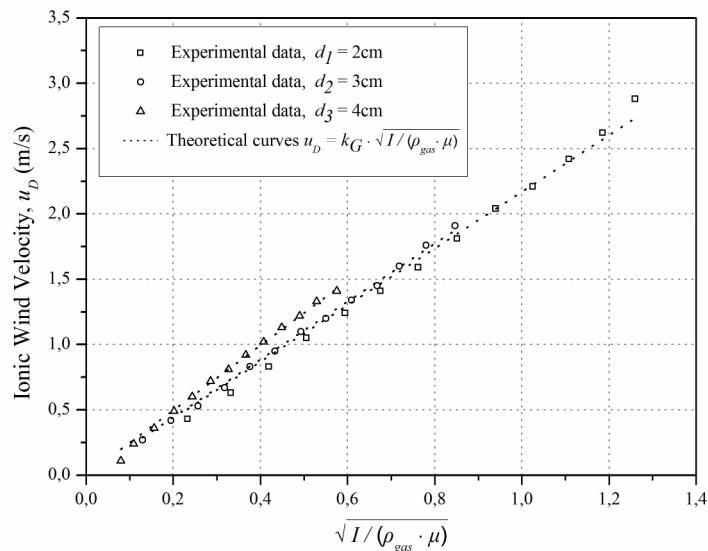
(b)

Figure 5-18 (a) Wind velocity with the applied voltage and (b) wind velocity with the $(I/\rho_{gas} \cdot \mu)^{1/2}$ (d_1=2cm, d_2=3cm and d_3=4cm, r=50μm and R=15mm).

Table 5-5 Function of geometry k_G and discharge cross section A_{cs} with the electrode gap d, for r=50µm and R=15mm.

Electrode gap d (cm)	Function of geometry k_G (m$^{-1/2}$)	Discharge cross section A_{cs} (m^2)
$d_1 = 2$	2.169	0.0043
$d_2 = 3$	2.215	0.0061
$d_3 = 4$	2.481	0.0065

As shown in figure 5-18a, the ionic wind velocity decreases with the gap distance, but on the other hand, the function of geometry and the discharge cross section increase with d. This is normal, since larger gaps produce more homogeneous electric fields and the field lines are getting wider. Thus, the discharge cross section A_{cs}, which depends on the area the field lines are shaping, increases with the gap as shown in table 5-5. In contrary, small gaps generate strongly inhomogeneous electric fields, which lead to bipolar conduction phenomena like streamers [14, 33, 116]. In this way, the ionic current which becomes bipolar, enhances the ionic wind velocity.

Influence of the emitter radius r on the wind velocity

The dependence of the ionic wind velocity on the emitter radius r was also investigated, with measurements of the wind velocity on three modules with r_1=50µm, r_2=100µm and r_3=250µm, while the electrode gap d and the collector radius R were 3cm and 15mm respectively. In this case also, fitting curves were drawn accordingly and the function of geometry k_G, so as the discharge cross section A_{CS}, was derived consequently. The results are given in figure 5-19 and table 5-6 respectively.
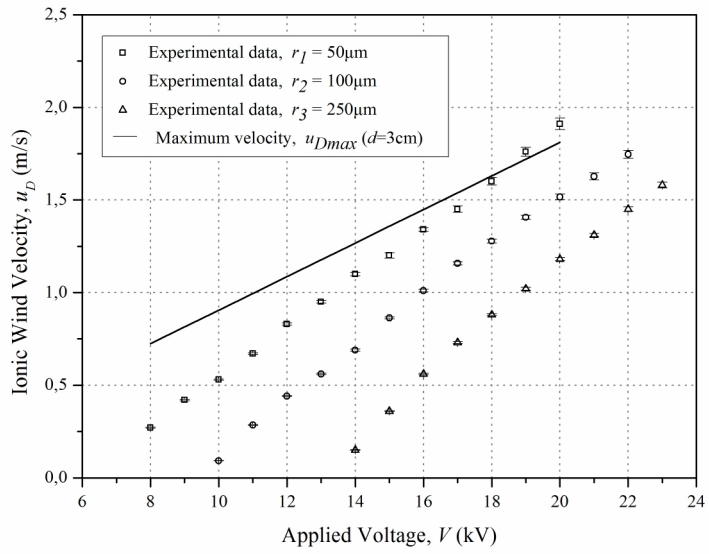
(a)
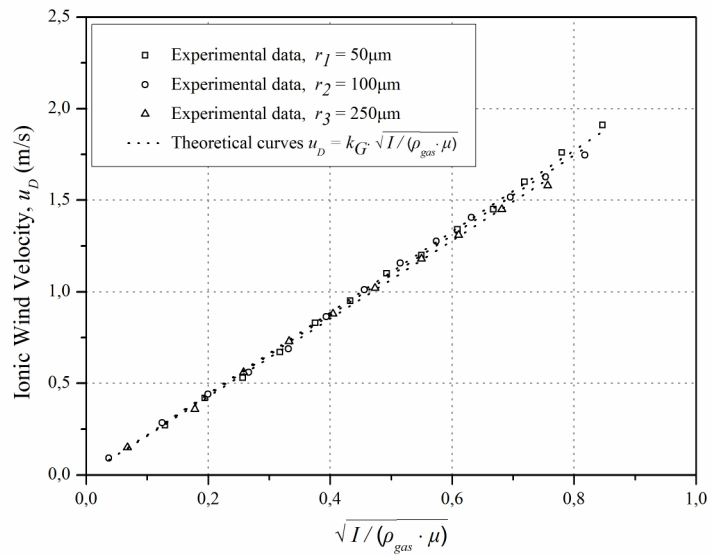
(b)

Figure 5-19 (a) Wind velocity with the applied voltage and (b) wind velocity with the $(I/\rho_{gas}\cdot\mu)^{1/2}$ (r_1=50μm, r_2=100μm and r_3=250μm, d=3cm and R=15mm).

Table 5-6 Function of geometry k_G and discharge cross section A_{cs} with the emitter radius r, for d=3cm and R=15mm.

Emitter radius r (μm)	Function of geometry k_G ($m^{-1/2}$)	Discharge cross section A_{cs} (m^2)
r_1 = 50	2.215	0.0061
r_2 = 100	2.182	0.0063
r_3 = 250	2.132	0.0066

Figure 5-19 shows that the ionic wind velocity has an inversely proportional relationship with the wire radius r, with respect to the applied voltage. The maximum field intensity in the conductor's surface decreases with r and so does the mean field intensity (see Chapter 4), thus the carriers that were produced in the ionization region a, start their drift across the electrode gap with reduced velocity according to equation (2.18). On the other hand, the function of geometry k_G varies within a limited range with r (see table 5-6). This comes in agreement with the small changes in the discharge cross section A_{cs}, due to the fact that the emitter radius has a very small effect on the distribution of the electric field lines in space, corresponding that the area that is formed by the electric field lines between the emitter and the collector electrode is slightly affected.

Influence of the collector radius R on the wind velocity

Measurements of the ionic wind velocity were made on three modules with R_1=5mm, R_2=10mm and R_3=15mm, in order to define the influence of the collector radius R on the wind velocity, while the electrode gap d and the emitter radius r were kept constant at 3cm and 50μm respectively. Fitting curves were drawn, in order to determine the function of geometry k_G, so as the discharge cross section A_{cs}, for different cylinder radii and the results are given in figure 5-20 and table 5-7.
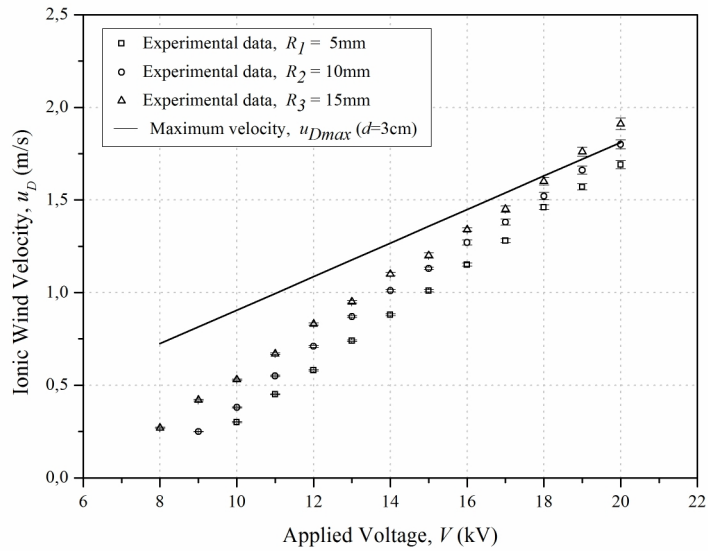
(a)
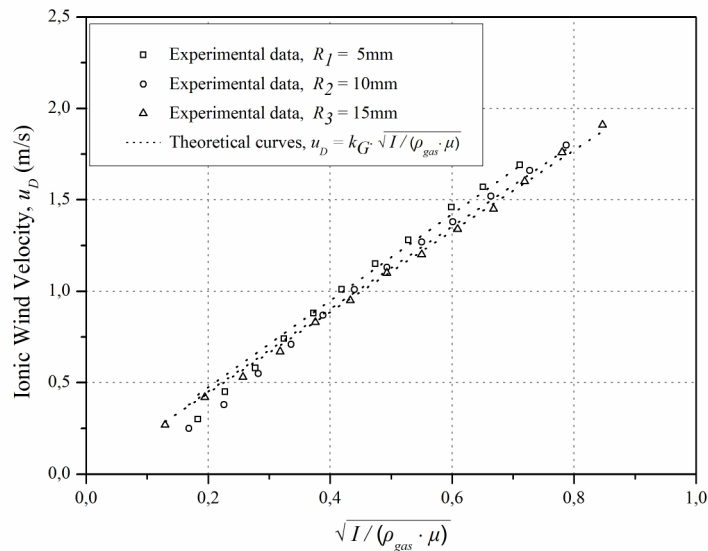
(b)

Figure 5-20 (a) Wind velocity with the applied voltage and (b) wind velocity with the $(I/\rho_{gas}\cdot\mu)^{1/2}$ (R_1=5mm, R_2=10mm and R_3=15mm, d=3cm and r=50µm).

Table 5-7 Function of geometry k_G and discharge cross section A_{cs} with the collector radius R, for d=3cm and r=50µm.

Collector radius R (mm)	Function of geometry k_G (m$^{-1/2}$)	Discharge cross section A_{cs} (m^2)
R_1 = 5	2.371	0.0053
R_2 = 10	2.256	0.0059
R_3 = 15	2.215	0.0061

It becomes clear that the collector radius R has a small effect on the ionic wind velocity (see figure 5-20a). Increased R results in increased field intensity in the emitter's surface due to the higher field inhomogeneity. Thus, the positive ions which start their drift with increased velocity near the ionization region α travel through the gap with higher mean drift velocity according to equation (2.18).

As shown in table 5-7, the function of geometry k_G decreases with R but, on the other hand, the discharge cross section A_{cs} increases. As the collector radius increases, the electric field lines in the area between the emitter and the collector electrode are getting wider, hence the discharge cross section expands.

Flow Efficiency

The electromechanical efficiency in our case may be calculated by the following expression:

$$n = P_{mech}/P_{el} = \frac{1/2 \cdot \rho \cdot A_{cs} \cdot u_D^3}{V \cdot I} \tag{5.5}$$

where V (V) is the applied voltage, I (A) is the corona discharge current, ρ_{gas} (kg/m^3) is the density of air, u_D (m/s) is the ionic wind velocity and A_{cs} (m^2) is the discharge cross section that has been derived according to equation (2.25). The results are presented in figure 5.21.

In our case, the maximum electromechanical efficiency is relatively low (n=0.8%), yet it comes in agreement with other results found in bibliography for different electrode geometries [35]. On the other hand, the values of the wind velocity were high enough (u_D=2.88m/s) even though the wire-cylinder arrangement doesn't seem quite efficient.
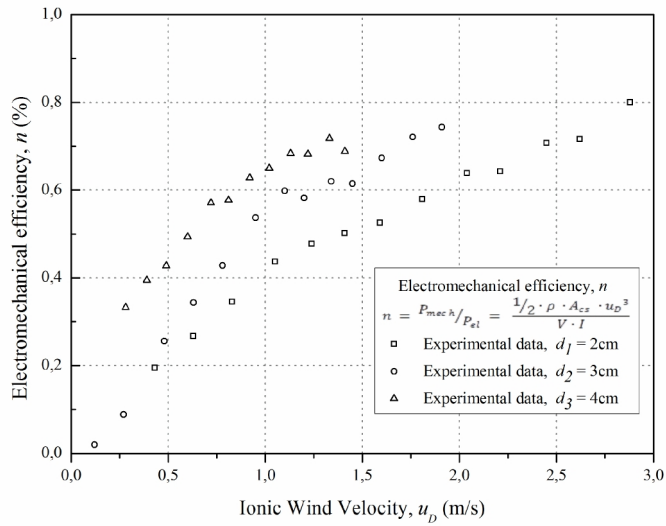
(a)
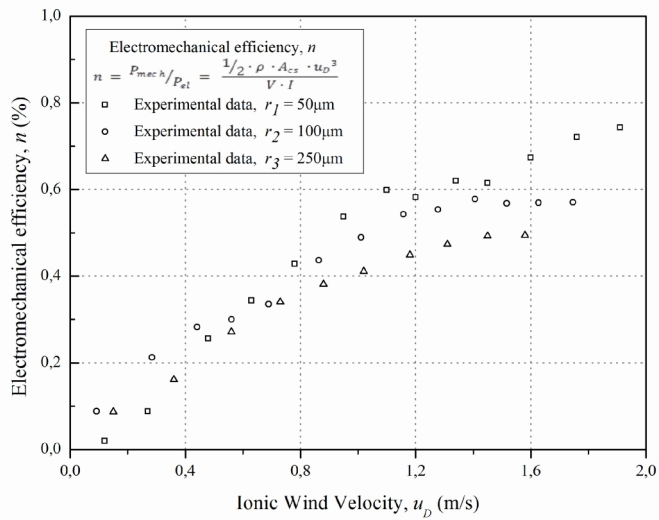
(b)
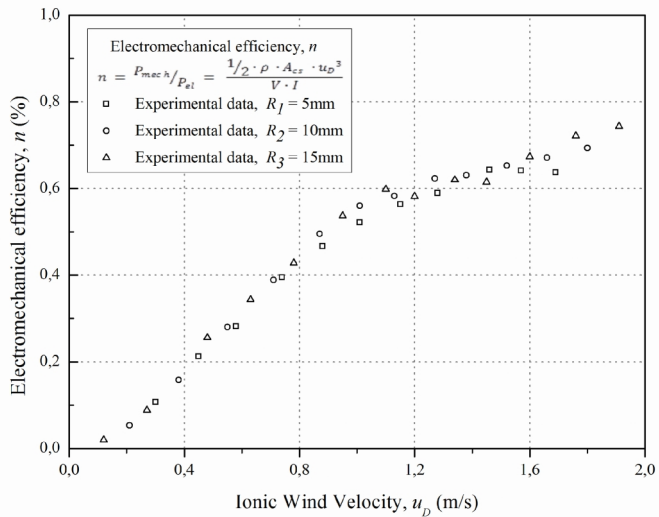
(c)

Figure 5-21 Electromechanical efficiency with the wind velocity for various wire-cylinder configurations. (a) d_1=2cm, d_2=3cm, d_3=4cm with constant r=50μm and R =15mm, (b) r_1=50μm, r_2=100μm, r_3=250μm with constant d=3cm and R =15mm and (c) R_1 =5mm, R_2 =10mm, R_3 =15mm with constant d=3cm and r=50μm).

5.4 GENERATED THRUST

As presented in Chapter 4, dedicated Multiphysics modeling software COMSOL 4.3a has been implemented in order to determine the drift distance of the ions for various angles of incidence to calculate the saturation current density and the unipolar saturation current limit according to equations (4.11) and (4.13). It has been observed that the current density $j_s(\varphi)$ is decreasing abruptly at larger φ angles and as a consequence, the contribution of large incidence angles φ, over 1.6 rads ($\approx$90°), to the current density is generally minimal, due to the 'expansion' of the field lines. In addition, the normalized distribution of $i_s(\varphi)/I_s$ over the cylinder's surface (see figure 4-18), shows that the electric field lines that end on the cylinder's surface at incidence angles over 1.6 rads (~90°) have limited effect on the total saturation current. This is due to the current density distribution over the cylinder's surface which falls abruptly for $\varphi \geq 90°$ (see figure 4-16).

Hence, trajectories with incidence angle equal to 90° could be considered as the boundaries of the 'active' flow volume V_{wc} (see figure 5-22) according to equation (2.33).
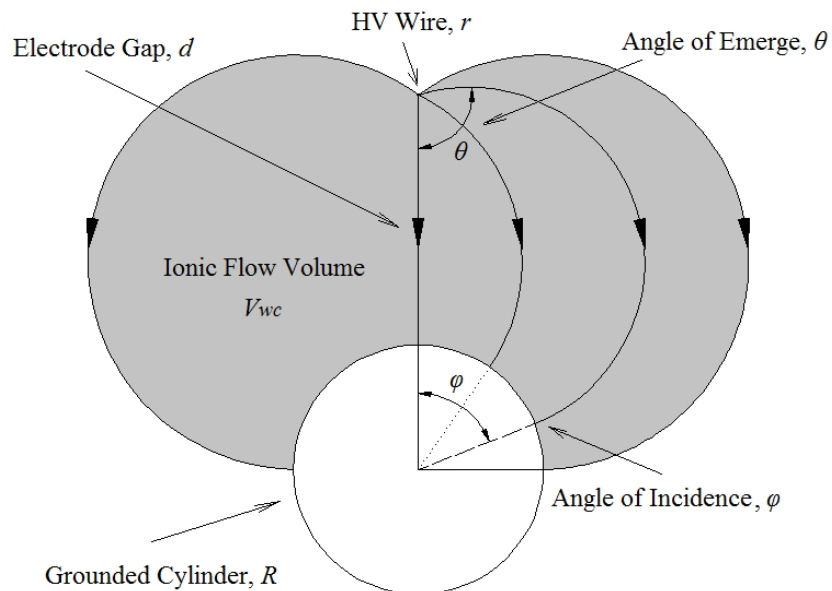
Figure 5-22 Representation of the field lines, which define the boundaries of the 'active' flow volume V_{wc} (grey part). Here, φ_{max}=90°.

Series of measurements have been carried out in order to determine the relationship between the generated thrust and the discharge current, as well as the dependence of the thrust and the field coefficient f_c (equation 2.32) on the electrode gap d and the emitter and collector radii r and R respectively, while the electrode length was constant at 300mm in all cases.

Influence of the electrode gap d on the generated thrust

Investigation of the generated thrust has been conducted on three modules with electrode gap d_1=2cm, d_2=3cm and d_3=4cm, while the emitter and collector radii were 50μm and 15mm respectively. Plots of the generated thrust per unit electrode length against the applied voltage and the corona discharge current are presented in figures 5-23a and 5-23b respectively. Field coefficient f_c was derived from the experimental results (see figure 5-23b), by applying a least square fit to equation (2.32). The average electric field intensity E_{av} and the 'active' ionic flow volume V_{wc} were determined by COMSOL, considering the included volume by the electric field lines with incidence angles up to φ=90° (see figure 5-22). The equivalent homogeneous ionic flow volume was derived in each case according to equation (2.33). The results are given below in τable 5-8.

Table 5-8 Field coefficient f_c and ionic flow volumes V_{wc} and V_{hom} with electrode gap d, for r=50μm and R=15mm.

Electrode gap d (cm)	Field Coefficient f_c	V_{wc} (cm^3)	V_{hom} (cm^3)
d_1 = 2	0.541	665.8	1193.8
d_2 = 3	0.600	919.7	1471.5
d_3 = 4	0.674	1238	1634.7
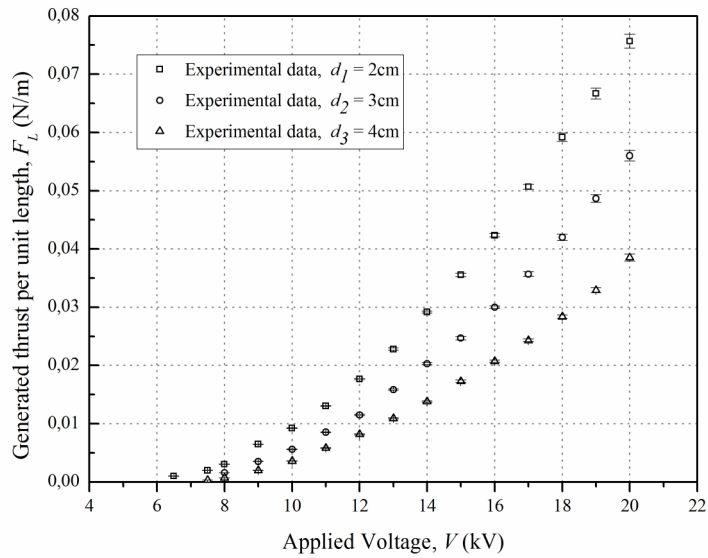
(a)
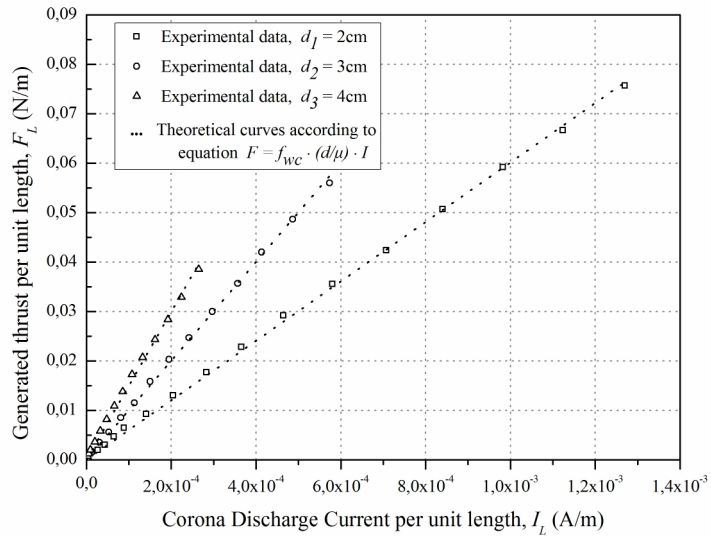
(b)

Figure 5-23 Generated thrust per unit length (N/m) with (a) applied voltage and (b) discharge current (A/m) (d_1=2cm, d_2=3cm and d_3=4cm, r=50µm and R=15mm).

As shown in figure 5-23, the generated thrust reduces with the gap distance d, but on the other hand, the field coefficient f_c increases with d (see table 5-8). This is normal, since larger gaps produce more homogeneous electric fields ($f_c \to 1$).

Influence of the emitter radius r on the generated thrust

The dependence of the generated thrust on the emitter electrode radius r was also investigated, with measurements of the thrust on three modules with r_1=50µm,

r_2=100µm and r_3=250µm, while the electrode gap d and the collector electrode radius R were 3cm and 15mm respectively. In this case also, fitting curves were drawn according to equation (2.32). The average electric field intensity E_{av}, the ionic flow volume V_{wc}, as well as the equivalent homogeneous ionic flow volume V_{hom}, has also been determined as in the previous section. The results are given in figure 5.24 and table 5-9, respectively.

Table 5-9 Field coefficient f_c and ionic flow volumes V_{wc} and V_{hom} with emitter radius r, for d=3cm and R=15mm.

Emitter radius r (µm)	Field Coefficient f_c	V_{wc} (cm^3)	V_{hom} (cm^3)
r_1 = 50	0.600	919.7	1471.5
r_2 = 100	0.597	920.1	1387.1
r_3 = 250	0.594	921	1317.9

As shown in table 5-9, field coefficient f_c differs slightly as far as the emitter radius is concerned. This comes in agreement with the small changes in the ionic flow volume, due to the fact that the emitter radius is very small in comparison with d or R, thus having a small effect on the distribution of the electric field lines in space.
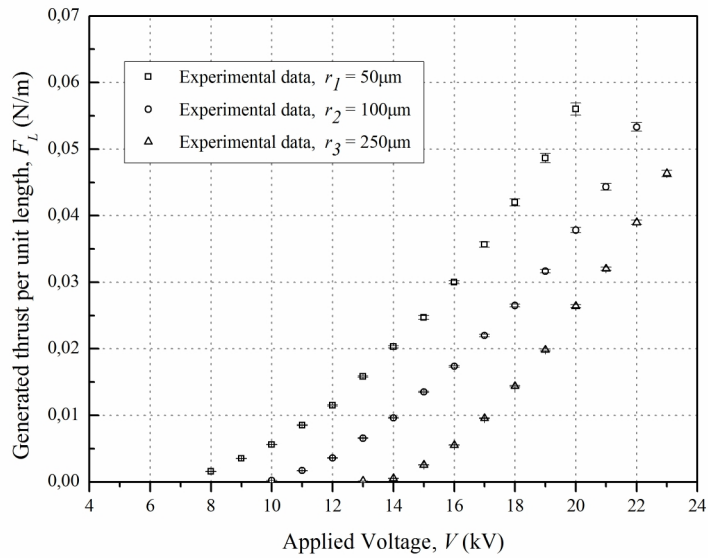
(a)
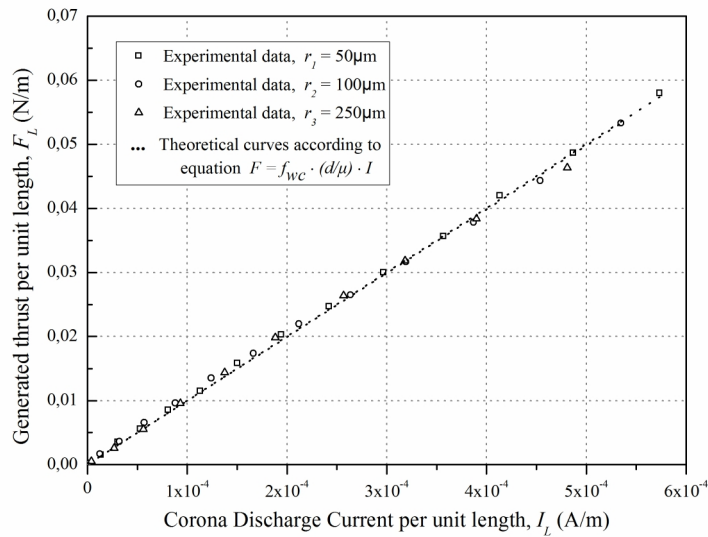
(b)

Figure 5-24 Generated thrust per unit length (N/m) with (a) applied voltage and (b) discharge current (A/m) (r_1=50μm, r_2=100μm and r_3=250μm, d=3cm and R=15mm).

Influence of the collector radius R on the generated thrust

Measurements of the generated thrust were made on three modules with R_1=5mm, R_2=10mm and R_3=15mm, in order to define the dependence of the thrust on the collector electrode radius, while the electrode gap d and the emitter electrode radius r were kept constant at 3cm and 50μm respectively. Fitting curves were drawn, in order to determine the field coefficient f_c for different cylinder radii. The average electric field

intensity E_{av}, the ionic flow volume V_{wc}, as well as the equivalent homogeneous ionic flow volume V_{hom}, were determined accordingly, as shown in table 5-10.
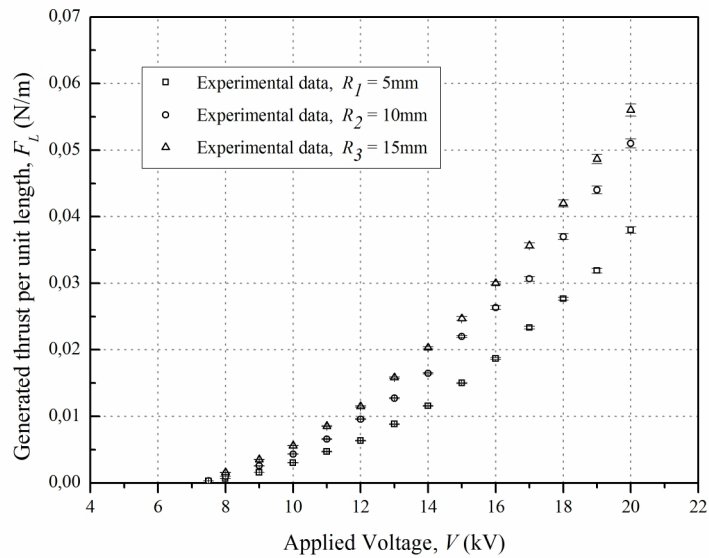
(a)
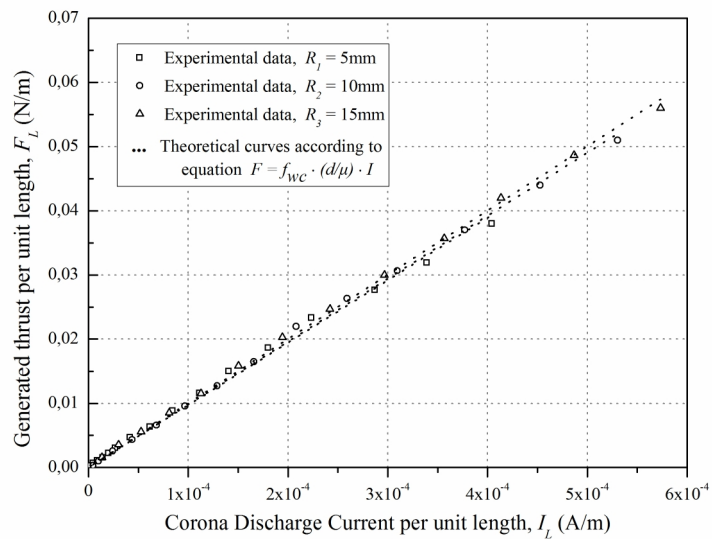
(b)

Figure 5-25 Generated thrust per unit length (N/m) with (a) applied voltage and (b) discharge current (A/m) (R_1=5mm, R_2=10mm and R_3=15mm, d=3cm and r=50μm).

Table 5-10 Field coefficient f_c and ionic flow volumes V_{wc} and V_{hom} with collector radius R for d=3cm and r=50μm.

Collector radius R (μm)	Field Coefficient f_c	V_{wc} (cm^3)	V_{hom} (cm^3)
R_1 = 5mm	0.583	395.3	617
R_2 = 10mm	0.592	648	1028.9
R_3 = 15mm	0.600	919.7	1471.5

It becomes clear the collector radius R has a very small effect on the field coefficient f_c, but on the other hand, V_{wc} and V_{hom}, increase abruptly with R, mainly because of the electric field line spread-out as R increases.

Thrust per unit Power, Thrust efficiency and Flow efficiency

Based on the above results, the generated thrust (N/m) was plotted against consumed power per unit electrode length (W/m) for various geometrical characteristics of the wire-cylinder electrode assembly (see figure 5-26).

In addition, plots of thrust efficiency n_F (N/kW) against the thrust per unit length of the electrodes (N/m) were made for various gaps and emitter and collector radii (see figure 5-27). The thrust efficiency n_F which is the generated thrust per unit consumed power ratio, is frequently used in bibliography as an overall performance evaluation factor [35, 49-53, 122].

On the other hand, the thrust efficiency n_F (N/kW) was plotted against the applied voltage (kV) for different gaps, as well as emitter and collector radii, and the results are shown in figure 5-28.
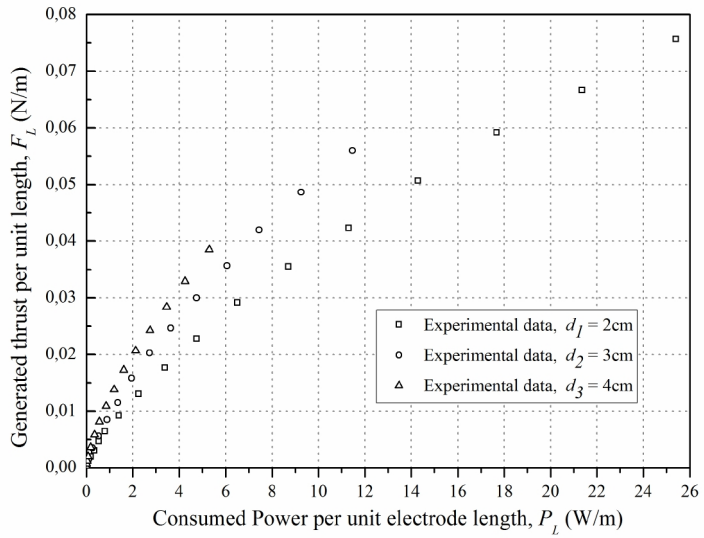
(a)
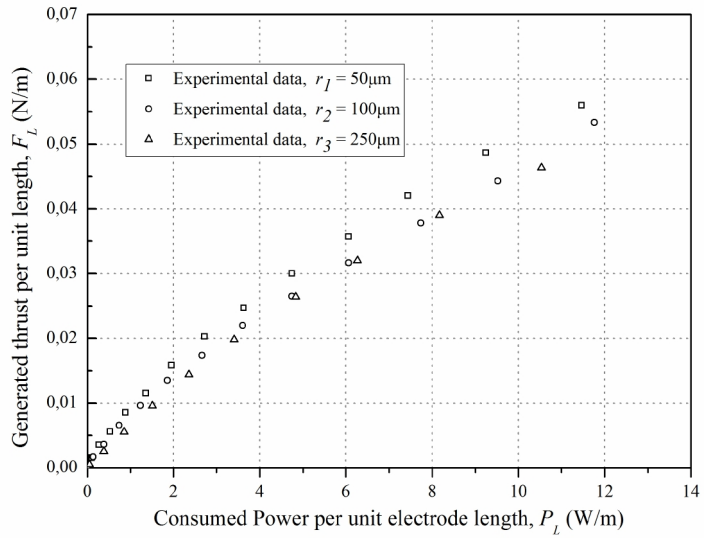
(b)
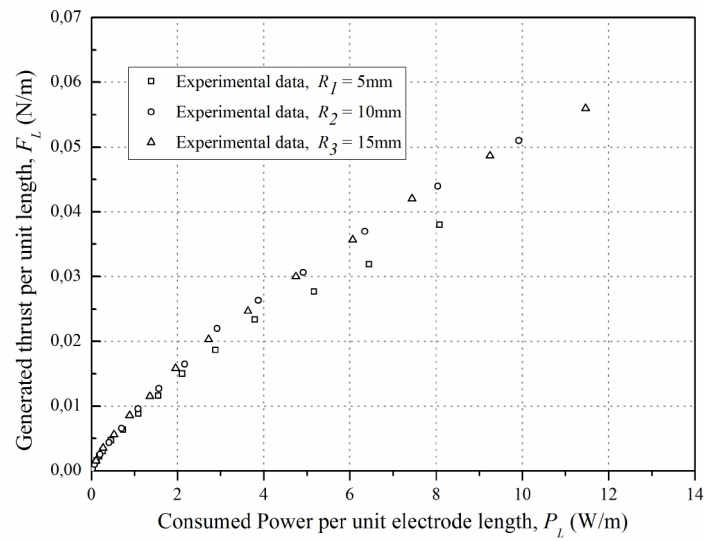
(c)

Figure 5-26 Generated thrust (N/m) with power (W/m) for various geometrical characteristics (a) variable electrode gap d, (b) variable emitter radius r and (c) variable collector radius R.
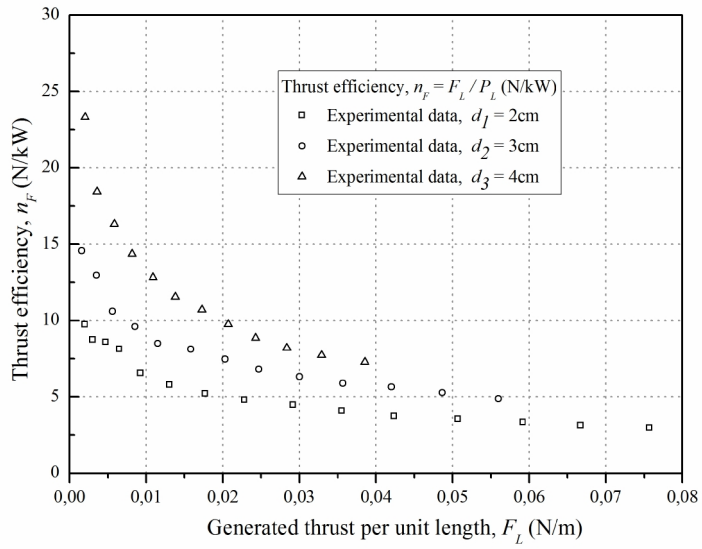
(a)
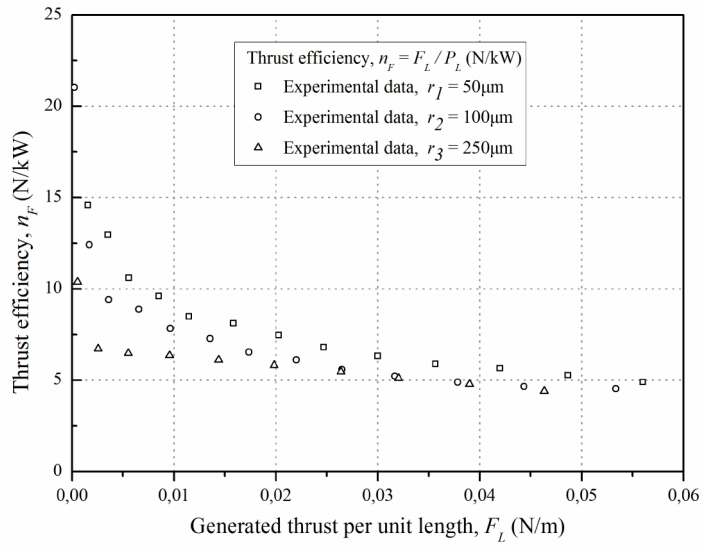
(b)
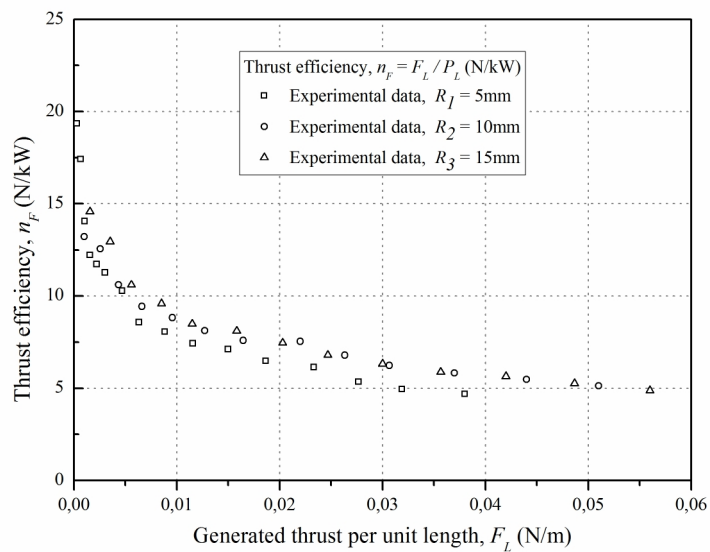
(c)

Figure 5-27 Thrust efficiency n_F (N/kW) with generated thrust (N/m) for various geometrical characteristics (a) variable electrode gap d, (b) variable emitter radius r and (c) variable collector radius R.
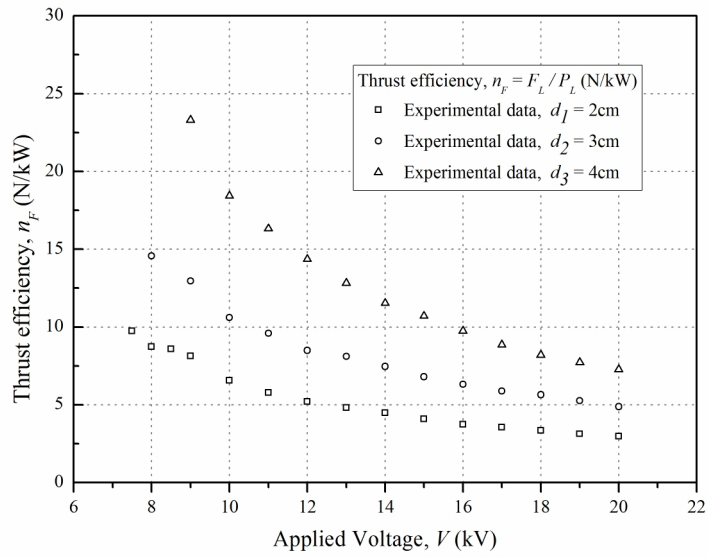
(a)
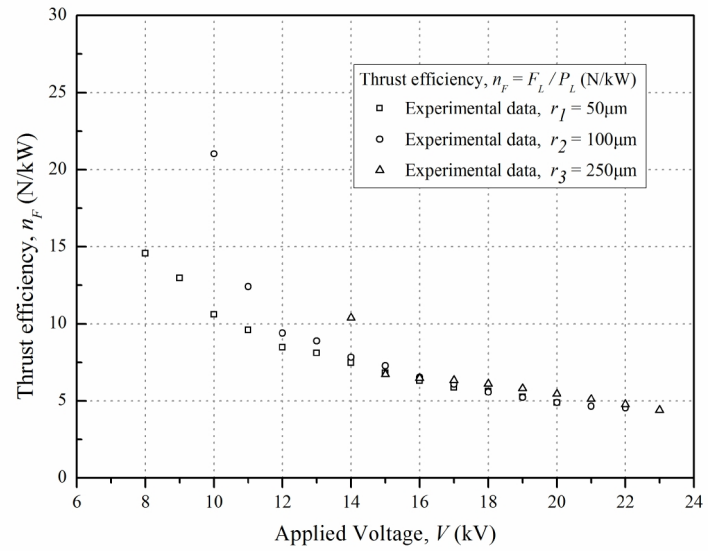
(b)
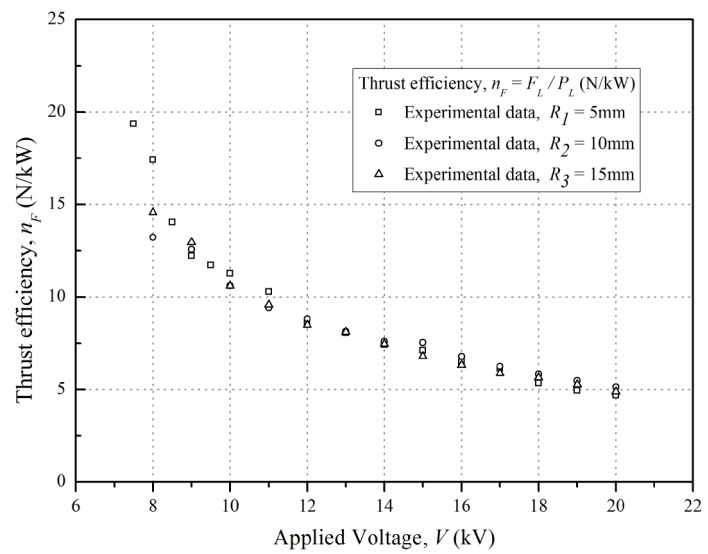
(c)

Figure 5-28 Thrust efficiency n_F (N/kW) with applied voltage (kV) for various geometrical characteristics (a) variable electrode gap d, (b) variable emitter radius r and (c) variable collector radius R.

It becomes clear from figures 5-26, 5-27 and 5-28, that in terms of thrust efficiency, the electrode gap d, primarily, and the wire radius r, secondarily, play the most important role in the thrust per unit power ratio. The cylinder radius R seems to have limited effect.

The maximum value of the generated thrust (F_L=0.076N/m at 20kV) was measured for the shortest gap (d_1=20mm) as shown in figure 5-26a, but on the other hand, the efficiency was very low at the same time ($\approx$3N/kW). Although the generated thrust reduces with d, large gaps favor the thrust per unit power ratio.

The maximum values of efficiency were recorded for the larger gap d_3=40mm (n_F=23.3N/kW) as shown in figures 5-27a and 5-28a, but with very low generated thrust at the same time ($\approx$0.002N/m). This may be attributed to the fact that higher efficiency values were obtained for lower voltages, as shown in figure 5-28.

Small emitter radii produce higher thrust values, with higher efficiency (see figures 5-26b and 5-27b). On the other hand, as far as the collector electrode radius is concerned, increased R resulted in increased generated thrust and thrust per unit power ratio (see figures 5-26c and 5-27c).

The produced mechanical power in our case may be calculated by:

$$P_{mech} = F \cdot u_D \tag{5.6}$$

The electromechanical efficiency is then deduced by the following expression:

$$n = \frac{P_{mech}}{P_{el}} = \frac{F \cdot u_D}{V \cdot I} \tag{5.7}$$

where V (V) is the applied voltage, I (A) is the corona discharge current, u_D (m/s) is the ionic wind velocity and F (N) is the generated thrust due to the EHD effect.

The ionic wind velocity measurements have shown that velocities with an average value of 2.88m/s may be reached within the range of the geometry of this study (see

Chapter 5.3). In this case, the electromechanical efficiency is relatively low (n=0.8%). Even though the wire-cylinder arrangement doesn't seem quite efficient, the thrust per unit power ratio that has been achieved was high enough considering other similar studies [49, 52, 53, 122].

CHAPTER 6 - CONCLUSIONS

The physical phenomenon of the EHD mechanism has been demonstrated and validated through simulations, experiments and comparisons in the wire-cylinder electrode configuration under HV DC application. The operational parameters of the EHD effect, such as the electric field and potential distribution, in altered electrode arrangements have been investigated, while their dependence on geometrical characteristics of the electrodes, such as the electrode length, the electrode gap and the emitter and collector electrode radii, has been examined. In addition, the critical variables that enhance or undermine the EHD effect have been determined. On this purpose, both computer modelling and experimental studies have been conducted.

The electric field and potential distribution in typical wire-cylinder electrode arrangements, under HV DC application, has been studied by implementing the Finite Element Analysis (FEA). On this purpose, open source FEA modelling software F.E.M.M. ver. 4.2 and dedicated Multiphysics software COMSOL ver. 4.3a have been implemented. The maximum electric field strength E_{max}, as well as the minimum electric field strength E_{min}, has been examined considering geometrical characteristics of the electrodes such as the wire radius r, the electrode spacing d and the cylindrical electrode radius R. The investigation has shown that E_{max} is mainly associated with the wire electrode radius r. Smaller wire radii result in higher field intensities around the wire, especially at the wire's surface, where the maximum electric field intensity is observed. In addition, E_{max} was found to be inversely proportional to the electrode gap d. Moreover, larger cylinder radii R led to higher E_{max} values, for constant r and d. On the other hand, E_{min} is strongly related to the electrode gap d, while the wire radius r and the cylindrical electrode radius R have a limited impact on the minimum electric field intensity. The potential distribution along the axis of the gap in all cases remains almost the same regardless of the gap distance d. Further analysis of all simulation results has shown that the maximum electric field intensity may be approximated by an empirical formula (equation 4.1). The correlation of the simulated data with the empirical formula results was found to be satisfactory, with an absolute error lower than 4% in all cases.

An approximate technique for the determination of the unipolar saturation current limit in the wire-cylinder electrode configuration, based on the analysis of the electric

field lines has also been proposed. The varying length of electric field lines has been determined by FEA simulations and it has been proven that the ionic saturation current limit may be calculated by an analytic formula, which defines the saturation current limit as a function of the applied voltage and other geometrical characteristics of the electrodes. The unipolar current density distribution over the cylinder's surface is similar to the well-known Warburg distribution which has been observed in other electrode geometries as well. According to the results, the closest part of the cylinder's surface to the wire, contributes at most for the total current, thus leaving the remaining part almost inactive (see figure 4-18). The proposed model has been verified through experimental investigation, which has shown that the wire-cylinder unipolar corona discharge current is closely related to the specified theoretical limits.

The experimental study of the positive corona discharge current in the case of a parallel wire-cylinder arrangement has shown that the corona discharge current is related to the applied voltage through a quadratic relationship which also involves a coefficient k. This finding is in good agreement with the well-known Townsend's general model for the corona current which has previously been applied to other typical geometries. The discharge current decreases with the emitter radius and the electrode gap, but on the other hand, increases with the collector radius. Based on the analysis of the experimental measurements, coefficient k was found to be inversely proportional to the gap distance, yet increasing with the emitter and collector radii. The analysis of the experimental results has led to an expression for coefficient k as a function of the wire-cylinder distance d and the wire and cylinder radii r and R respectively. This formula resembles similar formulae found in literature for other electrode geometries and may be used in various applications where corona discharge generation with a wire-cylinder electrode pair could be used for. In addition, the CIV in each case has been experimentally determined and the results have been verified with simulation results, as well as with empirical formulae values. Simulation and experimental results have shown that the CIV was mainly associated to the wire radius r, while the distance d between the electrodes had a secondary importance. On the other hand, the cylinder's radius R seemed to have insignificant affection to the inception of the positive corona discharges.

The study of the positive corona ionic wind generation has shown that the ionic wind velocity is an approximately linear function of the applied voltage and is

proportional to the square root of the discharge current. Parametric analysis in our case showed that the ionic wind velocity decreases with the electrode gap d and the emitter radius r, but, on the contrary, increases with the cylinder radius R. The electrode gap d and the collector electrode radius R, are of high importance to the field line distribution, as noted before, and consequently to the discharge cross section A_{cs}, while the emitter radius r seems to have a minimal effect on A_{cs}. As the gap increases, the function of geometry k_G increases as well, while k_G reduces with the collector radius R. The influence of the emitter radius r seems to be of secondary importance for the function of geometry.

Theoretical and experimental investigation of the generated thrust due to the EHD effect has also been conducted. Due to the fact that the reduction in weight of the electrode system that has been measured with the precision balance was ranging between 0-2.31gr (0.58% of the overall weight) the assembly could not balance, hence the measurements have not been biased by the EHD effect. A theoretical model has been presented, based on the momentum exchanges, through collisions, between the field force-accelerated ions and the electrically neutral air molecules. A field coefficient f_c has been introduced in order to determine the generated thrust as a function of the corona current intensity. Experimental results have shown a linear relationship between the generated thrust and the corona discharge current, while parametric analysis showed that smaller electrode gaps and emitter radii resulted in increased thrust. The experimental findings were in good agreement with theoretical expectations according to the proposed model. The wire-cylinder setup that has been used seems to be quite efficient in terms of thrust per unit power ratio [49, 52, 53, 122].

The variation of the key EHD flow parameters with the electrode configuration at 20kV is presented in Table 6-1. It becomes clear that the maximum velocity and thrust values (2.88m/s and 0.076N/m respectively) have been obtained with the shortest gap (d= 2cm), which produced the higher field inhomogeneity and as a consequence the higher electric field intensity (E_{max}= 55.6·10^6V/m). At the same time the thrust per unit power ratio was 2.82N/kW with an electromechanical efficiency of 0.81%. On the other hand, the larger gap (d= 4cm) produced lower velocity and thrust values (1.41m/s and 0.039N/m respectively at 20kV potential difference) but, favoured the thrust per unit power ratio (7.28N/kW) and the efficiency (1.02%).

Generally, small emitter radii and large gaps favour the electromechanical efficiency with respect to the wind velocity and the generated thrust. Moreover, large gaps and collector radii are in favour of the thrust per unit power ratio. On the other hand, as far as the maximum values of velocity and thrust are concerned, an optimized electrode configuration would be consisted of a thin emitter wire and a significantly larger radius collector set in a limited distance to each other, within the limits of the geometry used in this study.

Table 6-1 Key EHD parameter's variation with the electrode configuration at 20kV potential difference.

Electrode configuration	Varying parameter		E_{max} (V/m)	u_D (m/s)	F_L (N/m)	n_F (N/kW)	n (%)
1st set (r = 50μm and R = 15mm)	d (cm)	2	$55.6 \cdot 10^6$	2.88	0.076	2.82	0.81
		3	$51.4 \cdot 10^6$	1.91	0.056	4.88	0.93
		4	$48.6 \cdot 10^6$	1.41	0.039	7.28	1.02
2nd set (d = 3cm and R = 15 mm)	r (μm)	50	$51.4 \cdot 10^6$	1.91	0.056	4.88	0.93
		100	$28.2 \cdot 10^6$	1.52	0.038	4.89	0.74
		250	$13 \cdot 10^6$	1.18	0.026	5.46	0.64
3rd set (r = 50μm and d = 3 cm)	R (mm)	5	$47.2 \cdot 10^6$	1.69	0.038	4.78	0.80
		10	$50 \cdot 10^6$	1.8	0.051	5.14	0.92
		15	$51.4 \cdot 10^6$	1.91	0.056	4.88	0.93

APPENDIX

During the PhD research some BEng and MSc dissertations have been co-supervised along with the official supervisor Professor Antonios Moronis.

M. Konstantinidi, 2011, "Study of EHD Effect in Asymmetric High Voltage Capacitors", MSc Dissertation, Heriot-Watt University.

K. Kantouna, 2011, "Electric field and air flow modeling in high voltage electrode configurations during corona discharge", MSc Dissertation, Heriot-Watt University.

E.D. Fylladitakis, 2012, "Evaluation of the ionic wind effect - Air cooling applications and e-learning adaptation", MSc Dissertation, Heriot-Watt University.

N. Simou, 2012, "Modeling and simulation of the Electric field distribution with the aid of Finite Element Method, under high voltage DC in asymmetric electrode configuration", BEng Dissertation, Heriot-Watt University.

The main results of these dissertations, or their development, have been published in form of papers in scientific journals and international conference proceedings and are not included in this thesis.

E.D. Fylladitakis, A.X. Moronis & **K.N. Kiousis**, 2014, "*Experimental evaluation of a needle-to-grid EHD pump prototype for semiconductor cooling applications*", International Journal of Circuits systems and Signal Processing, Vol. 8, pp. 337-342.

E.D. Fylladitakis , A.X. Moronis & **K.N. Kiousis,** "Design of a prototype EHD air pump for electronic chip cooling applications", IOP International Journal of Plasma Science and Technology, Vol.16, No.5, pp. 491-501.

E.D. Fylladitakis, A.X. Moronis & **K.N. Kiousis**, "*Evaluation of a Single Needle to Grid EHD Pump Prototype for Forced Convection Cooling Applications*", Proceedings of the 1st Europment International Conference on Applied Mathematics and Computational Methods in Engineering, Rhodes, Greece, July 17-19, 2013, pp. 282-287.

K. Kantouna, G.P. Fotis, **K.N. Kiousis**, L. Ekonomou, G. Chatzarakis, "*Finite Element Method Analysis of the Electric Field in Cylinder‑Wire‑Cylinder Electrode Configuration during Corona Discharge*", Proceedings of the 1st International Conference on Circuits, Systems, Communications, Computers and Applications, Iasi, Romania, June 13-15, 2012, pp. 204-208.

References

[1] L. B. Loeb, *Electrical coronas*, University of California Press, London, 1965.

[2] I. Newton, *Optics*, London, England, 1718.

[3] M. Faraday, *Experimental Researches in Electricity*, London, England, 1839.

[4] J. Maxwell, *Treatise on Electricity and Magnetism*, London, England, 1873.

[5] O. Stuetzer, *Ion Drag Pressure Generation*, Journal of Applied Physics, pp. 984-994, 1959.

[6] M. Robinson, *Movement of air in the electric wind of the corona discharge*, Transactions of the American Institute of Electrical and Electronic Engineers, pp. 143-150, 1961.

[7] A. Chattock, *On the velocity and mass of the ions in the electric wind in air*, Philosophical Magazine Series 5, 48, 294, pp. 401-420, 1899.

[8] J. Townsend, *Electricity in gases*, Oxford University press, New York, 1915.

[9] F. Peek, *Dielectric Phenomena in High Voltage Engineering*, McGraw-Hill Press, New York, 1929.

[10] M. Robinson, *A History of the Electric Wind*, American Journal of Physics, 30, pp. 366-372, 1962.

[11] P. Bérard, D. Lacoste, C. Laux, *Measurements and simulations of the ionic wind produced by a dc corona discharge in air, helium and argon*, 38th AIAA Plasma dynamics and Lasers Conference in conjunction with the 16th Conference on MHD Energy Conversion, pp. 1-12, 2007.

[12] A. Martins, M. Pinheiro, *Modeling of an EHD corona flow in nitrogen gas using an asymmetric capacitor for propulsion*, Journal of Electrostatics, pp. 133-138, 2011.

[13] D. Buehler, *Exploratory research on the phenomenon of the movement of high voltage capacitors*, Journal of Space Mixing, 2, pp. 1-22, 2004.

[14] R. Sigmond, *Simple approximate treatment of unipolar space-charge-dominated coronas: The Warburg law and the saturation current*, Journal of Applied Physics, 53, 2, pp. 891-898, 1982.

[15] J. Thomson, G. Thomson, *Conduction of Electricity through Gases*, London, Cambridge University, 1933.

[16] T. Matsumoto, *DC corona loss of coaxial cylinders*, Journal of Electrical Engineering in Japan, 88, 1968.

[17] P. Giubbilini, *The current-voltage characteristics of point-to-ring corona*, Journal of Applied Physics, 64, 30-37, 1988.

[18] R. Waters, T. Rickard, W. Stark, *The Structure of the Impulse Corona in a Rod/Plane Gap. I. The Positive Corona*, Proceedings of the Royal Society, London, pp. 1-25, 1970.

[19] G. Ferreira, O. Oliveira, J. Giacometti, *Point-to-plane corona: Current-voltage characteristics for positive and negative polarity with evidence of an electronic component*, Journal of Applied Physics, 59, pp. 3045-3049, 1986.

[20] H. Wintle, *Unipolar wire-to-plane corona: accuracy of simple approximations*, Journal of Electrostatics, 28, 149-159, 1992.

[21] F. Carreno, E. Bernabeu, *On wire-to-plane positive corona discharge*, Journal of Physics D: Applied Physics, 27, 1994.

[22] M. Abdel-Salam, A. Hashem, A. Turky, A. Aziz, *Corona performance of conductor-to-plane gaps as influenced by underneath grounded and negatively stressed metallic grids*, Journal of Physics D: Applied Physics, pp. 1684-1691, 2007.

[23] B. Komeili, J. Chang, G.. Harvel, C. Ching, D. Brocilo, *Flow characteristics of wire-rod type electrohydrodynamic gas pump under negative corona operations*, Journal of Electrostatics, pp. 342:353, 2008.

[24] B. Buchet, M. Goldman, A. Goldman, *The nature of the permanent current in point to plane corona discharges with direct voltage*. Journal of Les Comptes Rendus de l'Académie des sciences, 263, pp. 356-359, 1966.

[25] E. Moreau, *Airflow control by non-thermal plasma actuators*, Journal of Physics D: Applied Physics, pp. 605-636, 2007.

[26] E. Moreau, L. Léger, G. Touchard, *Effect of a DC surface-corona discharge on a flat plate boundary layer for air flow velocity up to 25m/s*, Journal of Electrostatics, pp. 215-225, 2006.

[27] J. Wilson, H. Perkins, W. Thompson, *An Investigation of Ionic Wind Propulsion*, Glenn Research Center Cleveland, Ohio, 2009.

[28] K. Nikas, A. Varonos, G.. Bergeles, *Numerical simulation of the flow and the collection mechanisms inside a laboratory scale electrostatic precipitator*, Journal of Electrostatics, 63, pp. 423-443, 2005.

[29] J. Kim, H. Lee, H. Kim, A. Ogata, *Electrospray with electrostatic precipitator enhances fine particles collection efficiency*, Journal of Electrostatics, 68, 305-310, 2010.

[30] M. Barletta, A. Gisario, *Electrostatic spray painting of carbon fibre-reinforced epoxy composites*, Journal of Progress in Organic Coatings, 64, 339-349, 2009.

[31] A. Jaworek, A. Sobczyk, *Electrospraying route to nanotechnology: An overview*, Journal of Electrostatics, 66, 197-219, 2008.

[32] M. Goldman, *Corona discharges and their applications*, Physical Science Measurement and Instrumentation, Management and Education - Reviews, IEE Proceedings A, 128, pp. 298-302, 1981.

[33] M. Goldman, A. Goldman, R. Sigmond, *The corona discharge, its properties and specific uses*, Journal of Pure Applied Chemistry, 57, 1353-1362, 1985.

[34] J. Chang, P. Lawless , T. Yamamoto, *Corona discharge processes*, Plasma Science, IEEE Transactions, 19, pp. 1152-1166, 1991.

[35] E. Moreau, G. Touchard, *Enhancing the mechanical efficiency of electric wind in corona discharges*, Journal of Electrostatics, 66, pp. 39-44, 2008.

[36] J. Matéo-Vélez, P. Degond, F. Rogier, A. Séraudie, F. Thive, *Modelling wire-to-wire corona discharge action on aerodynamics and comparison with experiment*, Journal of Physics D: Applied Physics, 41, pp. 1-11, 2008.

[37] P. Magnier, D. Hong, A. Leroy-Chesneau, J. Pouvesle, J. Hureau, *A DC corona discharge on a flat plate to induce air movement*, Journal of Electrostatics, pp. 655-659, 2007.

[38] K. Hyun, C. Chun, *The wake flow control behind a circular cylinder using ion wind*, Journal of Experiments in Fluids, pp. 541-552, 2003.

[39] N. Benard, J. Jolibois, E. Moreau, *Lift and drag performances of an axisymmetric airfoil controlled by plasma actuator*. Journal of Electrostatics, 67, pp. 133-139, 2009.

[40] S. Grundmann, C. Tropea, *Experimental transition delay using glow-discharge plasma actuators*. Journal of Experiments in Fluids, 42, pp. 653-657, 2007.

[41] J. Seyed-Yagoobi, *Electrohydrodynamic pumping of dielectric liquids*, Journal of Electrostatics, 63, pp. 861-839, 2005.

[42] J.-D. Moon, *An EHD Gas Pump Utilizing a Ring/Needle Electrode*, IEEE Transactions on Dielectrics and Electrical Insulation, 16, 2, pp. 352- 358, 2009.

[43] J.-D. Moon, *An EHD Gas Pump Utilizing a Wet Porous Point Electrode*, IEEE Transactions on Dielectrics and Electrical Insulation, 16, 3, pp. 622-628, 2009.

[44] A. Alamgholilou, E. Esmaeilzadeh, *Experimental Investigation on Hydrodynamics and Heat Transfer of Fluid Flow into Channel for Cooling of Rectangular Ribs by Passive and EHD Active Enhancement Methods*, Journal of Experimental Thermal and Fluid Science, 38, pp. 61-73, 2012.

[45] S. Laohalertdecha, S. Wongwises, *Effect of EHD on heat transfer enhancement during two-phase condensation of R-134a at high mass flux in a horizontal smooth tube*, Journal of Heat and Mass Transfer, 43, 9, pp 871-880, 2007.

[46] L. Velasquez-Garcia, A. Akinwande, M. Martinez-Sanchez, *A Micro-Fabricated Linear Array of Electrospray Emitters for Thruster Applications*, Journal of Microelectromechanical Systems, 15, pp. 1260-1271, 2006.

[47] W. Miller, P. Miller, T. Drummond, *Force characterization of asymmetrical capacitor thrusters in air*. American Institute of Aeronautics and Astronautics, Frontiers of propulsion science: progress in astronautics and aeronautics, 227, pp. 293-327, 2009.

[48] D. Kirtley, J. Fife, *Modeling, simulation, and design of an electrostatic colloid thruster*, Proceedings of the 29th IEEE International Conference on Plasma Science, 2002.

[49] L.Pekker, M. Young, *A Model of an Ideal Electrohydrodynamic Thruster*, Air Force Research Laboratory, 2010.

[50] Z.Lin, L. Teck-Meng, *Thrust origin in EHD lifters*, IEEE Industry Applications Society Annual Meeting (IAS), 2011.

[51] M. Young, S.Keith, A. Pancotti, *An Overview of Advanced Concepts for Near-Space Systems*, Air Force Research Laboratory, 2009.

[52] K. Masuyama, S. Barrett, *On the performance of electrohydrodynamic propulsion*, Proceedings of the Royal Society A: Mathematical, Physical and Engineering Sciences, 469, pp. 21-54, 2013.

[53] D. Cravens, *Electric propulsion study (AL-TR-89-040)*, Air Force Astronautics Lab, Edwards AFB, CA, USA, 1990.

[54] H. Chih-Peng, N. Jewell-Larsen, I. Krichtafovitch, S. Montgomery, J. Dibene, A. Mamishev, *Miniaturization of Electrostatic Fluid Accelerators*, Journal of Microelectromechanical Systems, pp. 809-815, 2007.

[55] J. Darabi, H. Wang, *Development of an Electrohydrodynamic Injection Micropump and its Potential Application in Pumping Fluids in Cryogenic Cooling Systems*, Journal of Microelectromechanical Systems, pp. 747-755, 2005.

[56] H. Chih-Peng, N. Jewell-Larsen, I. Krichtafovitch, A. Mamishev, *Heat-Transfer-Enhancement Measurement for Microfabricated Electrostatic Fluid Accelerators*, Journal of Microelectromechanical Systems, pp. 111:118, 2009.

[57] H. Velkoff , F. Kulacki, *Electrostatic cooling*, ASME Paper No. 77-0E-36, Design Engineering Conference and Show, 1977.

[58] S. Marco, H. Velkoff*, Effect of electrostatic fields on free convection heat transfer*, ASME Paper No. 63-HT-9, 1963.

[59] H. Velkoff, R. Godfrey, *Low-velocity heat transfer to a flat plate in the presence of a corona discharge in air*, Journal of Heat Transfer, 101, pp. 157-163, 1979.

[60] K. Kibler, H. Carter Jr., *Electrocooling in gases*, Journal of Applied Physics, 45, pp. 4436-4440, 1974.

[61] B. Owsenek, J. Seyed-Yagoobi, *Theoretical and experimental study of electrohydrodynamic heat transfer enhancement through wire-plate corona*, Journal of Heat Transfer, 119, pp. 604-610, 1997.

[62] B. Owsenek, J. Seyed-Yagoobi, R. Page, *Experimental investigation of corona wind heat transfer enhancement with a heated horizontal flat plate*, Journal of Heat Transfer, 117, pp. 309-315, 1995.

[63] H. Kalman, E. Sher, *Enhancement of heat transfer by means of a corona wind created by a wire electrode and confined wings assembly*, Journal of Applied Thermal Engineering, 21, pp. 265-282, 2001.

[64] M. Molki, K. Bhamidipati, *Enhancement of convective heat transfer in the developing region of circular tubes using corona wind*, Journal of Heat and Mass Transfer, 47, pp. 4301-4314, 2004.

[65] N. Jewell-Larsen, E. Tran, I. Krichtafovitch, A. Mamishev, *Design and optimization of electrostatic fluid accelerators*, IEEE Transactions on Dielectrics and Electrical Insulation, 13, pp. 191-203, 2006.

[66] D. Schlitz, S. Garimella, T. Fisher, *Microscale ion-driven air flow over a flat plate*, Paper no: HT-FED04-56470, Proceedings of ASME Heat Transfer/Fluids Engineering Summer Conference, 2004.

[67] V. Patel, J. Seyed-Yagoobi, *Dielectric fluid flow generation in meso-tubes with micro-scale electrohydrodynamic conduction pumping*, Proceedings of the IEEE International Conference on Dielectrics and Liquids, pp.1-4 2011.

[68] D. Go, T. Fisher, S. Garimella, *Direct simulation Monte Carlo analysis of microscale field emission and ionization of atmospheric air*, Paper no:IMECE 2006-14476, Proc. of ASME Int. Mechanical Engineering Congress and Exposition, 2006.

[69] W. Zhang, T. Fisher, S. Garimella, *Simulation of ion generation and breakdown in atmospheric air*, Journal of Applied Physics, 96, pp. 6066-6072, 2004.

[70] M. Peterson, W. Zhang, T. Fisher, S. Garimella, *Low-voltage ionization of air with carbon-based materials*, Journal of Plasma Sources Science and Technology, 14, pp. 654-660, 2005.

[71] D. Go, S. Garimella, T. Fisher, *Numerical simulation of microscale ionic wind for local cooling enhancement*, Proceedings of the 10th Intersociety Conference on Thermal and Thermomechanical Phenomena in Electrical Systems, 2006.

[72] D. Go, T. Fisher, S. Garimella, *Ionic winds for locally enhanced cooling*, Journal of Applied Physics, 102, art. no. 053302, 2007.

[73] L. Zhao, K. Adamiak, M. Mazumder, *Numerical and Experimental Studies of the Electrohydrodynamic Pump for Sampling System on Mars*, Proceedings of ESA Annual Meeting on Electrostatics, Paper O3, 2008.

[74] M. Pearson, J. Seyed-Yagoobi, *Experimental study of EHD conduction pumping at the meso- and micro-scale*, Journal of Electrostatics, 69, 6, pp. 479-485, 2011.

[75] J. Chang, H. Tsubone, Y. Chun, A. Berezin,, K. Urashima, *Mechanism of Electrohydrodynamically Induced Flow in a Wire-non-parallel Plate Electrode Type Gas Pump*, Journal of Electrostatics, 67, pp. 335-339, 2009.

[76] H. Tsubone, B. Komeili, S. Minami, G.D. Harvel, K. Urashima, C.Y. Ching, J.S. Chang, F*low characteristics of dc wire-non-parallel plate electrohydrodynamic gas pump*, Journal of Electrostatics, 66, pp. 115-121, 2008.

[77] F. Yang, N. Jewell-Larsen, D. Brown, K. Pendergrass, D. Parker, I. Krichtafovitch, A. Mamishev, *Corona driven air propulsion for cooling of electronics*, Proceedings of the 13th International Symposium in High Voltage Engineering, pp. 1-4, 2003

[78] H. Wang, N. Jewell-Larsen, A. Mamishev, *Thermal management of microelectronics with electrostatic fluid accelerators*, Journal of Applied and Thermal Engineering, 51, 1-2, pp. 190-211, 2013.

[79] A. Napartovich, *Critical Review of Atmospheric Pressure Discharges Producing Nonthermal Plasma*,Proceedings of International Symposium on High Pressure Low Temperature Plasma Chemistry, 2000.

[80] H. Schmid, S. Stolz, H. Buggisch, *On the modelling of the electro-hydrodynamic flow field in electrostatic precipitators*, Journal of Flow, Turbulence and Combustion, 68, 1, pp. 63-89, 2002.

[81] R. Huang, W. Sheu, C. Wang, *Heat transfer enhancement by needle-arrayed electrodes - An EHD integrated cooling system*, Journal of Energy Conversion and Management, 50, 7, pp. 1789-1796, 2009.

[82] K Yanallah, *Ozone generation by negative corona discharge: the effect of Joule heating*, Journal of Physics D: Applied Physics, 41, 19, pp. 195-206, 2008.

[83] S. Lynikiene, *Carrot seed preparation in a corona discharge field*, Commission Internationale du Genie Rural Journal of Scientific Research and Development, 3, pp. 10-21, 2001.

[84] M. Rickard, D. Dunn-Rankin, F. Weinberg, F. Carleton, *Maximizing ion-driven gas flows*, Journal of Electrostatics, 64, pp. 368-376, 2006.

[85] E. Moreau, L. Leger, G. Touchard, *Effect of DC surface-corona on a flat plate boundary layer for air flow velocity up to 25m/s*, Journal of Electrostatics, 64, pp. 215-225, 2006.

[86] A. Rashkovan, E. Sher, H. Kalman, *Experimental optimization of an electric blower by corona wind*, Journal of Applied and Thermal Engineering, 22 pp. 1587-1599, 2002.

[87] J. Moon, J. Jung, S. Gum, *The Effect of a Strip-type Ring Electrode of a Wire-Plate Type Nonthermal Plasma Reactor on Corona Discharge and Ozone Generation Characteristics*, Journal of Plasma Environmental Science and Technology, 2, 1, pp. 26-33, 2008.

[88] K. Yanallah, F. Pontiga, A. Fernandez-Rueda, A. Castellanos, A. Belasri, *Ozone generation using negative wire-to-cylinder corona discharge: the influence of anode composition and radius*, Proceedings of the IEEE Conference on Electrical Insulation and Dielectrics Phenomena, pp. 607-610, 2008.

[89] K. Yanallah, F. Pontiga, Y. Meslem, A. Castellanos, *An analytical approach to wire-to-cylinder corona discharge*, Journal of Electrostatics, 70, 4, pp. 374-383, 2012.

[90] M. June, J. Kribs, K. Lyons, *Measuring efficiency of positive and negative ionic wind devices for comparison to fans and blowers*, Journal of Electrostatics, 69, 4, pp. 345-350, 2011.

[91] R. Morrison, D. Hopstock, *The distribution of current in wire-to-cylinder corona*, Journal of Electrostatics, 6, 4, pp. 349-360, 1979.

[92] E. Kuffel, W.S. Zaengl, J. Kuffel, *High Voltage Engineering Fundamentals*, Newnes Oxford, 2000.

[93] F. Paschen, *On the potential difference required for spark initiation in air, hydrogen, and carbon dioxide at different pressures*. Annalen der Physik, 273, 5, pp.69-75, 1889.

[94] M. Khalifa, *High-Voltage Engineering Theory and Practice*, New York: Marcel Dekker Inc., 1990.

[95] M. Naidu, V. Kamaraju, *High Voltage Engineering*, New York: Mc Graw Hill, 1996.

[96] C. Wadhwa, *High Voltage Engineering*, New Age International (P) Ltd., 2007.

[97] O. Zienkiewicz, *The Finite Element Method in Engineering Science*, McGraw-Hill, 1977.

[98] D. Vitkovitch. *Field Analysis: Experimental and Computational Methods*, D. Van Nostrand,1966.

[99] K. Hidaka, T. Kouno, *A method for measuring electric field in space charge by means of pockels device*, Journal of Electrostatics, 11, pp. 195-211, 1982.

[100] I. McAllister, *Electric fields and electrical insulation*, IEEE Transactions on Dielectrics and Electrical Insulation, 9, pp. 672-696, 2002.

[101] A. Maglaras, L. Maglaras, *Modeling and analysis of electric field distribution in air gaps, stressed by breakdown voltage*, Proceedings of the WSEAS Conference on Mathematical Methods and Computational Techniques in Electrical Engineering (MMACTEE), 2004.

[102] A. Maglaras, *Numerical Analysis of Electric Field in Air Gaps, Related to the Barrier Effect*, Proceedings of the 1st International Conference 'From Scientific Computing to Computational Engineering', 2004.

[103] L. Zhao, K. Adamiak, *EHD gas flow in electrostatic levitation unit*, Journal of Electrostatics, 64, pp. 639-645, 2006.

[104] M. Rezouga, A. Tilmatine, R. Ouiddir, K. Medles, *Experimental Modelling of the Breakdown Voltage of Air Using Design of Experiments*, Journal of Advances in Electrical and Computer Engineering, 9, 1, pp. 41-45, 2009.

[105] M. Rau, A. Iftemie, O. Baltag, D. Costandache, *The Study of the Electromagnetic Shielding Properties of a Textile Material with Amorphous Microwire*, Journal of Advances in Electrical and Computer Engineering, 11, 1, pp. 17-22, 2011.

[106] J. Cobine, *Gaseous Conductors; Theory and Engineering Applications*. McGraw-Hill, 1970.

[107] J. Lowke, F. Alessandro, *Onset corona fields and electrical breakdown criteria*, Journal of Applied Physics, 28, pp. 2673-2682, 2003.

[108] D. Phillips, R. Olsen, P. Pedrow, *Corona onset as a design optimization criterion for high voltage hardware*, IEEE Transactions on Dielectric Electrical Insulation, 7, 6, pp. 744-751, 2000.

[109] V. Amoruso, F. Iattarulo, *Accurate extension of Peek's law to stranded conductors*, European Transactions in Electrical Power, 1, 1, pp. 15-20, 1991.

[110] K. Yamazaki, R. Olsen, *Application of a corona onset criterion to calculation of corona onset voltage of stranded conductors*, IEEE Transactions on Dielectrics and Electrical Insulations, 11, 4, 674-680, 2004.

[111] P. Cooperman, *A theory for space-charge-limited currents with application to electrical precipitation*, AIEE Transactions, pp. 47-50, 1960.

[112] R. Waters, W. Stark, *Characteristics of the stabilized glow discharge in air*, Journal of Physics D: Applied Physics, 8, pp. 416-426, 1975.

[113] J. Cross, *Electrostatics: Principles, Problems and Applications*, Bristol, Adam Hilger, 1987.

[114] Y. Raizer, *Gas Discharge Physics*, Berlin, Springer, 1997.

[115] J. Jones, A. Boulloud, R. Waters, *Dimensional analysis of corona discharges: the small current regime for rod-plane geometry in air*, Journal of Physics D: Applied Physics, 23, 1652-1662, 1990.

[116] R. Sigmond, *The unipolar corona space charge flow problem*, Journal of Electrostatics, 18, 3, pp. 249-272, 1986.

[117] E. Warburg, *Wied*. Ann, 67, 69, 1899.

[118] E. Warburg, *Handbuch der Physik,* 14, Berlin, Springer, 1927.

[119] R. Sigmond, I. Lagstad, *Mass and species transport in corona discharges*, Journal of Chemical High Temperature Processes, pp. 221-229, 1993.

[120] B. Held, R. Peyrous, *Physical and chemical studies of corona discharges in air*, Czechoslovak Journal of Physics, pp. 301-320, 1999.

[121] C. Jen-Shih, A. Watson, *Electromagnetic hydrodynamics*, IEEE Transactions on Dielectrics and Electrical Insulation, pp. 871-895, 1994.

[122] E. Christenson, P. Moller*, Ion-Neutral Propulsion in Atmospheric Media*, Journal of the American Institute of Aeronautics and Astronautics, 5, pp. 1768-1773, 1967.

[123] J. Bastos, N. Sadowski, *Electromagnetic Modeling by Finite Element Methods*, New York, Marcel Dekker, 2003.

[124] S. Rao, *The Finite Element Method in Engineering*, Elsevier Science, 2011.

[125] J. Mackerle, *Finite element and boundary element modelling of surface engineering systems: A bibliography (1996–1998)*, Journal of Finite Elements in Analysis and Design, 34, pp. 113-124, 2000.

[126] J. Mackerle, *Mesh generation and refinement for FEM and BEM - A bibliography (1990–1993)*, Journal of Finite Elements in Analysis and Design, 15, pp. 177-188, 1993.

[127] P. Sylvester, R. Ferrari*, Finite Elements for Electrical Engineers*, 3rd Edition, New York, Cambridge University Press, 1996.

[128] J. Jin, *Finite Element Method in Electromagnetics*, 2nd Edition, New York: Wiley-IEEE Press, 2002.

[129] D. Meeker, *Finite Element Method Magnetics (F.E.M.M.) Ver 4.2 User's Manual*, 2010.

[130] I. Hlavacek, M. Krizek, *On a super convergent finite element scheme for elliptic systems. I. Dirichlet boundary condition*, Journal of Applications of Mathematics, 32, pp. 131-154, 1987.

[131] Y. Liu, Choose the best element size to yield accurate FEA results while reduce the model's complexity, British Journal of Engineering and Technology, 1, 7, pp 13-28, 2013.

[132] R. Arora, W. Mosch, *High Voltage and Electrical Insulation Engineering*, New Jersey, John Wiley and Sons Inc., 2011.

[133] A. Krupa, *Electric field and charge dirstribution in back discharge in point-plane geometry*, Journal of Physics, Conference Series, 310, 1, pp. 1-4, 2011.

[134] G. Yinliang, X. Xiaodong,, C. Baozhi, *Investigation of Current Density Distribution Model for Barb-plate ESP*, Springer, Berlin, Heidelberg, pp. 359-362, 2009.

[135] K. McLean, I. Ansari, *Calculation of the rod-plane voltage/current characteristics using the saturated current density equation and Warburg's law*, IEEE Transactions on Physics, Science, Measuring Instruments, Management and Education - Reviews, 134, 10, pp. 784-788, 1987.

[136] M. Goldman, R. Sigmond, *Corona and Insulation*, IEEE Transactions on Electrical Insulation, 17, 2, pp. 90-105, 1982.